Understanding the regulation of epidermal tissue thickness by cellular and subcellular processes using multiscale modelling

Claire Miller

ORCID iD: 0000-0003-0758-9447

Doctor of Philosophy

July, 2020

School of Mathematics and Statistics

The University of Melbourne

This thesis is being submitted in total fulfilment for the degree.

Supervisors: James M. Osborne, Edmund Crampin

Abstract

The epidermis is the outermost layer of the skin, providing a protective barrier for our bodies. Two important aspects to the barrier function of the epidermis are maintenance of its barrier layer and constant cell turnover. The main barrier layer in the epidermis is the outermost layer, called the stratum corneum. This layer blocks both the entry of antigens and the loss of internal water and solutes. If antigens do enter the system, cell turnover has been hypothesised to propel them out the system by providing a constant upwards velocity of cells which carry the toxins with them.

The majority of severe diseases of the epidermis relate to a reduction in thickness of the stratum corneum. Decreased thickness reduces the barrier function of the layer, causing discomfort and inflammation. Due to its importance to barrier function, the maintenance of stratum corneum thickness, and consequently overall tissue thickness, is the focus of this thesis.

In order to maintain both stratum corneum thickness and overall tissue thickness it is necessary for the system to balance cell proliferation and cell loss. Cell loss in the epidermis occurs when dead cells at the top of the tissue are lost to the environment through a process called desquamation. Cell proliferation occurs in the base, or basal, layer. As the basal cells proliferate, cells above them are pushed upwards through the tissue, causing constant upwards movement in the tissue. Not only does this contribute directly to the barrier function through the cell turnover as discussed above, but the velocity of the cells is likely to be key in regulating the tissue thickness. Assuming the cell loss occurs at a fairly constant rate, the combination of the velocity and the loss rate determine tissue thickness.

In order to investigate these processes we develop a three dimensional discrete, multiscale, multicellular model, focussing on maintenance of cell proliferation and desquamation. Using this model, we are able to investigate how subcellular and cellular level processes interact to maintain a homeostatic tissue.

Our model is able to reproduce a system that self-regulates its thickness. The first aspect of this regulation is maintaining a constant rate of proliferation in the epidermis, and consequently a constant upwards velocity of cells. The second aspect is a maintained rate of desquamation. The model shows that hypothesised biological models for the degradation of cell-cell adhesion from the literature are able to provide a consistent rate of cell loss which balances proliferation. An investigation into a disorder which disrupts this desquamation model shows reduced tissue thickness, consequently diminishing the protective role of the tissue.

In developing the multiscale model we have begun to delve deeper into the relationship between subcellular and cellular processes and epidermal tissue structure. The model is developed with scope for the integration of further subcellular processes. This provides it with the potential for further experiments into the causes and effects of behaviours and diseases of the epidermis, with much higher time and cost efficiency than other experimental methods.

Declaration of Authorship

This is to certify that

1. the thesis comprises only of my original work towards the PhD except where indicated in the Preface;
2. due acknowledgement has been made in the text to all other material used; and
3. the thesis is less than 100,000 words in length, exclusive of tables, maps, bibliographies and appendices.

Signed:

_____

Claire Miller, February 2020

Preface

Chapters 4 and 5 reproduce content from an article in preparation, available on arXiv (`arxiv.org/abs/1811.10781`). Authors of this article are myself (Claire Miller), Edmund Crampin, and James M. Osborne. I was the primary author of the publication and contributed 90% of the work. Each of the authors contributed to conceiving, developing, and analysing the model, and drafting of the manuscript.

Chapters 6 to 8 also reproduce content from an article in preparation. Authors of this article are myself (Claire Miller), Edmund Crampin, and James M. Osborne. I was the primary author of the publication and contributed 95% of the work. Each of the authors contributed to conceiving, developing, and analysing the model, and drafting of the manuscript.

This thesis includes several third party figures. These are listed on page 23.

All other work in this thesis is my own. None of the work in this thesis has been submitted for other qualifications. None of the work in this thesis was carried out prior to enrolment in the degree. No third party editorial assistance was provided in the preparation of this thesis.

Financial support

I am supported by the Australian Government Research Training Program (RTP) Scholarship (formerly the Australian Postgraduate Award). Financial assistance was provided by Australian Research Council Centre of Excellence in Convergent Bio-Nano Science and Technology (project number CE140100036)

Acknowledgements

First and foremost, I wish to thank my two supervisors: James Osborne and Edmund Crampin. Thank-you for your guidance, whether that be mathematical, biological, or editorial. You have helped me to develop the necessary skills to become an independent researcher and to ask interesting mathematical and biological questions. Without your commitment and assistance this PhD would not have happened.

Secondly, my committee chair, James McCaw, for making sure I always kept perspective throughout PhD, and ensuring that I remained on target. Thirdly, I would like to thank Kirsten Hoak for her ready assistance with everything and anything administrative.

Many people have given me support throughout the PhD. This list starts with the amazing group of students and staff of OGS level 3 over the past four years. In particular I would like to thank Hilary Hunt, Tiffany Leung, Michael Lydeamore, Alex Zarebski, Stuart Johnston, Dominic Maderazo, Sarah Belet, and Domenic Germano. Without your guidance, confidence in my abilities, and willingness for endless coffees and chats, this thesis would not even be close to where it is today.

A big thank-you to both Kate Saunders and Alicia Chenoweth. You have both been a constant inspiration to me throughout my PhD and the many other years of our friendships. Your confidence in assuaging any of my concerns made me believe that this was possible. Watching you navigate the end of your PhDs and the start of your careers has made me so proud to be your friend.

Thank-you to Alana Overmeyer, my adventure buddy. You have always been

there to provide support when I needed it. Our trips together have been epic over the last few years, and given me the mental breaks I now realise I may not have coped without.

And to Sophie Francis, for always helping to give me perspective. Your optimistic attitude and confidence in me have helped me to be proud of my achievements, both big and small.

Finally, I would like to thank my family. My father, for always being happy to provide an external perspective on the work and proofreading. My mother, for her support, particularly when I needed to come home for a break.

There are so many other people I could list here. This includes long-time friends from high school and undergraduate studies who have stuck with me all these years, the friends I have met through climbing, and my flatmates. I am continually inspired by the level of support and friendship so freely given to me by all these people.

Contents

List of Figures

List of Tables

Third Party Copyright Material

This thesis includes third party figures. These are provided in the table below.

Citation Information for Third party copyright material	**Location in thesis**	**Permission status**
Pasparakis, M., Haase, I., and Nestle, F. O. *Nature Reviews Immunology* 14.5 (May 2014). DOI: 10.1038/nri3646	Figure 2.1, p. 34	Granted
Alberts, B. et al. New York, NY: Garland Science, Taylor and Francis Group, 2015. ISBN: 978-0-8153-4432-2	Figure 2.4b, p. 40; Figure 2.7a, p. 46	Granted
Krstić, R. V. Berlin; New York: Springer-Verlag, 1979. ISBN: 978-0-387-09583-7	Figure 2.7b, p. 46	Granted
Osborne, J. M. et al. *PLoS Computational Biology* 13.2 (2017). DOI: 10.1371/journal.pcbi.1005387	Figure 3.2, p. 60	Granted
Igawa, S. et al. en. *Experimental Dermatology* 20.1 (Jan. 2011). DOI: 10.1111/j.1600-0625.2010.01170.x	Figure 7.7, p. 169	Granted

Glossary

Basal Forming or occurring in the base layer, e.g. basal cells are in the base layer of the epidermis.

CD Cell diameters.

CND Corneodesmosome.

Corneodesmosome Protein complexes that form the adhesion between the cells in the stratum corneum of the epidermis. Similar to desmosomes but with additional proteins.

Desmosome Protein complexes that form the adhesion between the cells in the epidermis.

Desquamation Cell loss from the top of the epidermis through loss of sets of cells, also known as squames.

Differentiated cell A non-proliferative or post-mitotic cell.

Extracellular Outside of a cell or cells.

IFE Inter-follicular epidermis.

Inter-follicular epidermis The region of the epidermis between hair follicles.

Intracellular Within a cell or cells.

Keratinocyte A type of cell named for its production of keratin (an intracellular structural protein). The majority (95%) of cells in the epidermis are keratinocytes.

KLK Kallikreins (KLKs) are a species of enzyme, specifically a subgroup of serine proteases.

KLK5 Kallikrein-related peptidase 5 (formerly known as SCTE). An enzyme expressed in the epidermis relating to the degradation of corneodesmosomes.

LEKTI Lympho-epithelial Kazal-type-related inhibitor (LEKTI) is an inhibitor of serine proteases. Also known as serine protease inhibitor Kazal-type 5 (SPINK5).

M phase The final phase of the cell cycle in which the parent cell contracts in its centre before finally splitting to become two daughter cells.

NS Netherton Syndrome.

Progenitor cell A proliferative cell that can undergo any number of divisions, generally with a short cell cycle time.

Stem cell An immortal proliferative cell, generally with long cell cycle times.

Stratum corneum The stratum corneum, or corneum, is the top-most layer of the epidermis. This layer contains sheets of flat dead cells, which are lost to the environment at the top of the layer.

Suprabasal Above the basal layer, e.g. suprabasal cells are all cells not in the basal layer.

Transit cell Also known as a transit amplifying cell. A proliferative cell that undergoes a set number, e.g. 3, of divisions before differentiating.

1 | Introduction

The epidermis is the outermost layer of the skin. It plays a major role in our body's defence against the outside world, and maintenance of its thickness is a critical component of this role. The thickness of the epidermis is not a precise quantity—not only does it vary between individuals, it also varies across your own body. Reasons for this variation have been hypothesized but are not known, and likely involve a large variety of genetic and environmental factors. Defects causing excessive loss or accumulation of skin cells can lead to health issues such as inflammation and allergies [22].

Despite being a seemingly easily accessible tissue, we still have little understanding of how tissue thickness is regulated. As with any biological tissue, the epidermis is a complex system with multiscale behaviours and mechanisms all contributing to the overall thickness of the tissue. We hypothesise that two key players for this process are proliferation and desquamation. Specifics on how these processes interact and whether they are sufficient to maintain a consistent thickness is not known.

By building a tissue scale mathematical model of the epidermis, we are able to investigate how epidermal thickness is maintained. We do this by taking the information from experimental models, either *in vivo* (in culture) or *in vitro* (in animal), to create a model to replicate the key behaviours of proliferation and desquamation in the tissue. By then implementing these components into the model in more detail we can determine whether they are sufficient to maintain a healthy tissue. These results inform us on what might be occurring in the biological tissue, and also provide

further insight on how defects in the system could affect epidermal thickness.

1.1 How does the epidermis regulate its thickness?

1.1.1 The inter-follicular epidermis and cell turnover

The epidermis is a type of epithelial tissue. Epithelial tissues are tissues which provide the inner and/or outer linings of our body organs—in this case the skin.

The term inter-follicular refers to the region of the epidermis between hair follicles. The inter-follicular epidermis (IFE) is constantly producing new cells at the base of the tissue which migrate upwards and are eventually lost to the environment. It is thought that the constant turnover of cells contributes to the barrier function of the epidermis.

This cell influx and loss is all part of the highly specific structure of the IFE. Cell production occurs in a base layer of cells, called the basal layer, where cells are proliferative—they divide to create new cells. Once cells leave the basal layer, they no longer divide and move up through the next two layers: the spinous and granular layers. Within these two layers cells undergo a series of changes. These changes include a gradual flattening, as well as changes to mechanical properties, such as stiffness and adhesion to other cells. The final layer is the stratum corneum. It is from the top of this layer that cells are lost to the environment.

1.1.2 Key processes of thickness regulation in the epidermis

It is critical for our health that the thickness of the epidermis is maintained. We hypothesise that the thickness maintenance is due to maintained proliferation in the basal layer and a controlled rate of desquamation from the top of the tissue. This is because cells enter the system due to the proliferation in the basal layer. The entry

of these cells pushes the cells above outwards towards the outside of the tissue, where they are eventually lost. Consequently the rate of proliferation determines the upwards velocity of the tissue. The desquamation process determines the rate at which the cells are lost. We expect these two processes to determine the thickness of the tissue.

1.1.3 Computational modelling can help us understand this system

In order to better understand the regulation of thickness in the epidermis, we build a three dimensional multiscale multicellular model of the tissue. This enables us to implement different processes, and to understand their effect and interactions. Additionally, the inclusion of subcellular models enables a better understanding of the interaction between different scales, and the effect on the tissue. Specifically, we focus on models of proliferation and desquamation, and the balance between them.

Cell balance begins with maintenance of a basal layer. In order to provide a constant influx to the system, it is necessary to maintain a constant population of proliferating cells. We propose a new mechanism for cell division to better maintain a steady state population of stem cells.

The second component of this balance is desquamation. We implement a new, mechanistic model for desquamation at the top of the tissue, based on the degradation of the adhesion between cells. This allows us to better understand the relationship between proliferation rate, desquamation rate, and tissue thickness. By then developing a subcellular model for the degradation of adhesion, and incorporating it into the multicellular model, we are able to gain insight into the desquamation process.

The combination of each of these components in the computational model will provide us within insights on the mechanisms necessary for the epidermis to maintain its thickness.

1.2 Thesis outline

This thesis will firstly introduce readers to the biology of the inter-follicular epidermis in **Chapter 2**. Following on from this **Chapter 3** is an overview of computational models of the inter-follicular epidermis, and biological insights that have risen from these models. These first two chapters will provide the biological and mathematical modelling background required to follow the research discussed in the remainder of the thesis.

Chapter 4 will provide an overview of the multicellular model that provides the base model for this thesis. This model is based upon previous models in the literature. The subsequent chapters build upon this model and answer the following three questions that, together, produce insight into how the epidermis regulates its thickness:

Chapter 5: how is the proliferative population maintained in the basal layer of the epidermis? This chapter begins with a base multicellular model, developed based on methods from previous literature. The results using this base model show erroneous loss of proliferative cells from the basal layer. Consequently, to counter this loss, we include a mechanism inspired by the regulation of division direction seen in experimental literature. This mechanism regulates the direction of the division, and we find that it enables us to maintain higher densities of proliferative cells in the basal layer.

Chapter 6: what is the relationship between basal cell proliferation rate, upwards cell velocity, degradation of cell-cell adhesion, cell loss, and tissue thickness? In this chapter we include a mechanistic model for cell desquamation, based on the degradation of cell-cell adhesion at the top of the tissue. We find that, in combination with a maintained basal layer population, we are able to maintain a steady state thickness in the system. By varying

proliferation rate and the rate of decay of the adhesion we are able to determine a relationship between these two parameters in the model.

Chapters 7 and 8: can subcellular regulation of cell-cell adhesion generate an epidermal tissue that regulates its thickness? In Chapter 7 we develop a computational subcellular model for desquamation, based on hypothesised protein interactions from the literature. In Chapter 8 we couple this subcellular model with the multicellular model to investigate whether this model is sufficient to regulate desquamation. We use this model to investigate both healthy and diseased function, tissue thickness, and the relationship between the subcellular processes and the resulting tissue.

The final chapter of this thesis is **Chapter 9**, which provides a summary of the research done for this study and outlines the insights into maintenance of epidermal tissue thickness from these results.

2 | Biology of the Inter-follicular Epidermis

The inter-follicular epidermis is the outermost layer of our skin. It provides our bodies with a barrier to the ingress of toxins, pathogens, allergens and other unwanted materials into our tissues and blood stream [75]. This chapter provides a background of the biology of the inter-follicular epidermis (IFE) relevant to this thesis. It begins with a brief outline of the IFE tissue, then follows the migration of a cell through the tissue, with a focus on each of the key cell properties and the mechanics of each tissue layer. Finally, the chapter ends with an introduction to subcellular processes involved in IFE maintenance and a discussion on different diseases associated with the IFE.

2.1 IFE tissue

The epidermis is the layer of our skin that is exposed to the environment. It is located above the dermis (see Figure 2.1) and, for adults, covers an area of approximately 1.8 m^2 [106]. The IFE is the region of the epidermis between the hair follicles. As it is the outermost layer, the IFE is the part of our body exposed to the environment. Therefore it must maintain a barrier against external stresses and toxins, as well as preventing the loss of internal liquids. The IFE does this by creating a strong barrier in the outermost layers of its structure and by maintaining a constant outward flux

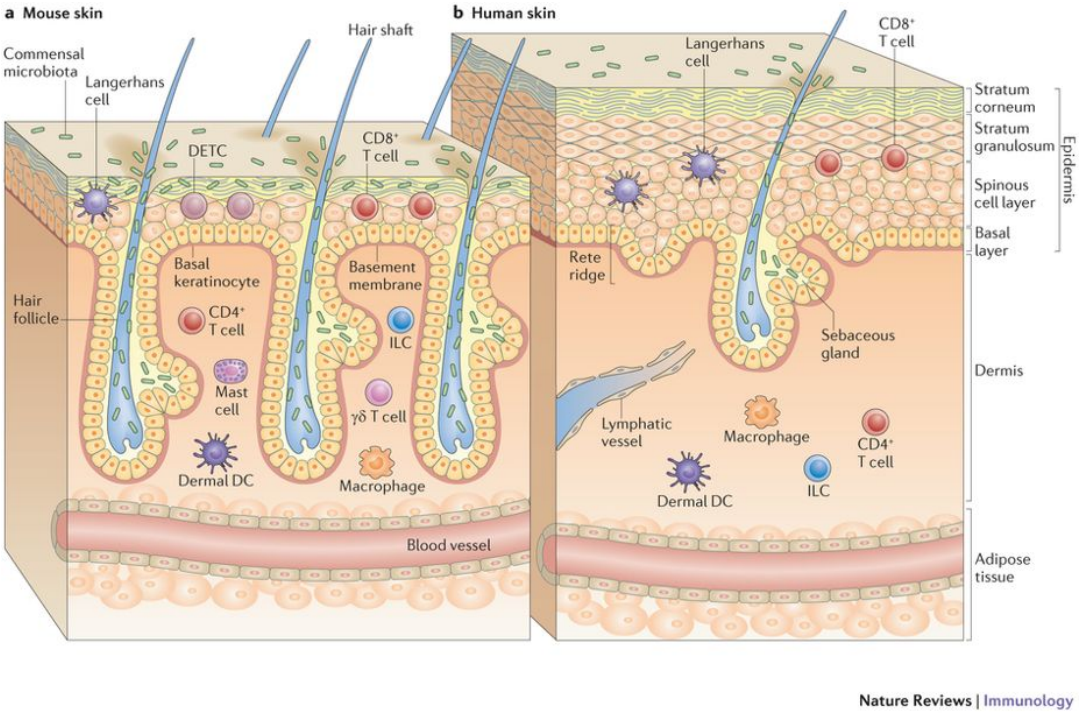

Figure 2.1: The structure of mouse and human skin. (Image reproduced with permission from Pasparakis, M., Haase, I., and Nestle, F. O. *Nature Reviews Immunology* 14.5 (2014) [92]).

of cells, replacing cells lost at the surface. Here, we consider the macro structure of the IFE and the cell flux.

The IFE is a biological tissue, which means it is composed of a collection of cells with the same purpose. Biological tissues are subdivided into four different categories: muscle, epithelial, connective, and nervous tissue. The IFE is classified as an epithelial tissue due to its composition of sheets of cells in a multi-layered structure [4]. An illustrative diagram of the structure of the IFE is shown in Figure 2.2. It contains four distinct layers of cells, which are separated from the dermis by an undulating basal membrane. From deep to superficial, these layers are the basal layer, spinous layer, granular layer, and stratum corneum. Each layer varies in its biology and function.

The IFE is composed of 95% keratinocytes, with the other 5% of cells being

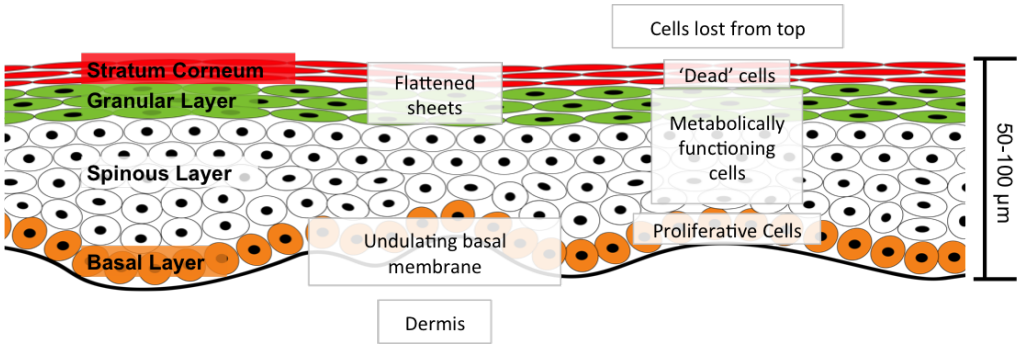

Figure 2.2: The structure of the epidermis.

a collection of melanocytes (pigments), Langerhans cells (immune response), and Merkel cells (nervous system) [77]. For the purposes of this thesis, we only consider keratinocytes.

As mentioned above, the epidermis is constantly being renewed via an upward flux of cells. This constant turnover has been hypothesised to be a way to help flush harmful microorganisms or viruses from the tissue [75]. It takes a human IFE cell three to four weeks to migrate from the base to the surface [21, 82, 98, 123]. This transit time is much longer than the transit time in mouse epidermis, which has been measured to be between eight and ten days [97]. The shorter transit time of IFE cells in mice is likely related to the lower number of cell layers, around ten, which is roughly half to a third that of humans [75]. These transit times and layer counts, along with other differences between mouse and human epidermis, are summarised in Table 2.1. Understanding these differences is important as much of the experimental data discussed in this chapter is taken from mouse epidermis studies, and therefore we can not assume all the results translate directly to human epidermis.

The constant outwards cell movement in the IFE occurs due to continual proliferation of cells in the basal layer of the tissue. Proliferation is the division of a single cell (parent), into two cells (daughters). The basal layer is the first layer of cells, located on the basal membrane. Cells proliferate within this layer and then

Property	Mouse epidermis	Human epidermis
Basal membrane	Essentially flat, with a high density of hair follicles in the torso region [5, 112]	Undulating [92]
Tissue layer count	10 [75]	17–30 [75]
Transit time	8–10 days [97]	3–4 weeks [21, 82, 98, 123]
Cell cycle times	2–7 days (progenitor/transit), 2–3 months (stem) [19, 74, 105]	13 days [123]

Table 2.1: Some important differences between mouse and human epidermis.

move up through the subsequent three layers, before being lost to the environment. Suprabasal cells, those not in the basal layer, are post-mitotic (no longer proliferative). As cells move up through the tissue, their shape flattens. When the cells reach the stratum corneum, they are classified as dead and have no nucleus, and are eventually shed from the skin through a process known as desquamation. The biology of each of the layers and processes is summarised in Figure 2.2 and described in further detail below in Sections 2.2 to 2.4.

Due to the constant upwards movement of cells, maintaining a steady tissue thickness in the IFE requires a balance between cell proliferation at the base of the tissue and desquamation from the top of the tissue. IFE thickness varies between individuals and by body location, as shown in Figure 2.3. Most of the IFE on our bodies is approximately 50–100 μm thick, however the finger and heel of the foot are much thicker—approximately 222 μm and 660 μm respectively. The high variation in thickness is an indication that environmental factors, such as UV [107] and forces, that different areas of our bodies are exposed to may have significant impact on the tissue. Additionally, the IFE on the palm of the hand and sole of the foot, called

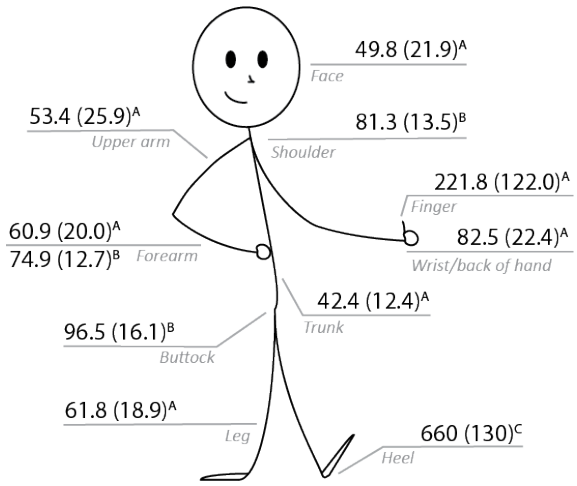

Figure 2.3: The measured thickness of the epidermis across different parts of the body in units of μm. Measurements shown as 'mean (standard deviation)'. The two measurements shown for forearm are due to a difference in the values between the two sources. Sources: (A) Whitton and Everall [124], (B) Sandby-Møller, Poulsen, and Wulf [107], and (C) Chao, Zheng, and Cheing [18].

thick skin (compared to thin skin elsewhere), varies slightly from the rest of the IFE and even contains an additional layer [36, 106]. Our discussion of the tissue ignores this fifth layer as is not present in the majority of the IFE. It is not known exactly how the thickness is determined and maintained by the tissue and this is a topic we explore in Chapter 6.

We next consider the functions of each layer in finer detail, following the journey of an IFE cell as it moves up through the tissue.

2.2 Cell production and the basal layer

An IFE cell's journey begins with its creation as a result of proliferation in the basal layer of the tissue. The basal layer is composed of a single layer of cells sitting above the basal membrane. This layer can also be called the *stem cell niche*, as it is where the stem cells are located. It is important to maintain a stable proliferative

population in this layer to maintain a consistent level of proliferation. This topic is investigated in Chapter 6.

2.2.1 The basal membrane

The basal membrane, also known as the basement membrane, separates the epidermis from the dermis below, as seen in Figure 2.1 and Figure 2.2. The basal membrane is a type of extracellular matrix. Cells in the basal layer attach to the membrane. Details of how this attachment occurs will be explained in Section 2.3. As noted in Table 2.1, in human IFE this membrane is an undulating boundary, composed of a heterogeneous series of dips known as rete ridges (see Figure 2.1) [92]. However, in mice the basal membrane of the IFE is almost flat [112]. This is another important difference to consider when discussing experimental results from mouse epidermis.

2.2.2 Proliferation

Proliferation is the production of new cells and the process by which the tissue continually renews itself. A proliferative cell is a cell that is able to divide, while a cell that is not able to divide is termed a post-mitotic or *differentiated* cell. Consequently, the term *differentiation* refers to a proliferative cell becoming a post-mitotic cell.

All proliferative cells in IFE tissue are contained in the basal layer. There are three potential types of proliferative cell in the basal layer: stem cells, progenitor cell, and/or transit amplifying cells [5, 19, 47]. Stem cells are generally considered to be effectively immortal, slow cycling cells. A progenitor cell is faster cycling than a stem cell with the potential to differentiate into a post-mitotic cell under certain conditions. Transit amplifying cells are similar to progenitor cells, but have a limited number of divisions they can undergo before differentiating.

There are two main aspects of cell proliferation: the cell cycle and the cell lineage. The cell cycle is the process that every proliferative cell undergoes between divisions. The cell lineage describes the proliferative cell types that occur in the basal layer. These are described below.

The cell cycle

The cell cycle is the general process of division all proliferative cells in the body undergo. A diagram of the cell cycle can be seen in Figure 2.4a. The cycle always consists of four phases: G_1, S, G_2, and M phase, in that order, with an optional fifth G_0 phase. Phases G_1 and G_2 are gap phases during which cells mainly grow and monitor their environment. During the S, or synthesis phase, the cell's chromosomes (structures containing the cell's DNA) are duplicated. This phase takes close to half the cycle time. The final M, or mitosis, phase is a short phase, for example 1 hour of a 24 hour cycle in some cells. It is during this phase that the cell splits into two daughter cells [4].

The optional fifth phase that a cell can enter is the G_0 phase, or resting phase. If, during the G_1 phase, a cell receives a certain signal, or finds the environment unfavourable, it will enter the G_0 phase. This is, essentially, a way of delaying the cell cycle. Cells in this state are known as *quiescent cells*. It is possible for a cell to remain in this state for an indefinite amount of time. Once an appropriate signal is received by the cell, it will re-enter the standard cell cycle and continue through the end of the G_1 and onto the S phase [4, 15].

The length of time it takes a cell to undergo the standard cell cycle in the IFE has not yet been precisely measured. Experimentally determined cell cycle times vary between *in vitro*, *in vivo* mouse, and *in vivo* human cells. The shortest cycle times measured are from *in vitro* experiments, varying from 14.5 hours for non-confluent cell culture to 24 hours or more for confluent or near-confluent culture [23]. In these experiments, the M phase length measured 25–60 minutes. Studies of mouse skin

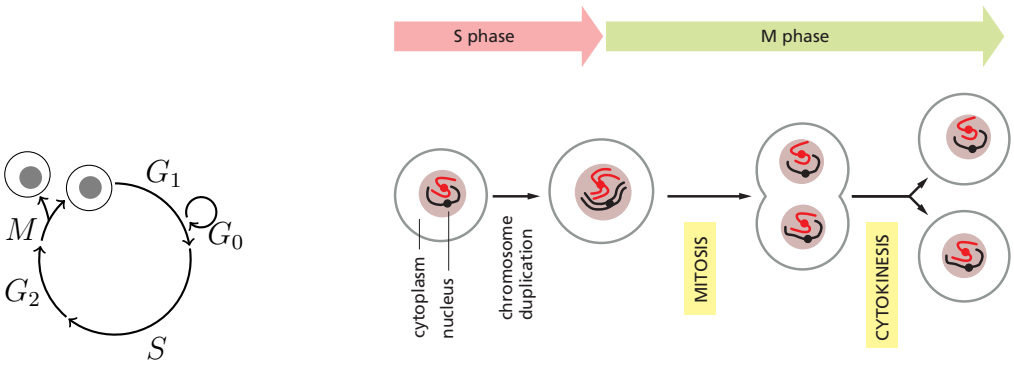

(a) The cell cycle

(b) The mitotic phase.

Figure 2.4: The cell cycle (a), with further detail on the M phase (b). Note the contraction at the centre of the cell (second to last time point) before it splits. (Image (b) reproduced from MOLECULAR BIOLOGY OF THE CELL, SIXTH EDITION by Bruce Alberts, et al. Copyright © 2015 by Bruce Alberts, Alexander Johnson, Julian Lewis, Martin Raff, Keith Roberts, and Peter Walter. Used by permission of W. W. Norton & Company, Inc. [4]).

measured longer cycle times: Sada et al. [105] recorded two or three days, Clayton et al. [19] recorded six days for progenitor cells, and Mascré et al. [74] recorded seven days for progenitor cells and two to three months for stem cells [19, 74]. *In vivo* experiments in human epidermis have shown even longer cycle times of around 13 days (not specific to cell type) [123], with other reports stating 12–19 days [30] (see Table 2.1).

The diagram in Figure 2.4b shows the representative shape change of the cell as it undergoes the M phase. As can be seen in the figure, the cell splits its duplicated chromosomes in two, separates them to the two sides of the elongating cell, then contracts and splits through the middle. An important player in this process is the mitotic spindle (not shown in the figure). The mitotic spindle is formed during the M phase and consists of two poles at either end of the dividing cell. Its main role is to separate the two sets of chromosomes to the two sides of the elongated cell [4].

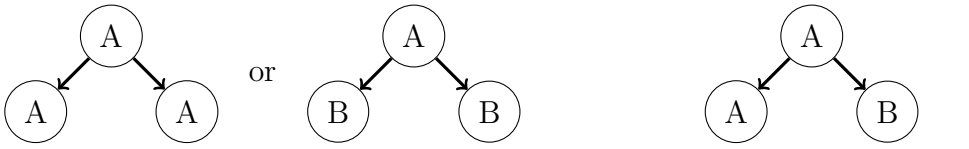

(a) Symmetric division (b) Asymmetric division

Figure 2.5: Symmetry of division. A parent cell of proliferative type A divides into two daughter cells of type A and/or a different cell type, B.

However, it does perform another role relevant to our research—regulation of the division direction, which will be discussed in Chapter 5.

Cell lineage in the IFE

Cell lineage refers to the progression of cell types that occurs as a cell divides, until eventually a differentiated cell is produced. Our understanding of the cell lineage in the IFE has evolved over the last few decades, and is a topic that has generated a variety of hypotheses and interpretations in the literature. The different lineages are all some combination of stem cell, transit amplifying cell, and/or progenitor cell, ending in a differentiated cell which migrates upwards.

Before we discuss current lineage hypotheses, we must first describe the concept of *division symmetry*. The two daughters of a cell division may have the same cell type, termed *symmetric division*, or different cell types, termed *asymmetric division*, as shown in Figure 2.5. In symmetric division, both cells either retain the proliferative type of the parent or both progress down the cell lineage. In asymmetric division, one cell retains the proliferative type of its parent, while the other progresses down the cell lineage.

In other biological tissues, it is thought that asymmetric division occurs during homeostasis, and symmetric division occurs only when there has been an insult to the system [86]. It is known that symmetric division occurs in the IFE in early embryonic development, switching to asymmetric late in development [86]. However,

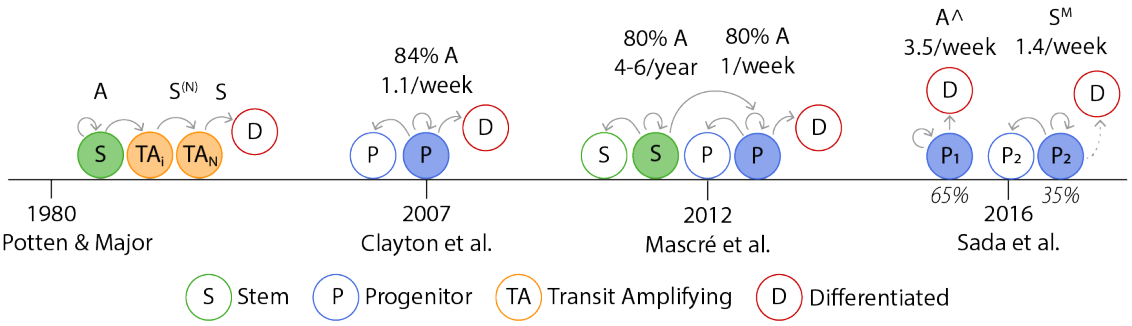

(a) The different lineage hypotheses over time for IFE tissue in homeostasis.

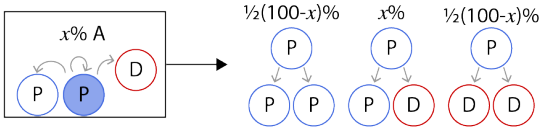

(b) Interpretation of x% A.

Figure 2.6: Cell lineage hypotheses in the IFE. A: asymmetric division, S: symmetric division, $S^{(N)}$: N generations of symmetric division, A^: asymmetric division coupled with upwards movement, S^{M}: symmetric division with stochastic upward migration resulting in differentiation.

it is not clear which is dominant in the homeostatic adult epidermis, with evidence varying with the different cell lineage hypotheses, as described below.

Figure 2.6a shows the proposed cell lineage hypotheses. The results discussed in this section are all from *in vivo* mouse studies, rather than *in vitro*. The traditional view on IFE cell lineage is that the basal layer consists of a population of stem cells which produce transit amplifying cells which divide a limited number of times before terminally differentiating [4, 23, 59, 112]. The first evidence we have found of a stem-transit amplifying lineage *in vivo* was published in 1980 by Potten and Major [99]. This lineage developed over time to become what is now known as the the hierarchical model for epidermal cell lineage [47] and is first lineage shown in Figure 2.6a.

In 2007 Clayton et al. [19] proposed an alternative hypothesis—progenitor cells

maintain the IFE, with the possibility of a population of quiescent stem cells only contributing in the event of injury to the tissue. These authors found evidence of individual cells persisting in the basal layer of mouse back and tail skin for longer time periods than the originally hypothesised proliferation lifetime of a transit amplifying cell. They proposed a stochastic model in which the progenitor cells divide predominantly asymmetrically, and the remaining small number of symmetric divisions produce two progenitor cells or two differentiated cells with equal probability. This is the second lineage shown in Figure 2.6a.

The model from Clayton et al. [19] was seemingly in conflict with a large historical body of results supporting the hierarchical model. A potential reconciliation between the two competing models is simply that both are true, with transit amplifying cells being a further specialised case of progenitor cells [59]. In 2012, Mascré et al. [74] proposed a model which could be considered such a 'combined' hierarchical-progenitor model; this is the third lineage shown in Figure 2.6a. Mascré et al. [74] presented experimental results from mouse tail skin showing evidence of two populations of stochastically dividing proliferative cells: a slow cycling population of stem cells dividing every two to three months, and a fast cycling population of progenitor cells dividing once a week. In this model, the two populations divide predominantly asymmetrically (80% of divisions), with the remaining small number of symmetric divisions equally likely to differentiate or remain the same proliferative type as the parent.

More recently, in 2016, Sada et al. [105] collected further data from mouse back and tail skin, and found neither the Clayton et al. [19] nor the Mascré et al. [74] model was able to explain the observed dynamics. Instead, they proposed an alternative model, the final model shown in Figure 2.6a, where the proliferating population consists of two, spatially segregated, fast-cycling proliferative cell populations. The first population, accounting for two thirds of the basal layer, divides asymmetrically, with the differentiated daughter immediately moving suprabasal, while the second

population divides symmetrically with migration from the basal layer occurring as a separate process to division. Additionally, they found their populations divided at much higher rates than hypothesised in the Clayton et al. [19] and Mascré et al. [74] models.

It is important to consider two things when considering these hypotheses. Firstly, as mentioned previously, there are significant differences between human and mouse skin. Additionally, different experimental methodologies can cause differences in which proliferative cells were successfully labelled, which may partially explain the differences in observations [47]. We provide a brief investigation into the robustness of each of these models in Section 4.2.2.

An alternative theory is that the cell type is not predetermined by cell lineage, but rather is determined by the environment. Given that differentiated as well as multiple types of proliferative cells have been observed in the basal layer, this is difficult to substantiate [19, 47]. However, there is some experimental evidence that the 'stem-ness' of a cell in human IFE could be related to whether it is at the base or peak of a rete ridge [112] (see Figure 2.2). In this thesis, we do not consider this hypothesis and assume the cell type is predetermined by lineage.

2.3 Keratinocyte metamorphosis and the middle layers

Upon leaving the basal layer, our cell is now differentiated and proceeds through multiple cell sheets in the spinous layer and the three cell sheets forming the granular layer [75]. As it passes through these middle two layers the cell gradually transforms into the required structure it needs to enter the stratum corneum. Three of the key changes that occur to the cell during its migration from basal layer to corneum are cell shape, cell-cell adhesion, and cell strength. These are detailed below.

Cell shape

Cells in the basal layer are ellipsoids of approximately 6–8 μm horizontal diameter and a larger vertical diameter. As the cell migrates through the spinous and granular layers, it becomes increasingly horizontal, and consequently the layers become less dense. By the time the cell enters the stratum corneum it is long and flat, reaching 20–40 μm horizontal diameter and less than 0.5 μm high [11, 57, 77]. A representative diagram of this shape change can be seen in Figures 2.1 and 2.2.

Cell-cell adhesion

In the IFE, cells adhere to each other via adhesive protein complexes. In order for these bonds to form between cells, specific transmembrane proteins (proteins spanning from the interior to the exterior of the cell across the cell membrane) are expressed by the cells. One such transmembrane protein type is the Cadherins which, in combination with intracellular (within cell) proteins, form desmosomes and adherens junctions—complexes that cause the adhesion between cells [4, 55]. Additionally, in the basal layer, expression of the transmembrane protein integrin allows for specialised complexes, hemidesmosomes and focal adhesions, to form with the basal membrane. It is possible that integrins are also expressed between basal cells parallel to the membrane [1, 4, 44, 103].

The different adhesion complexes commonly present in epithelial tissues are shown in Figure 2.7a. We focus first on desmosomes, which are the most important adhesion complexes for the purposes of this thesis. The distribution of desmosomes around the cells changes as it migrates through the tissue. Desmosomes in the basal layer of the skin are smaller and less organised. The spinous layer is also called the 'prickly' cell layer as desmosomes can be seen as 'prickles' around the cell membranes, as can be seen in Figure 2.7b [4, 62]. These desmosomes then become larger and more organised in the higher layers [4, 41]. On entry to the stratum corneum, the surface layer, desmosomes are transformed into corneodesmosomes with the ad-

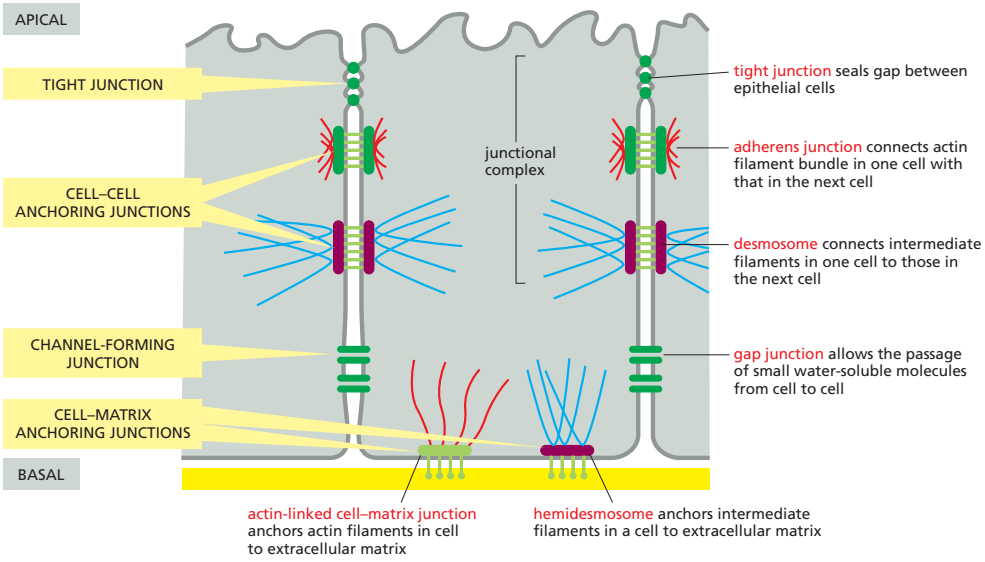

(a) The different adhesion types in epithelia.

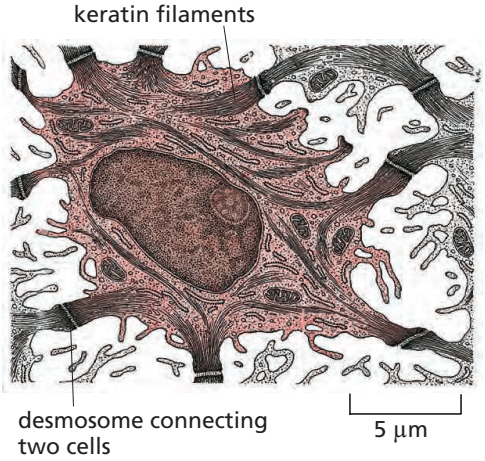

(b) Top view of a keratinocyte in the spinous layer

Figure 2.7: The types and structures of adhesion junctions and keratin in the IFE. (Image (a) reproduced from MOLECULAR BIOLOGY OF THE CELL, SIXTH EDITION by Bruce Alberts, et al. Copyright © 2015 by Bruce Alberts, Alexander Johnson, Julian Lewis, Martin Raff, Keith Roberts, and Peter Walter. Used by permission of W. W. Norton & Company, Inc. [4]. Image (b) reproduced with permission from Krstić, R. V. Berlin; New York: Springer-Verlag, 1979 [67]).

dition of a further protein, corneodesmosin, to the complex [54]. The number of corneodesmosomes then decreases in the direction of the skin surface. This degradation of adhesion proteins is important for homeostasis and excessive numbers of desmosomes at the top of this layer can cause skin abnormalities [102]. This is discussed in more detail in Section 2.4 and Chapter 7.

Desmosomes (and hemidesmosomes) link to the intermediate filament keratin [4], shown as blue lines in the cell in Figure 2.7a. Filaments are proteins contributing to the cell's structure and strength.

The formation of desmosomes requires prior formation of adherens junctions [71]. Adherens junctions, also shown in Figure 2.7a, connect to actin filaments (red lines in the figure), similarly to desmosomes connecting to keratin. Adherens junctions are believed to be random in formation [119] and calcium dependent [119]. This is important since calcium concentration increases from the spinous to granular layer, before decreasing again in the corneum [29]. In contrast, desmosomes become more stable and insensitive to extracellular calcium with age, and consequently height in the tissue [41, 119].

Also shown in Figure 2.7a are tight junctions and gap junctions. Tight junctions are barrier junctions that prevent the passage of molecules through extracellular space [4]. Tight junctions are known to form at the top of the granular layer and persist in the lower half of the corneum [12, 26, 62, 49]. The impact of these tight junctions on subcellular cell-cell adhesion-related processes is discussed further in Chapter 7. Gap junctions are a junction that enable cell-cell communication and are also known to be present in the epidermis [4, 79]. As they are not relevant to cell-cell adhesion we do not consider them here.

Cell strength

Keratinocytes have a high stiffness relative to other cell types, and this is maintained even after cell death in the stratum corneum [73]. Keratin is the dominant structural

element of the keratinocyte, providing the cell with mechanical strength as well as its name [4, 33]. Keratins are a type of elastic, fibrous protein, which bundle to form intermediate filaments that span the cell between desmosome junctions (see Figures 2.7a and 2.7b) [4, 75]. As seen in the Figure 2.7a, the desmosomes connect the keratin between the different cells, allowing them to form large, strong sheets. As the cell migrates through the spinous and granular layers towards the surface of the tissue, the total amount of keratin in the cell increases [33], consequently increasing the stiffness of the cell. Other structural proteins that help provide stiffness are actin filaments and microtubules [109].

2.4 Cell loss and the stratum corneum

After passing through the middle layers, our cell finally reaches the outermost layer: the stratum corneum. The cell is now known as a *corneocyte*. The stratum corneum (also known as the cornified layer) is an important barrier layer, and is also the layer from which the cell is lost from the IFE, and consequently the body, to the environment. It has the highest number of cell sheets, ranging from 10 to 20, though it only contributes to around 10–25% of the thickness of the tissue [75, 78, 82, 107]. This is because the cells are now much flatter compared to the cells in the lower layers. The migration through the corneum can take around 18.5–26.5 days in human IFE, depending on location on the body, which is the majority of the cell's total time in the tissue [104].

The cell does not die via the standard methods of apoptosis or necrosis, but rather by *cornification* [75]. The corneocyte cell has no nucleus and is no longer metabolically functioning [4, 54]. This occurs when the cell transitions from the granular layer to the corneum. Cornified cells are strongly attached to each other at edges, and the cell sheets provide key contributions to barrier function [16, 54, 75]. The barrier functions to both keep external toxins out, and internal water and

solutes in [12, 75, 82]. An essential part of this barrier is the production and secretion of impermeable and insoluble lipids, which form between the granular layer and stratum corneum in extracellular spaces [16, 75]. The corneocyte-lipid composition is often described as a brick and mortar structure, where the corneocytes are the bricks and the lipids are the mortar [26].

Though the cell loses its nucleus at the granular-corneum interface, this does not mean the cell no longer undergoes changes to its mechanical and chemical characteristics. As the cell migrates through the corneum, it continues to transform through a variety of chemical reactions until it reaches the surface of the tissue [75]. Once it reaches the surface, it is lost through a process known as *desquamation*.

2.4.1 Desquamation

Desquamation is the process of shedding skin in sets of cells, also known as *squames* or scales, from the surface [37]. It is estimated that we lose 0.2–1.0 billion cells per day, with high variation between individuals [82]. This cell count is extrapolated from measured data from Roberts and Marks [104] who measured both passive desquamation—cell loss over 48 hours from a protected section of the epidermis, and forced desquamation—cell loss when a (shear) force is applied to the skin for 10 seconds. Passive desquamation generated cell loss rates of 6.5–13.1 $\times 10^2$ cells/cm^2/hr, while forced desquamation generated loss counts of 5.6–10.4 $\times 10^4$ corneocytes/cm^2 over the 10 second scrub. The variation indicates the range across different areas of the body. Given our epidermis is neither fully protected nor inflicted with sustained forces, the actual homeostatic rate is estimated to be between these two ranges.

Many processes must happen to the cell to enable desquamation. One crucial processes is the degradation of corneodesmosomes [82]. As described in Section 2.3, corneodesmosomes are adhesive protein complexes that hold the cell together in the stratum corneum. During its journey through the stratum corneum, the cell will eventually lose adhesion to surrounding cells via the degradation of these cor-

neodesmosomes. This has been seen through fissures in the outermost three or four layers [37]. Once sufficient degradation of the proteins has occurred, the cell can be lost from the tissue in a squame. This process is described in further detail in Chapter 7.

2.5 Subcellular machinery

In the previous sections, we have mainly discussed the IFE tissue at a microscopic scale ($1 - 100$ μm), covering cell properties and cell-cell interactions. The majority of cell processes, regulatory mechanisms, and mechanics are the result of processes happening at a sub-micron scale (< 1 μm). We also call this the subcellular scale, as it is occurring at scales much smaller than a cell (either within or between cells). An example of subcellular machinery are the proteins, such as desmosomes, as discussed in Section 2.3. Here, we will describe the concepts of signalling pathways and discuss the chemical gradients in the IFE and the subcellular dynamics of desquamation. A full understanding of cell signalling pathways is not necessary for understanding the methods and results of this thesis. However, a level of comfort with the concepts and terminologies of proteins and enzymes, and their roles in subcellular machinery will assist in appreciating the models and results presented in Chapter 7.

2.5.1 Signalling pathways

An important aspect of subcellular machinery are *subcellular signalling pathways*. Subcellular signalling pathways are sequences of protein interactions that occur within a cell, causing some sort of action to be taken by the cell. A common trigger for these signalling pathways is the binding of molecules onto *cell receptors* on the cell membrane. The attachment of the signalling molecule causes a cascade of interactions in the cytoplasm, often through to the nucleus, to trigger gene expression.

The signalling molecules activating these pathways could be attached to other cells and activate on cell contact, or cells can emit molecules to signal other cells at both short and long ranges [4]. For example, desmosomes are thought to be involved in signalling pathways relating to proliferation, differentiation, and cell death [55]. Another example, previously incorporated in IFE models in the literature (see Sections 3.2 and 3.3), is TGF-β (transforming growth factor β). TGF-β is a signalling molecule that is hypothesised to help regulate cell growth in differentiated epidermal cells [115]. Every activity performed by a cell is likely to occur due to a combination of multiple signalling pathways, making it a very complex system to understand.

2.5.2 Molecular gradients in the epidermis

There are many molecular gradients present in the epidermis. In Section 2.3 we discussed cell stiffness and adhesion gradients. As cells move up through the epidermis, the keratin levels inside the cell increase and this results in increased cell stiffness. Additionally, the adhesion proteins between cells change. Firstly as the cell moves up through the spinous and granular layers the adhesion proteins become more organised, before changing in structure and gradually decreasing in the corneum [4]. This is briefly described at a molecular level in Section 2.5.3 below and in further detail in Chapter 7.

A chemical gradient of interest for the study in Chapters 7 and 8 is the pH gradient in the corneum. The cells' extracellular environment is at a neutral pH at the start of the corneum, and becomes increasingly acidic towards the top of the tissue [88]. It is hypothesised that this is controlled by the activities of other enzymes [51], but that is outside the scope of this thesis.

Another gradient which has been widely investigated using mathematical models is the calcium (Ca^{2+}) gradient [21, 39, 118]. In the epidermis calcium increases in the lower layers and then decreases in the corneum [21, 29]. Calcium is known to

be a signalling molecule for the ERK-MAPK signalling pathway which is thought to regulate differentiation of keratinocytes [21]. Additionally, the calcium may be involved in the organisation of adhesion proteins [119], as discussed in Section 2.3.

2.5.3 Subcellular molecules in desquamation

In Chapter 7, a subcellular interaction is introduced to regulate desquamation. This is an enzyme reaction involving kallikrein serine proteases (KLKs), which are *proteolytic enzymes* [4]. Proteolytic enzymes are enzymes that induce the breaking down of proteins—in this case the proteins in corneodesmosomes. KLK enzymes bind to and degrade the corneodesmosomes between the cells in the stratum corneum [10, 22, 26, 75].

This reaction is regulated by LEKTI, an *inhibitor*. LEKTI binds with the KLK enzymes, which prevents them from binding to the corneodesmosomes, effectively reducing the degradation rate [32, 53, 66]. Both the KLK enzymes and the LEKTI are released by the cell into extracellular space as it transitions into the corneum [54]. Further regulation is provided by the pH gradient (see Section 2.5.2) which controls the rates of these reactions [22].

The degradation of the adhesion protein complexes between the cells is critical for the desquamation process. Further details on the interaction between the pH gradient, KLK enzymes, corneodesmosomes, and LEKTI can be found in Chapter 7.

2.6 Diseased epidermis

The main aim of this thesis is to understand the IFE in homeostasis, however understanding how the system can fail is also important. An appreciation of the different diseases of the IFE helps provide motivation for the work: once we have a working model of the healthy IFE it can be used to investigate and help understand disease. Diseases of the skin can range from a nuisance to a major health risk, with debili-

tating or even fatal consequences, and even the less severe diseases can have flow on effects for our health.

A majority of skin diseases cause malfunctions in the stratum corneum, causing either excessive or insufficient desquamation of cells. Excessive desquamation, or peeling, of the epidermis causes deficiencies in barrier function of the skin. This allows the ingress of antigens, resulting in inflammation and has been linked to allergic diseases such as atopic dermatitis (eczema), food allergies, or asthma [26].

A more severe example of a skin disease is JEB (junctional epidermolysis bullosa) which causes chronic skin wounds, recurrent infections, and blistering of the skin at the basal membrane. Approximately 3.6 children per million are born each year with JEB in the U.S. (data from 2007–2010) . Though the genetic mutations of JEB are known, there is no cure and almost half of children born with the condition die before adolescence [45, 61].

Another serious skin disease we will touch on is melanoma, the deadliest form of skin cancer. Melanoma develops first in the epidermis during what is known as the radial growth phase of the cancer. This stage of the cancer is treatable through surgery. Once the cancer cells begin to invade the dermis, survival rates drop to 53-97% (depending on disease stage) [42].

2.6.1 Netherton Syndrome

Netherton syndrome (NS) is the skin disease we use as an application for the model in Chapters 7 and 8. NS is a rare genetic disorder affecting the desquamation process. The estimated prevalence of NS is 1 in 200,000 [114] with varying severity in symptoms. These symptoms include ichthyosis (dry, thickened, scaly skin), hair defects, growth problems, pain and irritation in skin, and recurrent skin infections [32, 66, 114].

The result of the defective gene in NS patients is a reduction in the inhibitor LEKTI, resulting in premature desquamation in the corneum [32, 66, 114]. A de-

scription of LEKTI's role in the desquamation process can be found in Section 2.5.3 and in further detail in Chapter 7. Other potential roles of LEKTI in the epidermis are in immune and inflammation processes, and cell differentiation [114], but we do not consider these processes in our model.

2.7 Relevant experimental results

Throughout this thesis we use the results of several *in vivo* and *in vitro* experiments to parameterise our results and test the model. There are many challenges to experimental studies of the epidermis. As with many biological systems, data is commonly collected from *in vitro* or *in vivo* mice experiments. However, as was detailed in Table 2.1, mouse and human skin vary significantly, and hence any extrapolation of results from mice to humans may not be robust.

We use data from several *in vitro* experiments to parameterise the system developed in Chapter 7. This data often only studies a subset of the components and reactions that are actually occurring *in vivo*, often without knowing how biologically relevant the particular combination of components chosen is [17, 22]. Despite this, these studies must be used as it is often not possible to extract the information we need from humans *in vivo*. This is because most information cannot be determined noninvasively, though one exception is data such as epidermal water content that can be collected using radiation methods [27]. For example, it is not possible to measure the dynamics of a chemical reaction *in vivo*. Consequently, reaction rates must be determined from *in vitro* experiments of the hypothesised reactants [17, 22]. Data from *in vitro* experiments by Caubet et al. [17] and Deraison et al. [22] is used to determine rate parameters for the enzyme reaction in Chapter 7, and these are described in further detail in the Chapter.

Several experiments have collected *in vivo* data for human skin by taking skin samples from participants. For example, data can be collected by stripping the skin

using tape or adhesive resins [66, 88]. These experiments go as deep as the depth of the stratum corneum, which is the region relevant to the desquamation model used in Chapters 7 and 8. Komatsu et al. [66] use this procedure to determine the dry-weight concentrations of KLK enzymes in healthy and diseased (NS) subjects, Ohman and Vahlquist [88] use it to study the pH gradient in the skin, and Igawa et al. [49] use it to count the number of adhesion proteins present on cells. We use data from these studies to parameterise the ODE system developed in Chapter 7.

In vivo human data can also be collected from skin samples, taken either as a biopsy from volunteers or obtained during surgery. Examples of studies using skin biopsies—the results of which we use in Chapter 7—are the studies of epidermal cell and tissue morphology done by Al-Amoudi, Dubochet, and Norlén [7] and Bouwstra et al. [11], and the dry-weight concentration measurements of LEKTI fragments by Fortugno et al. [32].

One final *in vivo* human experiment that we use to test the model in Chapter 6 is a study by Goldschmidt and Kligman [37] on the desquamation of human epidermis. Participants covered an area of their skin with a cup continuously for 3–6 weeks. At the end of this time period loose cells were scraped off the top of the skin and the skin morphology was studied. The authors conclude that, after the scraping, the skin is in a healthy homeostatic condition. Additionally, removed cells are both easily scraped off and easily broken down into clumps, but not easily reduced to single cells.

2.8 Summary

This chapter has provided background into the structure and function of the interfollicular epidermis relevant to results of this thesis, and necessary for understanding the advantages and limitations of the model developed.

In summary, the IFE is a tissue that consists of four main layers, each themselves

consisting of further layers of cell sheets. The bottom layer, the basal layer, sits on an undulating membrane and is one of the two most important layers of the tissue as this is where all cell proliferation occurs in the tissue. In order to undergo proliferation, proliferative cells progress through a cell cycle, the last phase of which is the mitotic (M) phase, where the parent cell contracts through the middle and then splits. There is a lot of uncertainty around exactly how cells proliferate in the epidermis, in terms of both cell lineage and the symmetry of division.

The stratum corneum, at the top of the IFE, is composed of numerous sheets of very flat cells. This layer provides the main barrier function of the tissue, and consequently for our bodies. The middle two layers serve to reshape the cells from a basal cell to a cell that is able to assist with the barrier function of the stratum corneum. All cells in the system experience adhesion to other neighbouring cells and this adhesion plays a critical role in barrier function. However, in order for cells to be lost to the environment, they must undergo a process of desquamation. This process requires the adhesion between cells to degrade, via the activities of KLK enzymes with regulation by LEKTI, towards the top of the tissue in order to allow them to be lost from the top of the tissue.

This chapter has provided a summary of the background required to understand the base model we developed of IFE tissue, described in Chapter 4. Any further information required to interpret models or results will be discussed in the relevant chapter.

3 | Computational models of epidermal tissue

The last couple of decades has seen a number of spatio-temporal computational models of the epidermis emerge. These models enable investigations into the effect of individual processes, and interactions between processes, previously unavailable using experimental methods alone. This chapter provides a background to the methodologies and uses of mathematical models of the epidermis. It begins with an overview of the different modelling techniques that are commonly used to model biological tissues. This is followed by a chronology of multicellular models of the tissue and a discussion on the most recently published model. Finally, we summarise some insights into the epidermis found as a result of these models.

3.1 Mathematical models of biological tissues

In this thesis we develop and interrogate a mathematical model of the inter-follicular epidermis (IFE). Mathematical models, supported by experimental data and observations, enables us to test hypotheses that are difficult, expensive, or even currently unattainable to test *in vitro* or *in vivo*. In particular, they allow for a more holistic, or systems biology type, approach, where the effect of the interactions of different processes, sometimes at different spatial or temporal scales, can be investigated.

However, these models require simplification of the highly complex systems they aim to replicate. These simplifications are made due to either a lack of computational power or a lack of understanding about the system. Additionally, these models are often highly dependent on the availability and quality of the experimental data used to parameterise them.

3.1.1 Modelling techniques

Though many different models of biological tissues exist, they are all generally based on a handful of modelling techniques. Figure 3.1 outlines the more common techniques used in tissue modelling. These techniques can be categorised as continuum or discrete. Continuum methods model system variables, for example cell density, over a domain, such that the value of each variable is defined at any point in the domain. Discrete models define individual objects, such as individual cells, or discrete locations in space to describe a system, associate variables with each of these objects or locations, such as cell type or age.

Models are also characterised in Figure 3.1 by their scale: *multicellular models* or *subcellular models*. We define multicellular models as models that look at the collective (macroscopic) behaviour of a population of cells interacting with each other and with external stimulants or forces. Subcellular models model processes occurring at a lower spatial scale than the cell, such as protein interactions. The coupling of a multicellular and subcellular model is a *multiscale model*.

In this thesis we use a discrete overlapping spheres method, which is described in more detail in Chapter 4. We extend this model to a multiscale model with the addition of a mass action kinetics subcellular model in Chapter 7. We provide a brief overview of the different modelling techniques shown in Figure 3.1 below.

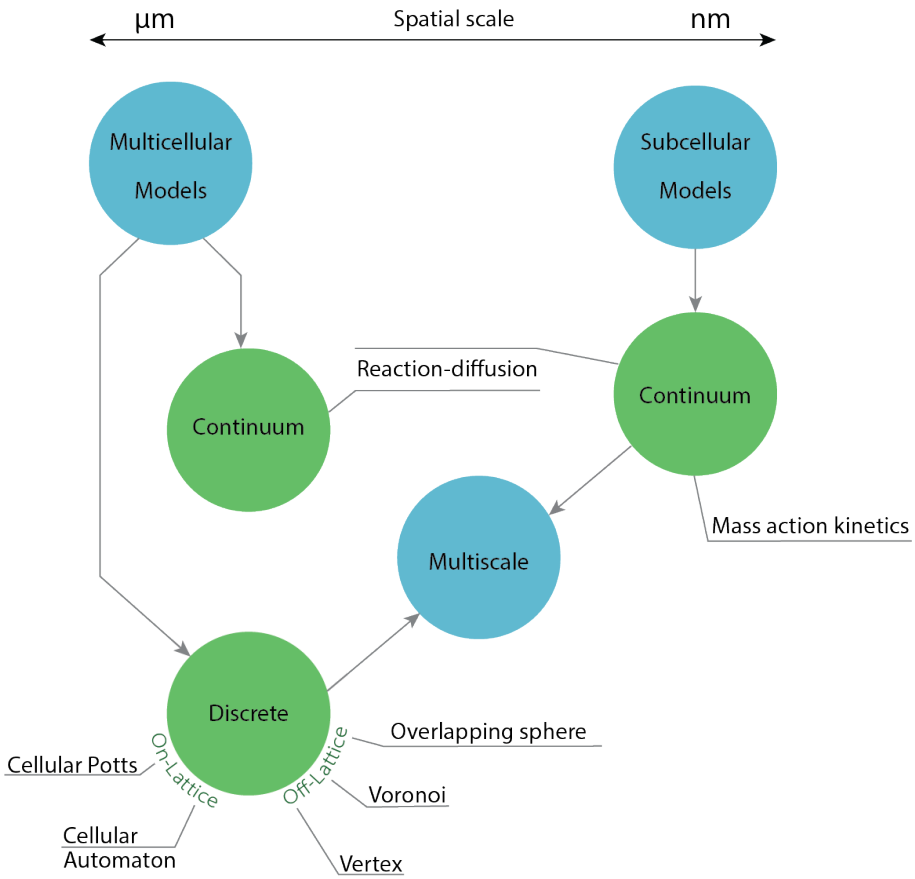

Figure 3.1: Some of the common modelling techniques used for biological tissue models. Arrows link model scales to modelling techniques. This is not a complete list of all modelling techniques and combinations—for example some reaction kinetics models, and subcellular systems more generally, use discrete methods. However, this diagram covers the most commonly used methods for epithelial tissues, and IFE tissue more specifically.

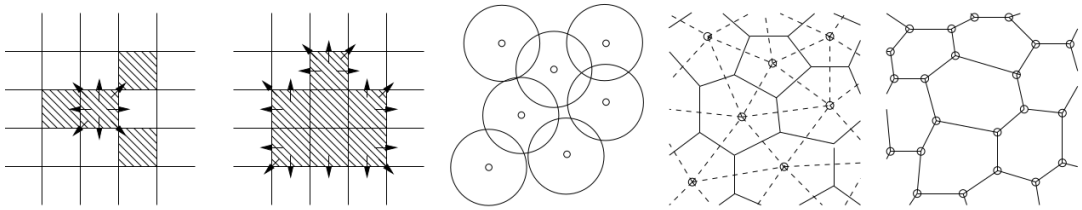

Figure 3.2: Examples of discrete multicellular modelling techniques: (a) cellular automaton; (b) cellular potts; (c) overlapping spheres; (d) Voronoi; and (e) vertex. (Image reproduced with permission from Osborne, J. M. et al. *PLoS Computational Biology* 13.2 (2017) [90]).

3.1.2 Discrete models of cell populations

Discrete models (also known as agent-based models), in the context of multicellular models, model each cell individually. This allows for populations of cells where the individual cells may be in different states. However, as a result, these models can require high computational effort. Discrete models can be split into two categories: on-lattice and off-lattice. On-lattice models prescribe a structure to the system, limiting cell positions to either lattice points or lattice sites. Examples of on-lattice models used to model epithelial tissues are cellular potts and cellular automaton [89, 3], shown in Figure 3.2. Cells move between lattice sites according to a set of rules. In the case of cellular potts, the cell is composed of several lattice sites, and in cellular automaton each cell is a single lattice site. The advantage of on-lattice methods are their computational simplicity and, in the case of cellular automaton, fast compute times [90]. The disadvantage of these models is that they impose an inherent structure on the tissue which can result in unrealistic mechanics [94].

Off-lattice models allow cells to move freely in space. Movement is determined by balancing the forces on a cell due to neighbouring cells and other external factors, such as boundary conditions. Examples of off-lattice techniques are Voronoi [90, 94], vertex [90, 126], and overlapping spheres [90, 94] methods.

As can be seen in Figure 3.2, Voronoi and vertex methods both model cells as polygons, but differ in the calculation of cell forces. Voronoi methods define cells by individual points for the cell centres, and are hence a *cell-centre based* method. The cell boundaries are defined by a Voronoi tessellation [122], and the equivalent Delauney triangulation between the cell centres is used to determine cell-cell forces [94]. The vertex method defines cells by a set of points which tessellate to form a tissue. Rather than calculating forces between cell centres, they are calculated for each vertex of the polygon defining the cell [126]. A disadvantage of both vertex and Voronoi methods is that extensions are required to remove the underlying connectivity assumption to enable cell separation. Further disadvantages of these two methods are their high computational times and the complexity of extending the models to three dimensions. A recent study by Osborne et al. [90] found the computational times of vertex and Voronoi methods in two dimensions were often at least twice those of overlapping spheres.

Overlapping spheres

Of the off-lattice models, the overlapping spheres method (also known as the particle based method) is the most efficient and easiest to implement in three dimensions [90, 94]. For this reason, it is the method we use for this thesis.

Overlapping spheres is another cell-centre based method, like Voronoi methods. Each cell is represented by a sphere (see Figure 3.2) and forces are calculated based on the distance between cell centres. Further detail on the methodology is provided in Section 4.1. The main disadvantage to the overlapping spheres method is the characteristic, potentially unrealistic, low density of the cell packings achieved, due to the somewhat unrealistic spherical shape of the cells. This disadvantage could potentially be mitigated with the use of deformable spheres, which have previously been implemented for small systems [34]. The overlapping spheres method has also been known to become unstable if there is not sufficient cell stiffness, however this

issue is easily overcome by careful force choice [94].

3.1.3 Continuum models of cell populations and subcellular dynamics

Continuum models are commonly used in both multicellular and subcellular systems. These models simplify the system by removing spatial granularity. For example, in the case of cell populations they remove the spatial granularity of the cells, locally averaging the population's properties over space and predicting tissue dynamics from this approximated system. The drawback to these methods is their inability to model the behaviour of cells at an individual level, but the benefit is their generally faster compute times.

As shown in Figure 3.1, an example of a continuum model that can be used in both multicellular and subcellular systems is reaction-diffusion. Reaction-diffusion models are systems of partial differential equations that are commonly used to predict the spread and interactions of a collection of bodies. In the case of multicellular systems this could be the spread of cell populations, such as in wound healing or tumour growth [35, 56, 111]. In subcellular systems this could be the spread of molecules, such as the diffusion of signalling molecules that regulate cell behaviours across the tissue [110].

Mass action kinetics

Another modelling technique of interest for this thesis is mass action kinetics, which is a technique used to model reaction kinetics. Reaction kinetics models of subcellular processes model the rates of interactions between subcellular molecules. These models usually consist of systems of differential equations (DEs) that can be used to predict temporal gradients of molecules. These DEs can also be used to determine spatial gradients, such as signalling molecules across a tissue, using a chemical

gradient as input and solving to steady state [21].

Mass action kinetics models derive a system of DEs using the law of mass action, in which the rate of a reaction is equal to the product of the concentrations of the reactants and a rate parameter. In this thesis, we will use mass action kinetics to model enzyme kinetics with competitive inhibition: a reaction between an enzyme and a substrate with an inhibitor that, by also binding with the enzyme, prevents the enzyme binding with the substrate [60]. The rate of the reactions for the two interactions (enzyme-substrate and enzyme-inhibitor) can be approximated using mass action kinetics. Under certain conditions the resulting system of DEs can be simplified, for example through the use of the quasi-steady state assumption [60, 87]. In the reaction described here however, though it is possible to find a solution the enzyme-substrate and the enzyme-inhibitor reactions separately using the quasi-steady state assumption, this is not possible for the combined reaction system. The mass action approach to enzyme kinetic models, and how we apply it to our system, is discussed in detail in Chapter 7.

3.1.4 Multiscale models

The goal of a multiscale model is to incorporate processes happening at different scales, thus enabling an increased understanding of the interplay between them. In the context of modelling biological tissues this generally involves incorporating models of signalling at a subcellular level to inform activities at a cellular level. For example, in the intestinal crypt, another epithelial tissue, Van Leeuwen et al. [120] include a model of intracellular signalling pathways, triggered by an external gradient of Wnt (a signalling pathway) factors, to regulate the cell cycle and cell-cell adhesion in a multicellular Voronoi model.

As shown in Figure 3.1, in multiscale models (that is coupled subcellular and multicellular) the multicellular model is generally discrete and the subcellular model is continuous and solved individually for each cell [2, 120]. Often the processes at the

different spatial scales also occur at different time scales, with the subcellular process having to be solved at higher temporal resolutions than the multicellular ones [65, 120]. Consequently, the main obstacle to multiscale models is computational, with the requirement for different time scales adding significant computational complexity, and the requirement for the subcellular model to run independent solutions for each cell adding significant computational effort, though it has the potential for parallelism.

3.2 Towards an in silico model of the IFE

Several *in silico* models of the IFE have emerged in recent decades, predominantly using methodologies similar to the overlapping spheres method. Early models were two dimensional and, as computational power increased over time, these models were expanded to three dimensions, which simultaneously caused significant increases in system size and computational effort. Figure 3.3 shows a chronology of some key developments in IFE models in the last 25 years along with the increase in the system sizes considered. Table 3.1 provides details of all overlapping spheres models of the epidermis, and the tissue property they have been used to study. In this section we focus only on discrete multicellular or multiscale models of IFE tissue and outline how these models have been able to reproduce known behaviours of the tissue. The novel insights into the IFE from these models are detailed in Section 3.3.

As seen in Figure 3.3, the first spatial multicellular model of the IFE was developed in 1995 by Stekel, Rashbass, and Williams [113]. The authors used an overlapping spheres type model in two dimensions, with an undulating membrane, and incorporated signalling by assuming signalling factors spread from cells according to the inverse square law. This model was presented as proof that such a system could reproduce realistic IFE tissue structure, and demonstrated the method was able to recover from a wounding perturbation. The model was then used to in-

Year	Citation	Cell shape	Multicellular framework	Subcellular framework	Subcellular model	Biological application
1995	Stekel, Rashbass, and Williams [113]	Circles	-	-	Inverse square law	-
2005	Grabe and Neuber [39]	Circles	-	-	Molecular transport	Generating a flat surface from an undulating membrane
2007	Schaller and Meyer-Hermann [108]	Spheres	-	-	-	Water's role in homeostasis, and cancerous melanocyte persistence
2009, 2010	Sun et al. [115], Adra et al. [2]	Spheres	FLAME	COPASI	Mass action ODE	Role of TGF-β in wound healing
2013	Li et al. [72]	Spheres	FLAME	-	-	Cell lineage hypotheses
2013	Sütterlin et al. [117]	Spheres	EPISIM	COPASI		-
2015	Zhang et al. [127]	Ellipses	-	-	-	Causes of psoriasis
2016	Kobayashi et al. [65]	Spheres	-	-	Phenomenological ODE	Calcium's role in homeostasis
2017	Sütterlin et al. [118]	Ellipsoids	EPISIM	-	Molecular transport	Maintenance of the calcium gradient

Table 3.1: Previous models of the epidermis using an overlapping spheres technique. Provides details of each model and the property of the epidermis the model was applied to.

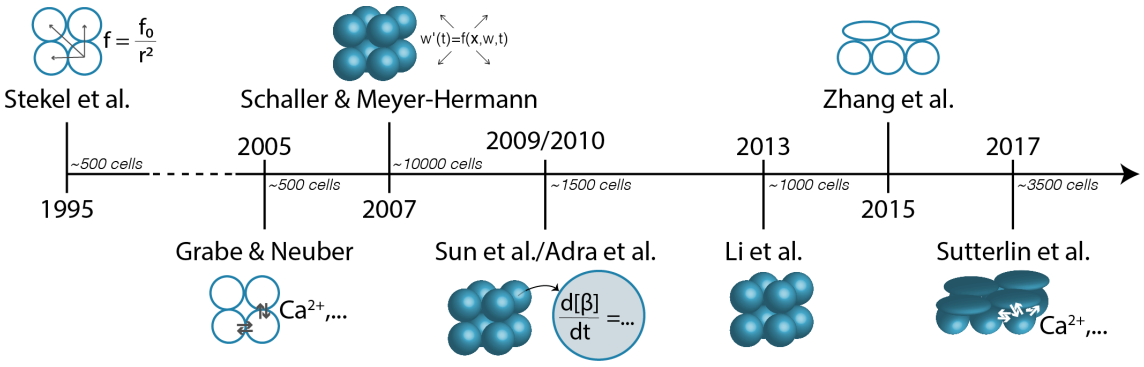

Figure 3.3: A brief chronology of the advancements in multicellular overlapping spheres models of the IFE. More details on these models and their uses are given in Table 3.1.

vestigate mutations that produced behaviours seen in different epidermal diseases [101].

In 2005, a decade after Stekel, Rashbass, and Williams [113], Grabe and Neuber [39] also used an overlapping spheres type methodology in two dimensions with an undulating membrane. The main difference in this model was the inclusion of the transportation of molecules between cells. Water was transported by exchange between neighbouring cells. Calcium ions and lamella units were also transported along with the water. The lamella units converted to lipids which created a barrier to block calcium loss from the surface. This model was a proof of concept that such a system could reproduce a horizontally layered system, starting on an undulating membrane and flattening towards the surface, as well as realistic cell turnover times and calcium gradients. The authors also showed this model could reproduce properties of psoriatic epidermis (a common skin condition) with extended proliferation of transit amplifying cells [40]. This model would later be developed further and become known as EPISIM, which we will discuss below [117].

As seen in Figure 3.3, the next key development for IFE models was an extension into three dimensions. In 2007 Schaller and Meyer-Hermann [108] implemented a three dimensional epidermal model which included cell growth during division,

degrading adhesion, and an extracellular reaction-diffusion model of water and nutrients to regulate division timing. Their model simplified the basal membrane to a flat surface, rather than the undulating membrane used by Stekel, Rashbass, and Williams [113] and Grabe and Neuber [39]. The model was used to investigate both diffusion as a control mechanism and the persistence of melanoma cells in the tissue with low, or no, basal adhesion and varying proliferation rates.

Two other early three dimensional multicellular IFE models—Sun et al. [115] and Adra et al. [2] (model published across two papers) in 2009/2010, and Li et al. [72] in 2013—used a modelling framework called FLAME which had previously been used to model the self-organisation of keratinocytes in culture in three dimensions by Sun et al. [116]. Both models used a flat basal membrane. The Sun et al. [115]/Adra et al. [2] model also included coupling with a subcellular reaction network model using the COPASI framework [46]. COPASI solved a set of ordinary differential equations (ODEs) within each cell, based on a mass action model for TGF-β signalling presented in Vilar, Jansen, and Sander [121], which regulated cell adhesion, division, and proliferation. The authors included TGF-β as a signalling molecule to regulate the re-epithelialisation process, that is the restoration of the epidermis after injury [115].

This FLAME-COPASI coupling was closely followed by the coupling of EPISIM to COPASI in 2013 by Sütterlin et al. [117] (not shown in figure). The goal of the EPISIM-COPASI model was to build a platform that allowed easy incorporation of subcellular processes via a graphical user interface. The would enable users with less computational expertise to build multiscale models in either two or three dimensions.

Now that systems were routinely developed in three dimensions, the next progression was the implementation of non-spherical cell shapes. In 2015, Zhang et al. [127] published a two dimensional model using elliptical cell shapes with an undulating membrane. This model also used a variation on the traditional approach to cell population kinetics. Rather than the proliferation and differentiation being

determined for individual cells, the authors determined the cell population kinetics using an external compartmental model, which then triggered proliferation and differentiation events the multicellular model. This two dimensional model was followed closely by Sütterlin et al. [118] in 2017, who implemented ellipsoids in three dimensions using EPISIM (without COPASI coupling). In both the Zhang et al. [127] and Sütterlin et al. [118] models the forces were modified to incorporate the new cell morphology, although the implementation did not include any rotation. The Sütterlin et al. [118] model extended the work of Grabe and Neuber [39] by including water and calcium diffusion and barrier formation through molecule exchange between neighbouring cells, as well as desquamation by decreased adhesion and an adhesion threshold.

A slightly different approach to the subcellular model, studying calcium gradient effects, was presented by Kobayashi et al. [65] in 2016. The model incorporated a phenomenological based, subcellular ODE model of calcium into an overlapping spheres multicellular model. The calcium model, detailed in Kobayashi et al. [64], was developed based on experimentally observed behaviours of calcium waves. The authors had previously done a similar study on calcium in IFE tissue, but using a reaction-diffusion multicellular model rather than a discrete model [63].

All the models mentioned above used an overlapping spheres type methodology. Two other discrete models that have been used to model the epidermis are the subcellular element model (SEM) and Voronoi. In SEM models, each cell is composed of multiple elements, hence enabling anisotropic behaviour. This method, implemented in three dimensions, was used by Gord et al. [38] in 2014 to model stratification during development. Their model was extended to include calcium diffusion, modelled on a regular grid, to regulate basal cell division and differentiation rates by Du et al. [25] in 2018.

The Voronoi method was used in 2014 by Hu and Cucinotta [48] to model IFE response to radiation. They model was built using Chaste [96], which we describe

in detail in Section 4.3. The Hu and Cucinotta [48] model included subcellular signalling models to regulate cell differentiation or cell cycle time, based on models previously developed in Chaste for similar purposes in intestinal crypt models by Van Leeuwen et al. [120] and Mirams [83].

Many of the studies described here aimed to reproduce observed tissue structures or experimental data. The overall goal of these models is generally either to generate a full model for use as an experimental alternative, or as a complement to experimental work. In some cases these models have already been used to gain insights into the system, which we detail below.

3.2.1 The current state of the art in IFE models

The different models that we have described above vary in both their applications and their limitations. Here we will focus on the Sütterlin et al. [118] model in more detail, as it would arguably be considered the state of the art in the field. This model is unique as it models cells as ellipsoids instead of spheres.

In the Sütterlin et al. [118] model cells undergo three differentiation steps: proliferative to spinous cell to granular cell to corneocyte. At each differentiation step the cell becomes progressively flatter, so there are four predefined cell shapes. The first differentiation step, from proliferative to spinous cell, occurs when the cell loses contact with the basal membrane. The cell lineage used in this model is the hierarchical, or stem-transit amplifying, cell lineage hypothesis.

The adhesion function between cells in the Sütterlin et al. [118] model is proportional to the overlap and contact area. Consequently anisotropy in the adhesion, due to the cell shapes, is inherently included in the model. However, anisotropy in adhesion due to a variation in the distribution of adhesion molecules is not. Cells also undergo a degradation of adhesion when they are corneocytes. Cells are then removed when their total adhesion to surrounding cells drops below a threshold.

Sütterlin et al. [118] included a subcellular model for the transport of water

and calcium. These molecules are exchanged between neighbouring cells. They enter the system through diffusion from the basal membrane, and are lost due to evaporation at the tissue surface. It is the water and calcium content that regulate the division and differentiation timings of the cells. An additional component in the subcellular model is the production of lipids and tight junctions by the granular cells and corneocytes. These increase the barrier function of the system, which helps prevent water, and calcium, loss.

The Sütterlin et al. [118] model was qualitatively compared to experimental studies to ascertain whether the system produces realistic tissue morphologies. Though the model was able to produce a self-regulating tissue that reflects experimentally observed properties, some parameters were chosen based on the model results, rather than using experimentally derived data. Consequently, it is not possible to say the model concretely proves that the included subcellular dynamics and cell morphologies are sufficient to explain the emergent tissue morphology. These parameter decisions were likely required due to a lack of available experimental data for all the parameters required for this model—as with many models, an increase in complexity means less of the model is able to be parameterised with appropriate data.

It is expected that ellipsoidal morphologies would provide improved packing characteristics compared to spherical cells. However, this may not be true at the interface between cell layers, where there is a discontinuity in cell shapes. It could be expected that these interface regions would also be problematic if cell rotation is ever introduced into the model, as the rounder cells in the layer below may cause rotation of the flattened cells above.

A final disadvantage of a model that includes high levels of detail, in particular ellipsoidal cell shapes, is the extra computational time required. Sütterlin et al. [118] state that a single simulation, with a population size of around 3,000 cells, takes 3–3.5 days to run 20,000 time steps on their machine ("Intel Nehalem E5520 CPU, 2.26 GHz, 16 physical cores, 12 GB RAM and 16 parallel simulation threads").

This is a huge computational cost if the intention is to run parameter sweeps, or a significant number of realisations to account for stochasticity. In comparison, the multiscale model developed in this thesis (Chapter 8) takes around 2–2.5 days to run a simulation with around 2,000 cells for 172,800 time steps on a single core (Gen9 Intel Xeon E5-2683v4, 2.1GHz, 16-core).

3.3 Insights into the IFE from in silico models

In silico models have been shown to be useful in investigating different and sometimes contradictory hypotheses, resulting from a range of *in vivo* and/or *in vitro* studies. For example, Li et al. [72] used their model to investigate the dynamics of opposing cell lineage hypotheses from the experimental literature and compare their relative reliability. We divide the *in silico* studies into two groups: investigations into the effect of different hypotheses on tissues structure, and investigations into the effect of different signalling molecules. The studies that use an overlapping spheres technique are also summarised in Table 3.1.

3.3.1 Cell behaviours and tissue structure

A common theme in the computational modelling literature is the effect of different cell behaviours on tissue structure. We discuss five studies in this category: Schaller and Meyer-Hermann [108] on the impact of basal adhesion on cancerous melanocytes, Li et al. [72] on the impact of cell lineage on colony development, Gord et al. [38] and Du et al. [25] on the stratification of the tissue during development, and Zhang et al. [127] on modified cell proliferation and differentiation kinetics resulting in psoriatic tissue. These studies aim to either understand which cell behaviour hypothesis produces the most realistic structures or determine the behaviours causing diseased tissue structure.

Schaller and Meyer-Hermann [108] included a reaction diffusion model of extra-

cellular water in their IFE model to regulate cell proliferation, and used the model to investigate how cancerous melanocyte cell adhesion to the basal membrane affected the persistence of the cancerous cells. The study first determined that the water and nutrient gradient was sufficient to maintain a homeostatic tissue. They then performed a parameter investigation on the melanocytes' basal adhesion and proliferation rate. The results indicated there is minimal dependence on basal adhesion, but the proliferation rate determines the likelihood with which the cancerous cells persist. At high proliferation rates the cancerous cells will always persist, whilst at lower proliferation rates they will not. Between these two extremes they found a region where stochasticity and other effects determined persistence.

Li et al. [72] used the FLAME,an agent based modelling framework, to investigate the effect of cell lineage hypotheses on cell colony development, both in homeostasis and after wounding. An *in silico* model is an ideal candidate for this type of investigation as it is simple to track colony development, a property which is difficult to track *in vivo*. In particular, *in silico* models can provide as many data points as desired, both in terms of number of colonies and time points. The three lineage hypotheses investigated were the traditional TA hypothesis, the Clayton et al. [19] hypothesis, and the Mascré et al. [74] hypothesis, each of which is described in Section 2.2. The results of the Li et al. [72] model supported the Mascré et al. [74] hypothesis, as it was able to explain behaviours observed experimentally.

In silico models are very useful tools to understand the effects of different processes, as it is easy to turn individual processes on or off. This was the approach taken by Gord et al. [38] and Du et al. [25], using an SEM model as described above, to investigate how stratification of the different epidermal layers occurs during development. Gord et al. [38] studied basal and suprabasal layer formation with different division and adhesion rules: symmetric division with or without polar adhesion; or symmetric division with a switch to asymmetric division, again with or without polar adhesion. In the case of polar adhesion, basal regions of cells only

form adhesions with the basal regions of their neighbours. All symmetric divisions produced two proliferative cells and occurred parallel to the (flat) basal membrane, with detachment causing differentiation, while asymmetric divisions were perpendicular to the membrane with the differentiated cell placed above the proliferative cell. Their results showed the most robust hypothesis is polar adhesion with a switch to asymmetric division. This work was extended in Du et al. [25] to model development of all four IFE layers. In this study the authors considered the effect of asymmetric division with polar adhesion, increased adhesion between the same cell type, and long range signalling with extracellular calcium diffusion. The results indicated all the tested processes contributed to layer formation, and asymmetric division with polar adhesion was still the most crucial.

The final study, Zhang et al. [127], related to cell behaviours and tissue structure in diseased IFE, used a cell kinetics-elliptical migration model to study psoriasis. Psoriasis is an epidermal disorder hypothesised to be caused by hyperproliferation, immune system disorder, or both. Their psoriatic tissue model consisted of two subpopulations of cells: normal and psoriatic. These two populations divided, differentiated, and underwent apoptosis at different rates and, in the case of stem cells, with different dynamics which included immune system interaction. The authors found their model predicted two psoriatic tissue states: a diseased state with hyperproliferation where diseased stem cells dominated the proliferation and the immune response was insufficient to manage them, and an asymptomatic state where normal stem cells dominate. They also considered the impact of UVB irradiation treatment, which causes apoptosis of proliferative cells, and found, if correctly managed, a tissue in the diseased state could switch to an asymptomatic state.

3.3.2 Studies of signalling molecules

The second theme in the computational modelling literature is the effect of signalling molecules on tissue structure and behaviour. We discuss four studies here: Sun et

al. [116] on pattern formation in culture at different calcium concentrations; Sun et al. [115] on the role of TGF-β in wound healing; Sütterlin et al. [118] on the maintenance of the calcium gradient in IFE tissue; and Kobayashi et al. [65] on the effect of calcium on tissue stability. While experimental studies are useful to determine the different characteristic behaviours due to signalling molecules, *in silico* models are useful for understanding the interactions of each of these behaviours and the resulting system behaviour.

Sun et al. [116], using FLAME like Li et al. [72], investigated pattern formation of keratinocytes using a three dimensional *in silico* model of cell culture at low and physiological calcium. The authors found evidence that the 'transit amplifying' cells in the culture did not have a limited division ability, but rather the observed low number of divisions was due to space limitations at low calcium levels, or other colony size limiting parameters of the system at physiological calcium levels.

Sun et al. [115] then used the FLAME-COPASI coupled model to investigate the role of TGF-β in wound healing. TGF-β has shown contradictory roles *in vivo* and *in vitro* in relation to cell migration and proliferation. Their model indicated TGF-β only affected migratory cells at the wound front, and supported a role of TGF-β in maintaining a balance between migration and proliferation during wound healing. However, the authors state that more data is necessary to produce critical insights.

The final two studies we will discuss here, also investigating calcium diffusion and signalling effects, are Kobayashi et al. [65] and Sütterlin et al. [118]. The Kobayashi et al. [65] study used a multiscale model to investigate how homeostasis of the tissue is regulated by calcium. They determined that calcium dynamics particularly helped provide spatio-temporal stability to the stratum corneum.

The Sütterlin et al. [118] study looked at how the calcium gradient is maintained in the tissue. Sütterlin et al. [118] used an ellipsoidal implementation of the EPISIM model to investigate this question, extending the previous investigation in two di-

mensions by Grabe and Neuber [39]. Their results showed restriction of diffusion and transport at a local level in the granular layer and stratum corneum is necessary to maintain the gradient.

3.4 Summary

The use of computational models to investigate inter-follicular epidermis is a relatively recent development in biological research. Over the past couple of decades these multicellular models have steadily increased in size and complexity, moving from two dimensional systems of roughly 500 cells [39, 101, 113] to three dimensional systems with over 3500 cells and heterogeneous cell morphologies [118].

Most multicellular IFE models have been based on overlapping spheres type methodologies and have included some implementation of subcellular processes. The incorporation of these subcellular processes has also increased in complexity, starting with inverse square approximations [113], moving to cell-cell transfer [39, 118], then to mass action ODE models [2, 115] or phenomenological ODE models [65]. In this thesis, we will use a similar coupled overlapping spheres and mass action kinetics approach to investigate the self-regulation of tissue thickness in the epidermis—a topic yet to be studied using computational models. In doing so, we further extend mechanisms used in previous multicellular models, and develop a novel ODE model of desquamation for inclusion as a subcellular model.

The development of these IFE models allows for novel investigations into hypotheses that have previously been inaccessible to experimental biologists. This is often due to their ability to incorporate a range of behaviours and to turn behaviours or processes on and off, enabling the understanding of the individual contributions of each behaviour and the resulting characteristics of the tissue.

In the future, these models will likely continue to grow in complexity and size. Additionally, as increased and improved experimental data becomes available, it

will be possible to provide more specific insights into the tissue. Eventually, the systems could reach a point where they can be interrogated for the potential effects of treatments or other factors, reducing the need for other, more expensive and complicated experiments such as experiments involving animals or clinical trials.

4 | A Mechanistic Model Of IFE Tissue

In this chapter, we present the base model used in this thesis to simulate the inter-follicular epidermis (IFE). Some material in this chapter reproduces content from a paper in preparation which is currently available on arXiv (Miller, Crampin, and Osborne [81]). The IFE tissue is simulated using an overlapping spheres multicellular tissue model combined with a rule based model for cell fate decisions. This model combines and builds upon components of previous models in the literature. The main components of the model are the forces, the boundary conditions, including cell removal, and cell proliferation. Cell movement through the tissue is primarily upwards, as a result of increased volume at the base of the tissue due to the proliferation in the basal layer. This chapter gives details on each of these components as well as the code framework, Chaste, in which the model is implemented.

4.1 Overlapping spheres model

The modelling methodology we use is an overlapping spheres model (sometimes called a point based method). This model was chosen for several reasons: reasonable computational times; ease of implementation in three dimensions; no model extensions required to implement cell separation (important when modelling desqua-

mation in Chapters 6 and 8); and the ease of implementation of heterogeneous cell populations, either predetermined or due to a subcellular model.

An overlapping spheres model is an agent based method which represents each cell as a sphere. As described in Section 2.3, cell shape changes as a cell moves through the epidermis, with cells becoming increasingly flat in the higher layers. Though other models have previously included this shape change [118, 127] (see Section 3.2), we do not include this in our model. This simplification will affect the packing densities and tissue height results in Chapters 6 and 8. However, given the many simplifications required to build the model, and the lack of parametrisation data for many aspects of the model, the majority of results presented in this thesis aim to investigate the qualitative changes to the tissue. Hence the use of spherical cells is preferred due to its computational efficiency and model simplicity.

Cells in the model are able to move freely in space. Movement of each cell in the model is determined by the forces it experiences due to interactions with neighbouring cells, or other external forces that are applied to the system. The sum of all forces on the cell is balanced with the cell drag to determine the movement. We assume motion is overdamped, that is, cell inertia is not included, as the inertial force term is assumed to be negligible compared to the other forces [24, 76, 94]. This gives us the equation of motion:

$$\eta \frac{\mathrm{d}\mathbf{c}_i}{\mathrm{d}t} = \sum_{j \in N_i} \mathbf{F}_{ij} + \mathbf{F}_{i,\mathrm{ext}} \ , \tag{4.1}$$

where $\mathbf{c}_i$ is the cell centre location of cell i; N_i is the set of neighbours of cell i; $\mathbf{F}_{ij}$ are the forces on cell i due to interacting neighbour cell j; $\mathbf{F}_{i,\mathrm{ext}}$ are any external forces acting on cell i such as adhesion to the membrane or rotation; and η is the viscous drag coefficient for the cell [94].

There are five types of forces a cell can experience in our model: adhesive cell-cell, repulsive cell-cell, adhesive cell-membrane, division forces, and removal forces. The adhesive and repulsive cell-cell forces are described in Section 4.1.1 and the cell-membrane forces in Section 4.1.2. Division and removal forces are not included

in the base model, and so are described in their relevant chapters (Sections 5.2.1 and 6.2.1). All distances in this the model are calculated in units of a characteristic cell diameter (CD), which we take to be 10 μm [94].

4.1.1 Cell-cell forces

There are two cell-cell forces we include in our base model: adhesion and repulsion. The adhesion force represents the cell-cell adhesion and also the cell stiffness under tension. The repulsion force represents the cell stiffness under compression. As described in Section 2.3, both the cell stiffness and cell-cell adhesion change as the cell moves through the system. For now we ignore these changes, though later in Chapters 6 and 8 we will add an adhesion gradient to the model. Including these gradients in the base model would change the tissue density profile, and consequently also the tissue dynamics, but would not qualitatively change the results presented here.

The force magnitudes are calculated as a function of the interaction distance between the two cell membranes. This distance can be either a separation or an overlap. If we have two cells, cell i and cell j, with cell centre positions $\mathbf{c}_i$ and $\mathbf{c}_j$ respectively, we define their interaction vector $\mathbf{s}_{ij}$:

$$\mathbf{s}_{ij} = s_{ij}\mathbf{n}_{ij}, \tag{4.2}$$

$$\text{where } s_{ij} = \|\mathbf{c}_j - \mathbf{c}_i\| - r_{ij}, \tag{4.3}$$

$$\text{and } \mathbf{n}_{ij} = \frac{\mathbf{c}_j - \mathbf{c}_i}{\|\mathbf{c}_j - \mathbf{c}_i\|}, \tag{4.4}$$

where r_{ij} is the *spring length* between cells i and j. The spring length between two cells is the separation distance (distance between cell centres) at which they experience zero force. This is almost always assumed to be when two normal cell membranes are just touching, i.e. $r_{ij} = 1$ CD. The only exception is during division, which is discussed in Section 4.2.1.

The interaction distance, s_{ij}, can be either positive or negative, according to

whether the cell spheres are separate or overlapping. The sign of s_{ij} determines which cell-cell force is experienced by each cell:

- if $s_{ij} > 0$ the cell membranes are separated and the adhesion force applies;
- if $s_{ij} = 0$ the cell membranes are touching and no force is experienced by either cell;
- or if $s_{ij} < 0$ the cell membranes are overlapping and the repulsion force applies.

These interactions are shown in the diagram in Figure 4.1. The adhesion and repulsion forces used are described below. Note the exact form of the forces is only important for maintaining stability of the system. As long as they ensured stability, different functions, for example linear forces, would not be expected to qualitatively change the results.

Adhesion force

The first cell-cell force is the adhesion force, which the cells experience when $s_{ij} > 0$. The adhesion force represents the effects of the adhesion proteins (described in Section 2.3) between neighbouring cells. We base our force function on the function used in Li et al. [72]. The force increases for a short distance as cells separate, peaking at $s_{ij} = 0.15$ CD before decreasing and asymptoting to zero. The initial increase represents the force from the adhesive proteins at short distances, then the decrease is due to the breaking of the adhesive proteins as the cells separate further. We also define a cut-off distance for the adhesion force, to increase computational efficiency and as the cells would no longer be connected by any proteins.

The adhesion force function, for $s_{ij} > 0$, is

$$\mathbf{F}_{ij}^{\mathbf{A}} = -\alpha \left(\left(s_{ij}^{*} + c \right) e^{-\gamma \left(s_{ij}^{*} + c \right)^2} - c e^{-\gamma \left(s_{ij}^{*2} + c^2 \right)} \right) \mathbf{n}_{ij}, \tag{4.5}$$

$$\text{where } c = \sqrt{\frac{1}{2\gamma}}, \tag{4.6}$$

$$\text{and } s_{ij}^{*} = \frac{s_{ij}}{r}, \tag{4.7}$$

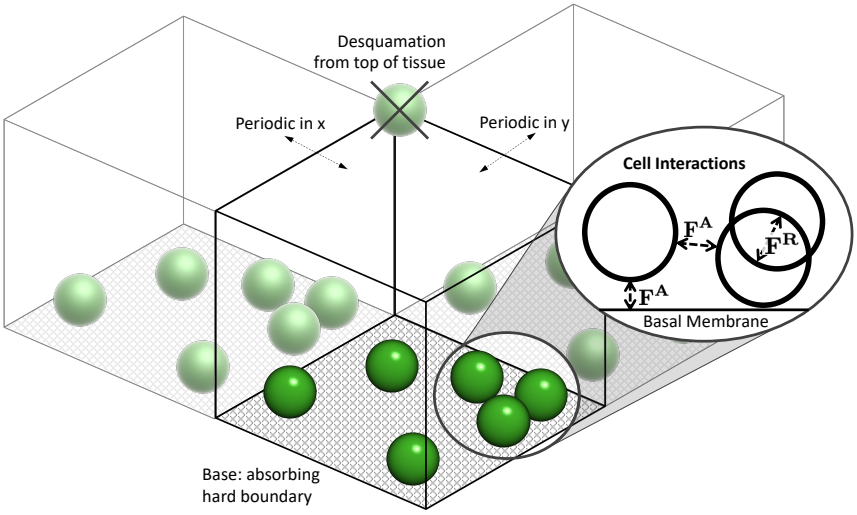

Figure 4.1: A diagram showing the simulation domain and, inset, the interaction forces experienced by the cells. If cells are separate they experience adhesion forces $\mathbf{F}^{\mathbf{A}}$, while if they overlap they feel repulsive forces $\mathbf{F}^{\mathbf{R}}$. Cells can also feel adhesion forces to the basal membrane. The domain is periodic in both x and y for three dimensional simulations. The basal membrane is the boundary at the base, and cells are removed from the top.

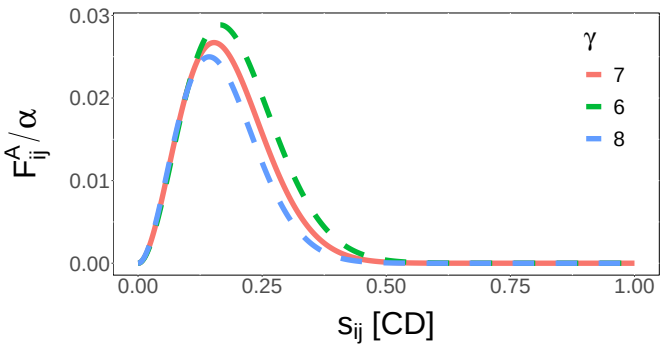

(a) Adhesion force

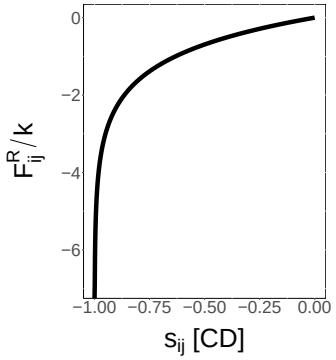

(b) Repulsion force

Figure 4.2: The shape of the magnitude of the force functions between two cells. (a) The short range adhesion force, also showing the effect of modifying the γ parameter in the adhesion force equation Equation (4.5). Here we use $\gamma = 7$ (solid line in graph). (b) The repulsion force when cells overlap.

where α is the adhesion force coefficient, γ is the shape parameter [72], and r is the characteristic cell radius, here $r = 0.5$ CD. Unless otherwise stated, we use the parameters used in Li et al. [72]: $\alpha = 0.2$ μN and $\gamma = 7$. The shape of the adhesion force can be seen in Figure 4.2a.

Repulsion force

The second cell-cell force is the repulsion force, which applies when the cell centres are closer than their spring length ($s_{ij} < 0$). For normal, non-dividing, cells this is when the cell membranes start to overlap. The repulsion force is to account for the conservation of volume of the cells. For the repulsion force, we use a logarithmic function from Atwell et al. [9]:

$$\mathbf{F}_{ij}^{\mathbf{R}} = k \log\left(1 + s_{ij}\right) \mathbf{n}_{ij}, \tag{4.8}$$

where k is the repulsive spring constant. We set $k = 150$ μN, as in Meineke, Potten, and Loeffler [76]. Meineke, Potten, and Loeffler [76] use this value to study intestinal crypts, another epithelial tissue, rather then epidermal cells. However, this value is

not known for the epidermis and the value of $k = 150$ μN ensures the stability of the system, therefore we use it here.

As can be seen in Figure 4.2b, the absolute magnitude of the repulsion force is much larger than the adhesion force. Substituting the coefficients of the force (Equations (4.5) and (4.8)), the repulsion force is around 5 orders of magnitude larger than the adhesion force. This is to avoid over-crowding and instability in the system [94].

4.1.2 Boundary conditions

Simulations are run in three dimensions and so there are six boundaries to the domain. These can be seen in the diagram in Figure 4.1. If we define positive z as the direction from deep epidermis to superficial epidermis, $z = 0$ is the basal membrane and $z = H$ is the top of the tissue. The conditions for each of these boundaries are described below.

The x and y directions are the horizontal directions, both of which have periodic boundaries. We use periodic boundaries as the tissue in the horizontal directions is much larger than is feasible to simulate. We limit the horizontal dimensions to 10 cell diameters, or 100 μm, to provide sufficient representation of the system, whilst avoiding excessive computational times. This is similar to the domain sizes used by Li et al. [72] and Sun et al. [115].

Basal membrane

The base of the tissue, $z = 0$, is bounded by the basal membrane. Though the basal membrane is undulating in the human IFE (see Chapter 2), we model it as a flat boundary for simplicity. In the model this is an *absorbing hard boundary*. If a cell overlaps with the basal membrane, it is immediately moved vertically back to the membrane, with a small perturbation added. The magnitude of this perturbation is stochastic and uniformly distributed ($\epsilon \sim U(0, 0.05)$ CD) [120]. The perturbation

stops crowding of the basal layer. Using a hard boundary can cause overcrowding as cells experiencing downwards forces due to crowding are placed back in the crowded layer.

In addition to a the no-overlap boundary condition, proliferative cells that separate from the membrane are attracted back down towards it. This is implemented as an *attachment force*. An attachment force will only occur if a cell has previously been in contact with the membrane. Contact occurs if the cell touches the membrane or is moved by the membrane boundary condition. When this occurs, the location of contact, $\mathbf{m}_i = (m_{ix}, m_{iy}, 0)$, is stored by the cell. The cell then experiences an adhesion force towards this contact position. The membrane adhesion force function is a modified version of the adhesion force between two cells which was given in Equation (4.5). Firstly, the adhesive coefficient, which we will refer to as α^* for membrane adhesion, is much higher than the adhesion coefficient between cells as the adhesion complexes between basal cells and the membrane are different to those between cells, as detailed in Section 2.3. We use $\alpha^* = 500$ μN, as in Li et al. [72], unless otherwise specified. Secondly, we replace s_{ij} and $\mathbf{n}_{ij}$ with s_{im} and $\mathbf{n}_{im}$, defined as:

$$s_{im} = \|\mathbf{c}_i - \mathbf{m}_i\|, \tag{4.9}$$

$$\mathbf{n}_{im} = \frac{\mathbf{c}_i - \mathbf{m}_i}{s_{im}}, \tag{4.10}$$

such that the adhesion force pulls the cell back towards its attachment point. Again, the force has a cut-off distance ($\max\{s_{im}\} = 1.5$ CD), and when the cell moves too far from its location of contact it is no longer considered to be attached to the membrane. At this point the contact location is removed, and the cell experiences no attachment force unless it comes into contact with the membrane again.

Desquamation

The top of the tissue, $z = H$, is where desquamation occurs and cells are lost to the environment. In our base model, the removal method is *sloughing*: cells are removed from simulation after they reach a specified height, $z = H$ CD. This method is used for Chapter 5. We believe this is a robust method to use in this research as for the study contained in Chapter 5 we are only interested in the dynamics of the basal layer. As the dominant movement in the tissue is vertically upwards, this simplified removal method should have little impact on the dynamics in the basal layer. In Chapters 6 to 8 we investigate cell removal and use an alternative method to modelling desquamation. This method will be described in Chapter 6.

4.1.3 Initial conditions

In order to begin from a homeostatic system, we run an initial fill period to produce a complete tissue. We start with 100 proliferating cells on a 10 CD by 10 CD basal plane. The details on proliferation are given below. The system will tend to pack tighter than a 1 CD square for each cell by the end of this fill period, and so the basal layer consists of both proliferative and differentiated cells.

The fill period uses the same setup as the model described above, with one exception: an extra boundary condition is imposed on stem cells to ensure they remain on the membrane. This boundary condition only restricts stem cell heights, therefore still allowing horizontal movement. This restriction is necessary due to the proliferative cell loss issues we will discuss in Section 4.4. Once the tissue is filled we remove the height restriction and run the model as described.

4.2 Cell proliferation

The other component to our epidermal tissue model is cell proliferation. As explained in Section 2.2, cell proliferation in the epidermis occurs in the basal layer. We model this proliferation stochastically, using a set of rules. Cells are created either proliferative or non-proliferative. If they are proliferative, after a period of time determined at their birth they proliferate and produce two daughter cells. Modelling of the proliferation process is described below in Section 4.2.1. The proliferative type of the daughter cells is determined by the cell lineage chosen, as will be explained in detail in Section 4.2.2.

The last element of cell proliferation is control of *division orientation*: the positions of the two daughter cells relative to each other. In this chapter we provide a simple way to orient division direction. Chapter 5 will provide more detail on the requirement for the regulation of division orientation and a novel, more robust, method of modelling the regulation.

4.2.1 Modelling the cell cycle

The cell cycle is the cycle a proliferative cell undergoes before dividing. As described in detail in Section 2.2, the cycle has 4 phases, in order: G1; S; G2; and M. The time lengths of importance for the model are the M phase length and total cycle time, as these are the time points at which division events occur.

In the model, the phase lengths for a proliferative cell are stochastic and determined at birth. We set the phase lengths for S, G2, and M to T_S = 5 hours, T_{G2} = 4 hours, and T_M = 1 hour respectively. The remaining phase is the G1 phase, to which we add stochasticity: $T_{G1} \sim U(3, 7)$. This makes the total cell cycle length $T_C \sim U(13, 17)$, unless mentioned otherwise. This gives an average cell cycle time of $\mathbb{E}(T_C)$ = 15 hours, as used in Li et al. [72]. Though the average cell cycle time is not known in the epidermis, it is likely much longer than 15 hours in both mice

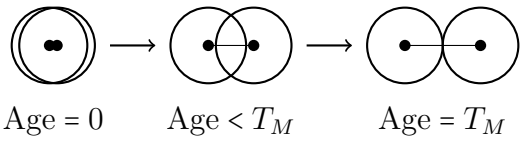

Figure 4.3: The increasing spring length between two daughter cells during the M phase of the cell cycle.

and humans, as discussed in Section 2.2. However, the actual cell cycle time is not critical to the system dynamics we are interested in as it just corresponds to a time scale for system turnover. By reducing the cycle time to 15 hours in the model we can achieve lower computational times for high numbers of divisions.

In order to model the splitting of the parent into two daughter cells, we shift the cell cycle by a phase. In the model the parent cell splits into daughter cells at the transition between the G2 and M phases. Consequently, the first T_M hours after division are allocated to the M phase of the division cycle. At the point of division, the spring length between the two daughter cells is much smaller than the ordinary spring length between two non-dividing cells—the daughters are born almost completely overlapping. Over the M phase (T_M), the spring length grows linearly until it reaches the normal spring length of r_{ij} = 1 CD, as shown in the diagram in Figure 4.3. The two cells still experience interaction forces due to each other during this period, however the changing spring length changes the zero force separation distance between the two cells, as defined by Equation (4.3). This process represents the growth and division process of the parent cell.

Cell proliferation is a complex process, including a multitude of subcellular machinery, and this model will not precisely reflect the cell growth and division dynamics. In particular, we do not incorporate the cell growth during the other cycle phases which was described in Section 2.2.2. However it is a good approximation when using constant radius cells with spherical cell shapes.

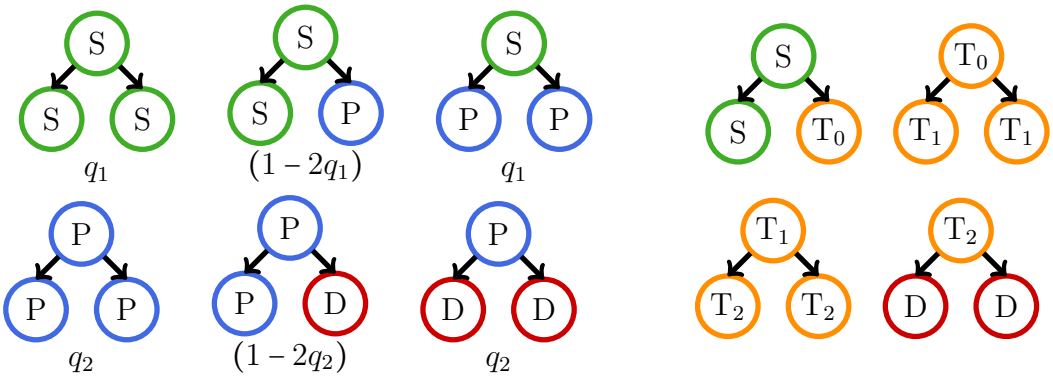

(a) Population Asymmetry (with stem cells) (b) Asymmetric Division

Figure 4.4: The division scenarios, S: stem cell, T_g: Transit amplifying cell at generation g, P: progenitor cell, D: differentiated cell. Population Asymmetry can include the stem cells (all six divisions shown) or not include the stem cells (only the second line).

4.2.2 Cell lineage

Cell lineage refers to the differentiation hierarchy—the sequence and timings of conversions between stem, progenitor, transit, and differentiated cells. As explained in Section 2.2, and illustrated in Figure 2.6a, there remains considerable uncertainty about the details of cell lineage in the epidermis.

In our model, we assign the cell type at birth to be stem or progenitor, transit, or differentiated. We initially investigated all three cell lineages used in Li et al. [72]: *asymmetric*, *population asymmetry*, and *population asymmetry with stem cells*. These are shown in the diagram in Figure 4.4.

Population asymmetry is not robust without regulating mechanisms

Proliferative cells in the two population asymmetry lineages, shown in Figure 4.4a, have 3 possible division outcomes: both daughter cells match the parent cell type, both daughter cells move down the differentiation path (either stem to progenitor, or

progenitor to differentiated), or one daughter cell matches the parent and the other moves down the differentiation path. The difference between the two population asymmetry lineages is that one includes stem cells, the top row in Figure 4.4a, and the other does not. These division scenarios require probabilities to be assigned for each division outcome, designated by q_1 and q_2 in Figure 4.4a.

When using the population asymmetry lineages there is no way to maintain a steady proliferative cell population size without some extra regulatory mechanism. We can investigate this by approximating the cell lineage as a branching process. If we start with a single proliferative cell, the probability of extinction (d_n) of the cell's colony at generation n is:

$$d_n = p_0 + p_1 d_{n-1} + p_2 d_{n-2}, \tag{4.11}$$

where p_0, p_1, and p_2 are the probabilities that the proliferative cell produces 0, 1, or 2 proliferative daughters respectively (produces 0, 1, or 3 stem cell daughters in a stem-progenitor division). Relating this back to the diagram in Figure 4.4a, $p_0 = p_2 = q_1$ and $p_1 = 1 - 2q_1$ for stem cell divisions or $p_0 = p_2 = q_2$ and $p_1 = 1 - 2q_2$ for progenitor cell divisions. In Li et al. [72], these proportions were $q_1 = 0.08$ and $q_2 = 0.1$.

The results from Equation (4.11) can be seen in Figure 4.5. As can be seen in Figure 4.5b no feasible $q > 0$ can maintain a sufficient population for the time frames we are interested in (a minimum of 200 generations). We define a sufficient population to be at least 90 out of 100 cells remain proliferative. Note, the $q_1, q_2 = 0$ line is the equivalent of an asymmetric division cell lineage, but with progenitor cells instead of transit cells.

We can also add a proliferative bias to try and balance out the population loss. Considering the hypothesis with only progenitor cells (second line only in

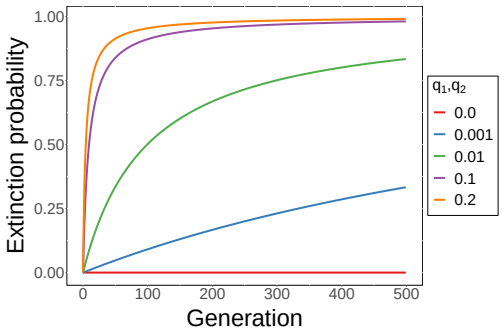

(a) The likelihood of extinction of a colony stemming from one proliferative cell that can divide to produce zero, one, or two proliferative daughters.

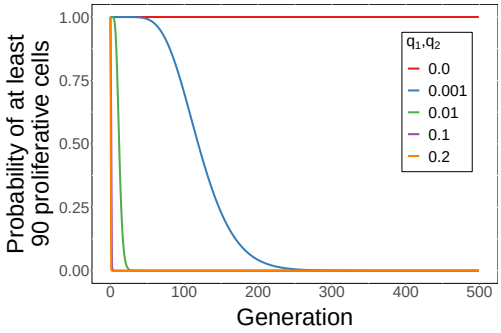

(b) The likelihood of maintaining at least 90 proliferative cell colonies out of 100 initial proliferative cell colonies.

Figure 4.5: Likelihood of extinction and maintenance for population asymmetry lineages. Graphs are based on the population asymmetry without stem cells cell lineage, where a progenitor cells produces zero, one, or two proliferative daughters at each division.

Figure 4.4a), the probabilities become:

$$p_0 = q - y, \tag{4.12}$$

$$p_1 = 1 - 2q, \tag{4.13}$$

$$p_2 = q + y. \tag{4.14}$$

However, using the same analysis described by Equation (4.11), we found that, even for small values of y, we get excessive population growth (results not shown). Consequently, this does not provide a robust solution.

From these results, we have determined that using the population asymmetric hypothesis it is not possible to maintain a realistic proliferative population using only a stochastic model. In order to use this cell lineage it would be necessary to incorporate some form of regulation to guide the daughter types chosen in a cell division.

Simplified asymmetric division cell lineage

Asymmetric division is the alternative, more robust lineage and consequently this is what we base our cell lineage model on. As can be seen in Figure 4.4b, in this lineage a stem cell division produces a transit cell and a stem cell. The transit cell undergoes two further divisions, producing two transit cells, before dividing to produce two differentiated cells.

Though we base our cell lineage on the asymmetric division model, it is possible to approximate this model with only a single proliferative cell type. In the asymmetric division lineage each stem cell division leads to the production of 8 differentiated cells after 3 iterations of transit cells. Consequently, given a stem cell cycle length of T_{SC}, this gives a rate of production of differentiated cells of 8 cells every T_{SC} hours. The same differentiated cell production rate is achieved by 8 proliferative cells dividing to produce one proliferative and one differentiated daughter, as shown in Figure 4.6, every T_{SC} hours. This simplified system is what we use for

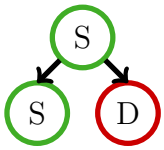

Figure 4.6: The simplified cell lineage we use in the model.

our model. We call the proliferative cells in this model *stem cells* as we assume they are immortal and they approximate the asymmetric division hypothesis, however they have a much faster proliferation rate than would be expected of stem cells.

4.2.3 Control of division direction

In the base model (the model defined in this Chapter), we enforce the orientation of the two daughter cells at the point of division. The differentiated daughter is placed vertically above the stem cell daughter when the new cell is created. However, this division direction is not enforced as the cells spring length increases over the M phase. Further control is used in later models, and this will be described in Chapter 5.

4.3 Chaste

We build the described model within the Chaste (Cancer, Heart and Soft Tissue Environment) framework [84, 96]. Chaste is a C++ library for modelling biological tissues, with the computational capabilities required to implement a three dimensional multicellular model. The Chaste core code can be accessed at `https://chaste.cs.ox.ac.uk/trac/wiki`. The core code includes the numerical solver for solving the equations of motion, methods for including stochasticity, representative forces, and models for cell division methods [84, 96]. In order to build our model, we specify each new element detailed above as an extension to the core Chaste classes, such as force classes and cell lineage classes for the system described

above.

4.3.1 Numerics

Two key considerations when deciding on a numerical method are the required efficiency and the complexity of the system. Our simulations are in three dimensions and generally contain 1,000–2,000 cells. Consequently, computational efficiency is critical. An extra complexity in our system is the frequent addition (via proliferation) and removal (via desquamation) of cells in the system. This is effectively adding frequent perturbations to the system.

Given the high efficiency that is required and the complexity in the system, we use an explicit, constant time step numerical method. The simplest explicit, constant time step numerical method is the forward Euler method and this is the method we use in our model. The equation for Euler's is:

$$\mathbf{c}_{n+1} = \mathbf{c}_n + \Delta t \frac{\mathrm{d}\mathbf{c}_n}{\mathrm{d}t_n}, \tag{4.15}$$

where $\mathbf{c}_n$ is the location of the cell at time step t_n, Δt is the length of the time step, and $\frac{\mathrm{d}\mathbf{c}_n}{\mathrm{d}t_n}$ is determined using the equation of motion described in Equation (4.1). These numerics are part of the core Chaste code base. We use a time step of Δt = 30 s, as in Van Leeuwen et al. [120]. Given the force expected (10 μN) and viscous drag coefficient (η = 3.6 g.s^{-1}.CD^{-1}) used for this study, Equation (4.1) and Equation (4.15) give a maximum movement in 30 s of 0.008 CD, and consequently this is found to be a stable time step.

4.3.2 Extending the core code

Using the Chaste core code we could produce a simplified version of the model described above. This simplified setup is shown in Figure 4.7. In order to produce the model described in this chapter (Figure 4.1), it was necessary to make several extensions to the code. In order to build some of these extensions, it was necessary

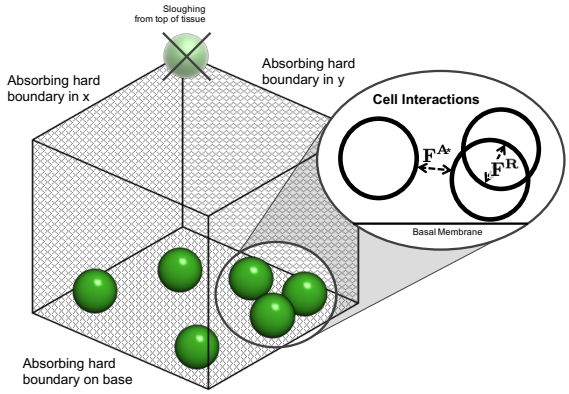

Figure 4.7: The tissue model using only core Chaste code, in comparison to the new model as shown in Figure 4.1. Here the adhesive function, $\mathbf{F}^{\mathbf{A}*}$, is of a different functional form.

to also modify the core code. The modified core code can be found at `https://github.com/clairemiller/Chaste`, and additions that did not modify the core code can be found at `https://github.com/clairemiller/ThesisCode`.

The addition of membrane adhesion, the adhesive force function, and the division direction (not shown in diagram) built on existing mechanics in the Chaste framework. However, the addition of periodic boundary conditions required more complicated extensions. This is because periodic boundary conditions require cells near the edge of the domain to detect neighbours at the opposite side of the domain. A cell's neighbours are the set of cells that could interact with, and effect a force on, the cell. In order to decrease the computational time required to determine a cells neighbours, Chaste divides the domain into a grid of the same dimension as the simulation. Grid size is the maximum radius of interaction between two cells, specified by the user (we use 2 CD). Neighbours of each cell are determined by iterating over all cells within that cell's box and its neighbouring boxes. In order to apply periodic boundary conditions to a box on the edge of the domain, it needs to search boxes on the opposite side of the domain, as shown in Figure 4.8. It must also move cells into these boxes if any cells are forced outside the domain. The code

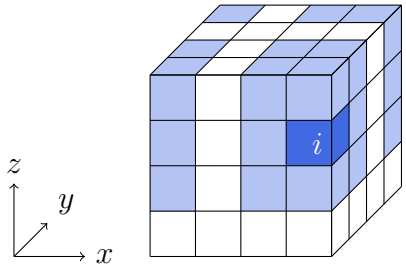

Figure 4.8: An example of the grid cells required (light blue) to determine the neighbours of the cells in box i (blue) if the domain is periodic in x and y.

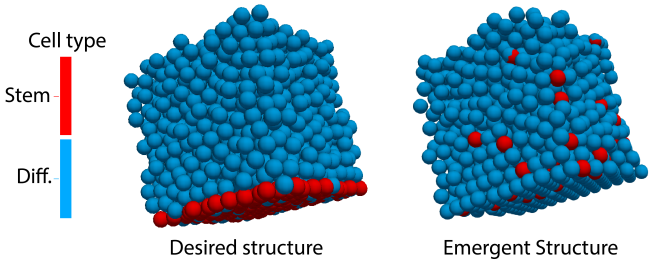

Figure 4.9: Simulation output with z as the vertical direction. Left: desired output structure with stem cells (red) at base, and suprabasal cells all differentiated (blue). Right: The resulting simulation structure using the model described above.

allows for periodicity in any number of dimensions, and was also developed to be run in parallel, in which case each box is assigned to a different processor.

4.4 Simulation output

An example of simulation output is shown in Figure 4.9. A video of a simulation using this base model can also be found at `https://youtu.be/4a985GcgOUw`. As can be seen in the figure, the simulated tissue after 500 days does not maintain a stem cell niche in the basal layer. This issue is investigated and addressed in Chapter 5.

4.4.1 Resulting tissue dynamics

We are interested in understanding the dynamics of the tissue. The dynamics of interest are cell counts, cell velocities, and cell deaths (via sloughing in this model). Plots of the simulation output are shown in Figure 4.10 for one simulation. The velocities are instantaneous velocities, calculated from the forces experienced by the cell at the output time point. The plots show the average velocity of all cells in the tissue. The stem cell velocities are not included in these results as their z velocities tend to be higher than the rest of the cells due to the their high adhesion to the membrane.

In the plots we can again see that the system is not maintaining its initial structure. The stem cell population has all left the basal layer by the end of the 500 days, and as a result the death rate (Figure 4.10b) and vertical cell velocity (Figure 4.10c) drop significantly in the first two output time steps. The system does appear to reach a new homeostatic state for the cell velocity and cell deaths, however at low values and with very few remaining stem cells in the basal layer.

Figure 4.10a shows the structure forming layers in the lower regions of the tissue after 500 days. This is due to the loss of stem cells in the basal layer. When stem cells remain in the basal layer, the constant influx of cells from the cell divisions causes constant movement in the suprabasal tissue, and hence there is not enough time for the system to stabilise into an ordered structure. However, if the stem cells instead move into the suprabasal regions, the cells in the lower regions of the tissue with no proliferative cells below them have the time to settle into clear layers.

4.5 Summary

This chapter has provided an overview of the base model we use for this study. Additional components are added for the different research questions studied, and these will be described in their relevant chapters. In summary, we use an overlap-

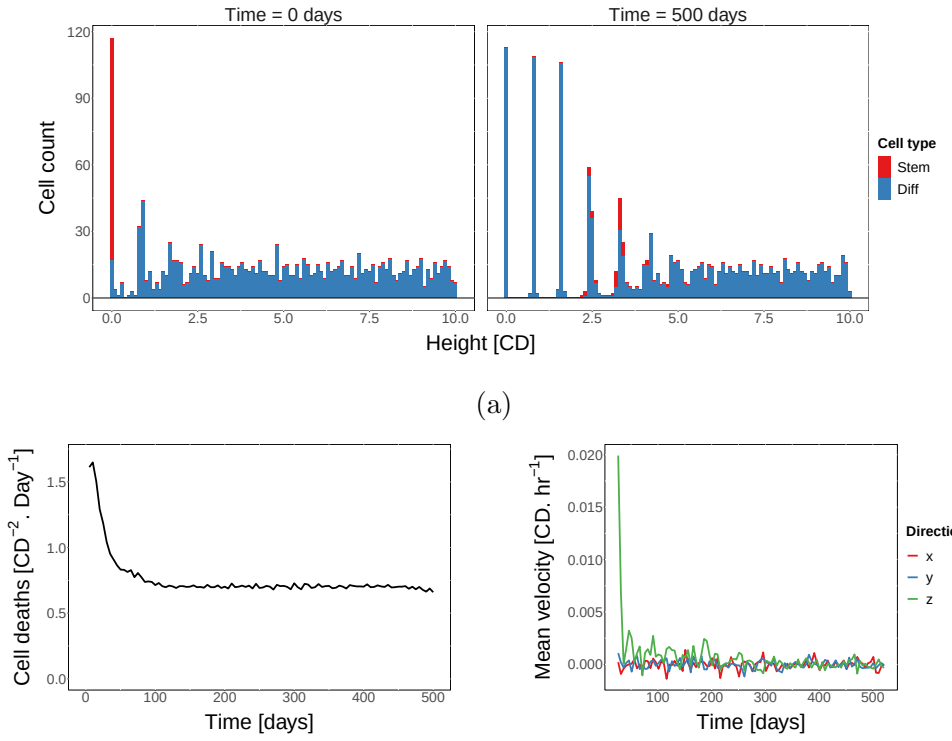

Figure 4.10: Tissue dynamics of one simulation. (a) A stacked histogram of cell counts at the start (after the fill) and end of the simulation. (b) The cell death rate over time. (c) The mean (over all the cells) velocity in each direction over time.

ping spheres model to simulate the inter-follicular epidermis. Cells move due to interactions with other cells, and the basal membrane. The dominant cell movement is vertically upwards due to the proliferation occurring in the basal layer. This proliferation is modelled using a stochastic rule based method. In Chapter 5 we will use this model to investigate the loss of the proliferative population seen above. We then add a mechanistic model for desquamation in Chapter 6 to investigate the maintenance of tissue thickness. This mechanistic desquamation model is replaced by a subcellular desquamation model in Chapter 8.

5 | Maintenance of a stem cell niche

This chapter investigates the erroneous loss of stem cells from the niche (basal layer) that occurs when using current modelling methods. The material in this chapter reproduces content from a paper in preparation which is currently available on arXiv (Miller, Crampin, and Osborne [81]). Using the model described in Chapter 4, we are unable to maintain populations of stem cells in the basal layer. In this chapter we introduce a novel modelling mechanism to ensure maintenance of desired stem cell populations—a rotational force which regulates division orientation during the M phase of the cell cycle. We demonstrate that this new methodology is able to maintain higher, more realistic, stem cell populations in overlapping spheres models.

5.1 Introduction

The basal layer is where all proliferation occurs in the epidermis by means of one or two proliferative cell types [6, 19, 59, 74, 105]. Continuous proliferation in the basal layer ensures a steady replacement of the cells lost at the top of the tissue.

The density of proliferative cells in the basal layer of the IFE is not known. A study in mice by Ipponjima, Hibi, and Nemoto [52] found that the density of basal cells was correlated to epidermal thickness. The basal cell densities varied from

128 cells/10^4 μm for 17 μm dorsum IFE to 218 cells/10^4 μm for 56 μm scale IFE (values estimated from graph). Note, the density unit for this data is cells/μm, as opposed to the unit of cells/μm^2 used in our results. This is the unit used in the paper and so we assume the data was recorded along a line across the basal layer. Importantly, this is also the density of all basal cells rather than actively proliferating cells, and differentiated cells have been previously detected in this layer [58].

Recent work, previously discussed in Section 3.3, has used multicellular models to investigate the dynamics of the IFE [72, 118]. These models were used to investigate the morphology of the IFE [118] and clonal dynamics, that is sizes of the cell populations stemming from a single proliferative cell [72]. Both of these tissue properties are influenced by the proliferative cell density. The morphology of proliferative and non-proliferative regions changes with the loss of stem cells, as could the stratification of the layers as the vertical velocities of cells are affected by reduced basal divisions. If the modelling techniques we use are influencing the stem cell population they would also influence the clonal dynamics, likely decreasing the number of clonal populations observed in the system. This also applies to clonal dynamics studies using these techniques in other epithelial tissues, such as the colonic crypt (intestinal glands in the colon) [85].

Previous models have employed different strategies in order to maintain stem cell populations. Sütterlin et al. [118] fix the stem cells in place on the membrane, thereby ensuring the maintenance of this niche. However, such a pinning has not been observed *in vivo*. Li et al. [72] and Kobayashi et al. [65] tightly bind the stem cells to the membrane by increasing adhesion for stem type cells. While mitigating the issue, this method restricts stem cell movement, which may not be biologically realistic and does not always guarantee maintenance of the population.

Using the multicellular model described in Chapter 4 with membrane adhesion functions and parameters based on those used in Li et al. [72], we found the system could not maintain high populations of stem cells. The desired system structure and

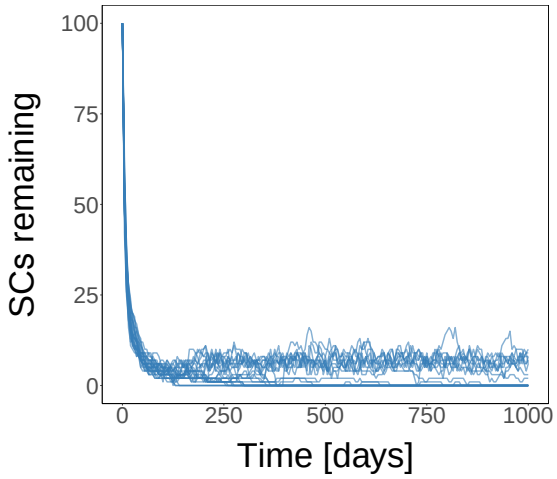

Figure 5.1: The population size of stem cells remaining in the basal layer over time. 25 realisations of the model are shown as there is stochasticity in the system.

a representative example of a simulation result were shown in Figure 4.9. It can be seen that almost all of the stem cells (red) have been lost from the basal layer and are moving upwards through the tissue. Figure 5.1 shows the proportion of original stem cells in the basal layer over time for 25 realisations of the model. The graphs shows that, in all realisations, stem cell populations in the niche reduced to less than 20% of their original population within 15 days. The mean stem cell count after 250 days is 2.8 cells. Assuming a cell diameter of 10 μm, this is a density of 2.8 proliferative cells/10^4 μm^2.

The IFE models discussed in this thesis so far assign a proliferative type to a cell at birth. An alternative approach is to associate proliferative ability to the spatial location of a cell. This concept is commonly used when modelling the colonic crypt [14, 85]. In the crypt, cells proliferate at the base and become terminally differentiated towards the top of the tissue. This is thought to be due to a gradient of the signalling factor Wnt through the depth of the crypt. Using this approach the niche will always be maintained. However, as mentioned above, it has been

hypothesised that two proliferative cell types exist in the IFE [74, 105], as well as potentially differentiated cells [58], suggesting more complicated intra- and inter-cellular signalling is required to maintain the niche.

Here we consider an alternative mechanism to maintain the niche that does not use cell signalling or restrict stem cell movement. Our results indicate that the current model of cell division enables easy entry of newly differentiated cells into the niche and therefore causes a loss of stem cells from the niche. Our alternative mechanism, motivated by these results and based on the experimentally observed regulation of division orientation, directly opposes the entry of differentiated cells into the basal layer during division by regulating division direction throughout the division process.

The regulation of division direction is reflective of the regulation of the mitotic spindle which forms in the final phase of the proliferative cell cycle. During the M phase, the mitotic spindle is formed and the cell elongates. The mitotic spindle consists of two poles at either end of the parent cell and determines the division direction of the cell. At the end of the M phase, the cell splits at the midpoint between the two poles of the spindle. In some tissues, misalignment of the spindle can lead to loss of tissue morphology [125] and has even been connected to epithelial tumour growth [95].

The orientation of the mitotic spindle during epidermal development stages has been well studied in mice—divisions parallel to the membrane dominate early development, then a switch to perpendicular occurs later in the development process to aid stratification of the tissue [8, 69, 70, 100, 125]. However less is known about the process in the adult epidermis. Ipponjima, Hibi, and Nemoto [52] imaged division directions in adult mice epidermis and observed a tendency towards parallel or oblique division directions depending on the body region considered. Interestingly, they also found that the number of oblique divisions (between 70 and 90 degrees) and the basal cell density was correlated to epidermal thickness. Consequently, there

is a potential association between oblique divisions and basal cell density. Results from Lechler and Fuchs [70] found the majority of divisions were perpendicular to the membrane to promote stratification in adult mice. In contrast, Clayton et al. [19] determined that only 3% of divisions were perpendicular to the membrane in mouse tail. Though the exact orientation of division in human epidermis is unclear, these results imply some type of regulatory mechanism for spindle orientation in the homeostatic tissue.

The regulation of division direction is useful to include in a mathematical model. Gord et al. [38] and Du et al. [25] found a switch from symmetric division parallel to the membrane to asymmetric division perpendicular to the membrane, combined with polar adhesion, generated correct stratification in their *in silico* model of epidermal development. Here, polar adhesion means basal and suprabasal regions of cells only form bonds with the basal and suprabasal regions of other cells respectively. We propose an alternative approach of a selected division direction at division and a rotational force to maintain this direction during the M phase of the cell cycle.

In this chapter we investigate how the modelling approach influences the potential loss of stem cells from the basal layer. We then investigate the strategy of the rotational force as a maintenance mechanism for the layer. Results show that the inclusion of the rotational force is more robust at maintaining a desired stem cell population size.

5.2 Model extensions

The model used in this chapter uses, and extends, the model described in Chapter 4. We add an additional force to regulate division orientation. Our implementation of this force is described below. We also describe the comparison metric we use to compare results using different parameters, and the model with and without the rotational force. This metric estimates the steady state population for each setup.

5.2.1 Control of division direction

Building on the model of cell growth and division described in Section 4.2.1, we add control of the relative orientation of the two daughter cells during the M phase of the division cycle. We do this by applying an additional force to dividing cells during the M phase of the division cycle. This phase has a length of $T_M = 1$ hour, as described in Section 4.2.1. The force is in addition to the enforcement of a vertical orientation at the point of division as described in Section 4.2.1. Given we use an asymmetric division lineage, the stem cell should remain attached to the membrane, and the differentiated cell should enter the suprabasal layers. Consequently, in order to control division direction, we apply a *division force* to the differentiated cell to help maintain an upward, vertical division direction. The stem cell daughter is assumed to remain in place and not experience any division force from the differentiated daughter, only the usual repulsion and attraction forces.

As the actual mechanism for the division orientation is highly complex and not completely understood, in this chapter we implement a simple model to emulate the effects of the mechanism at a cellular, rather than a subcellular, level. We base our model on a torsional spring force that is independent of spring length, similar to how we model other cell-cell forces. Figure 5.2 illustrates the concept of the force—rotating the differentiated daughter cells towards the upwards vertical position. The force equation is given in Equation (5.1) where k_ϕ is the torsional spring constant, ϕ is the angle between the division vector and vertical, and $\hat{\mathbf{n}}$ is the unit normal to the division vector:

$$\mathbf{F}_j^{\text{Rot}} = -k_\phi \phi \hat{\mathbf{n}} \, . \tag{5.1}$$

It would be feasible to use an alternative function of ϕ to the linear function shown here, however for any reasonable increasing function of ϕ qualitatively similar results might be expected.

The force is applied in a direction normal to the separation vector of the two

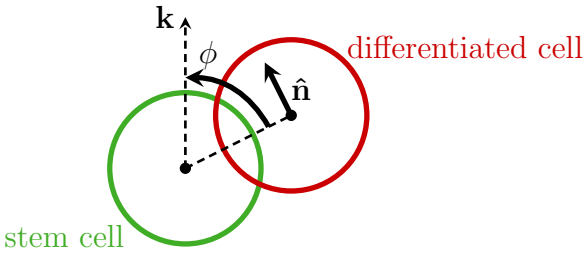

Figure 5.2: The concept of the rotational division force. $\mathbf{k}$ is the vertical unit vector and the desired division direction. The force is applied in the direction of the vector $\hat{\mathbf{n}}$.

cells and towards the desired vertical direction in the plane of the separation vector and the desired vertical direction at each time step. This is defined mathematically as:

$$\hat{\mathbf{n}} = \frac{\mathbf{s}_{ij} \times (\mathbf{k} \times \mathbf{s}_{ij})}{\|\mathbf{s}_{ij} \times (\mathbf{k} \times \mathbf{s}_{ij})\|}, \tag{5.2}$$

where $\mathbf{s}_{ij}$ is the unit vector between daughter cells i and j, and $\mathbf{k}$ is the vertical unit vector, representing the desired division direction. The angle ϕ is consequently bounded by $[0, \pi]$, with π being the highly unlikely case that the differentiated cell is pushed vertically below the stem cell.

5.2.2 Steady state population estimation

In order to compare the effectiveness of the different parameter combinations at maintaining the niche, it is necessary to determine a comparison metric. Motivated by the decay curves observed (see Figure 5.1) we assume the stem cell loss from the niche approximately follows an exponential form: cells detach from the basal membrane at some rate λ, but with a steady state population β of the stem cells remaining attached to the membrane. This is described by the following function:

$$p(t) = \omega e^{-\lambda t} + \beta \,, \tag{5.3}$$

where $p(t)$ is the population of stem cells attached to the membrane at time t, and ω is the lost population. Physically, β represents the number of stem cells that remain in the basal layer long term, and is consequently an estimate for the maximum density of stem cells the system can maintain in the niche. Given we simulate a horizontal domain of size 10^4 μm^2, the expected maintained proliferative cell density in the basal layer is given by β cells/10^4 μm^2. The fit of this model to the simulation data depends on the parameter values and hence β is a useful comparison metric for the different parameter combinations.

At very high steady state populations, when the mean stem cell loss was less than 6%, the regression algorithm could not find an appropriate fit to the data. This is due to the assumption of an initial transient, given by $\omega e^{-\lambda t}$ in Equation 5.3. When the starting population is very close to the steady state population, the algorithm fails to find a transient to fit to. Investigating these results by calculating the fit for β with a designated λ shows little variation in the calculated β, implying the data is relatively insensitive to λ over the time periods used. Consequently, in the cases where the mean loss was less than 6%, we instead set β as the mean stem cell count of the 25 realisations at the last time point.

5.3 Results

We include stochasticity in both the cell cycle time and the membrane boundary, as detailed in Section 4.2.1 and Section 4.1.2. Consequently, for each parameter set, we run the setup with 25 different seeds. Results show both every individual realisations and the mean, or just the mean, unless mentioned otherwise.

5.3.1 Loss of the niche affects system dynamics of the tissue

Using the model without the rotational force, which we will refer to as the base model, we see in Figure 5.1 that the system is unable to maintain a proliferative cell

density in the basal layer greater than 16 cells/10^4 μm^2. A video of a simulation can be found at `https://youtu.be/4a985GcgOUw`. Figure 5.1 shows the loss of the stem cell population in the basal layer over 1,000 days. The number of stem cells in the basal layer is determined by the number of stem cells which are experiencing the attachment force with the membrane. Consequently it is possible for a cell to detach and then re-attach later, which is why the lines do not always monotonically decrease in Figure 5.1.

In addition to disruptions to tissue structure, stem cell detachment affects system dynamics such as cell deaths at the top of the tissue and cell velocities. These results were shown for one simulation in Figures 4.10b and 4.10c and Figure 5.3 shows results for all 25 realisations and their mean. Figure 5.3 shows the base model results compared to a model in which the stem cells are vertically restrained to remain on the basal membrane, which represents the expected homeostatic system. Velocities are instantaneous velocities calculated from the forces experienced at the output time step, and the results for each simulation show the mean of all cells in the tissue. As in Section 4.4, stem cells are excluded from these results as they have much higher velocities due to their high adhesion to the basal membrane, and hence obscure the effects on the cell velocities in the rest of the tissue. This exclusion is used for all velocity plots in this thesis.

Two features of the plots in Figure 5.3 are relevant to all system dynamics results presented in this chapter. The first is the initial overshoot seen in the death rates and velocities. This is due to the fact that the tissue at the end of the fill period is not in exact equilibrium, and so there is a short initial settling phase when the stem cell restriction is released. The second is the noise seen in the velocity results. This is to be expected as proliferation events cause a large amount of movement in the system, and therefore the velocity will depend on the number of proliferation events in the time steps leading up to the output time step.

Figure 5.3 shows that, as time increases, and stem cells are lost, the vertical

Parameter	Description	Value range
$\frac{\alpha^*}{500}$	Basal membrane adhesion, as a multiple of the base model membrane adhesion	0–3
l_d	Starting spring length at division [CD]	10^{-3}–10^{-1}

Table 5.1: Sweep parameters.

velocity and cell death rate decreases. This would be expected as the decrease in stem cells causes a decrease in divisions. Consequently, less upwards force is exerted on cells, decreasing velocity and slowing the rate at which cells reach the top boundary. Slower upward velocities and lower death rates can dramatically change simulation dynamics, such as cell turnover times, and give rise to unrealistic results.

5.3.2 Only a very high level of membrane adhesion can maintain a niche in the base model

In order to fully investigate the problem we try different parameter combinations for the division and membrane adhesion parameters in the model. The different parameter ranges investigated are shown in Table 5.1. Doubling the length of the M phase, from 1 to 2 hours, was also tried, however the difference in results was minimal and is not included here for brevity.

The values of the estimated steady state population, β, for the different parameter combinations are shown in Figure 5.4b alongside examples of fits in Figure 5.4a. The plot in Figure 5.4b shows that increasing the adhesion to the basal membrane significantly increases the remaining stem cell population. It can also be seen that the remaining stem cell population decreases as the spring length at division decreases. At the lowest spring length, which provides the more realistic division model, it is necessary to increase the adhesion to three times the value of Li et al.

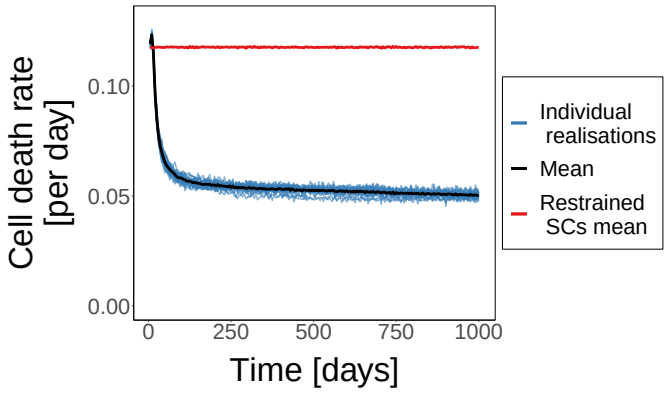

(a) Deaths

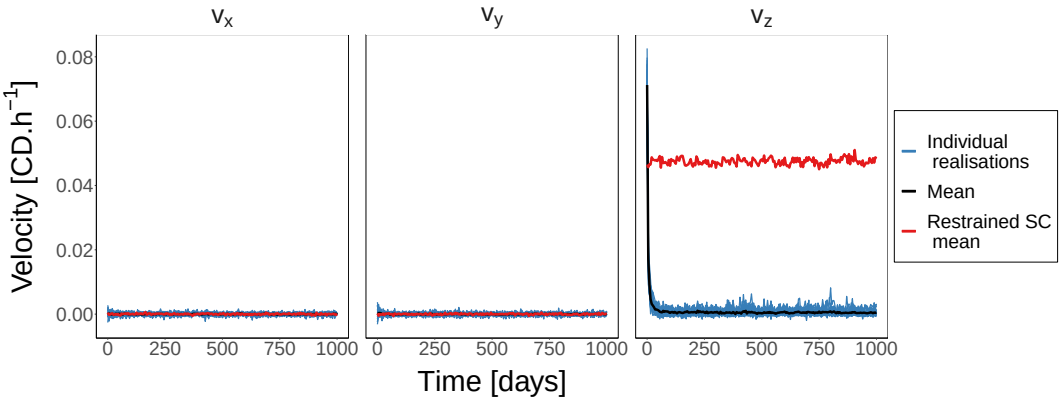

(b) Velocity

Figure 5.3: The effect of the loss of the stem cell niche on system dynamics for all 25 realisations: (a) cell deaths from the top of the tissue, as a proportion of total cell count, and (b) the cell velocities, in units of cell diameters (CD) per hour, in each direction. Blue lines show the individual simulation instances, and the black line is the average. The red line shows the comparative results for a simulation with vertically restrained stem cells (SC).

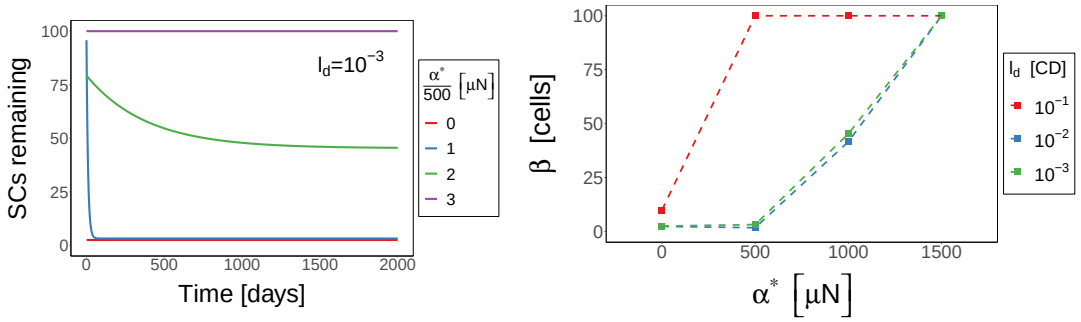

(a) Examples of fitted curves

(b) Results for base system

Figure 5.4: (a) Examples of the loss curves for the different levels of adhesion to the basal membrane at the lowest division spring length considered; l_d = 10^{-3} CD. (b) The value of β, the remaining stem cell population in the niche, for each parameter combination. The unit of l_d is cell diameters (CD).

[72] to maintain the desired population. Consequently, we see that we are unable to maintain high proliferative cell densities, particularly at low division spring lengths, without high levels of adhesion to the membrane.

5.3.3 Stem cell loss is due to neighbouring cell interactions during division

We wish to understand the underlying mechanism for stem cell loss from the basal layer. We propose that it is related to the low displacement required to rotate the daughter cell into the basal layer at the smaller spring lengths during the M phase of the division model. This idea is reinforced by the lower remaining stem cell population (β) seen as the division spring length (l_d) is decreased in Figure 5.4b. Once the daughter is in the basal layer, the layer becomes overcrowded and a cell must be pushed out. If the suprabasal area above a stem cell is at a lower density than that above the newly basal differentiated cell, the stem cell will be pushed out. This is because, in the model, the attractive forces between the stem cell and the

membrane are lower than the repulsive forces between the suprabasal cells and the differentiated daughter. This is shown diagrammatically in Figure 5.5a.

In order to investigate the validity of this proposed mechanism we can determine the number of differentiated daughter cells in the basal layer at the end of their M phase. The end of the M phase is the point in time at which the resting spring length between the two daughters reaches one cell diameter. This is also when the two daughter cells become two separate cells and are no longer considered a dividing pair. Figure 5.5b shows a histogram of the average heights over the first ten days of simulated time using the base model for the smallest (10^{-3}) and largest (10^{-1}) values of l_d considered, with $\alpha^* = 500$ μN. If the differentiated cells are being pushed into the basal layer as proposed we would expect to see large numbers of cells at, or close to, zero. As can be seen on the right in Figure 5.5b, there are more differentiated daughter cells in the basal layer at the smaller division spring length, $l_d = 10^{-3}$. These results support the idea that the smaller spring lengths enable the rotation of differentiated daughter cells into the basal layer, hence out competing the stem cells and pushing them out.

It is interesting to note that a mode in each of the histograms is seen around 0.7 CD. We would expect the cell packing to form a triangular pyramid style of packing, which would place the second layer of cells at roughly 0.8 CD, slightly higher than seen in this plot. The lower height is likely due to the compression both in the system overall, and particularly experienced as the daughter cells press into the surrounding cells during the division.

5.3.4 A rotational force improves maintenance of the niche

Motivated by the observed regulation of division orientation, we impose a rotational force on the differentiated daughter cell during the M phase, which directly opposes the proposed mechanism of cell loss described above. In Figure 5.6a we plot the estimated steady state population, β, for simulations using the rotational force. We

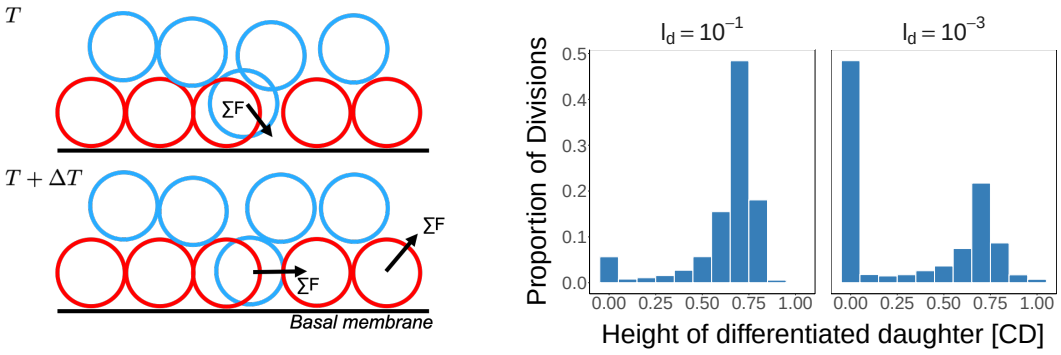

(a) Cell loss diagram

(b) Daughter height

Figure 5.5: (a) A histogram of the height of the differentiated cell's centre at the end of M phase for the largest (left) and smallest (right) spring lengths at division. The unit of l_d and the height is cell diameters (CD). Results are shown for membrane adhesion $\alpha^* = 500$ μN. (b) The proposed method by which differentiated cells enter the basal layer and push stem cells out. stem cells are shown in red, differentiated in blue. The top image shows the system at time T, immediately after the division has occurred. The lower image shows the system at time $T + \Delta T$, where ΔT is less than the M phase length and so the cells are still within the M phase.

present results for basal adhesion (α^*) levels between zero and the adhesion level used by Li et al. [72] (α^* = 500 μN). A video of a simulation using a rotational force of k_ϕ = 100 μN (l_d = 10^{-3} CD and α^* = 500 μN) can be found at `https://youtu.be/SSYWjvNZSsY`.

Figure 5.6a shows that including the rotational force increases the population of stem cells that remain attached to the membrane (β) for all spring lengths (l_d). With the base level of adhesion to the membrane (α^* = 500 μN), any of the rotational spring constants investigated (k_ϕ = 10, 50, 100 μN) maintain the whole stem cell population. With no adhesion and a torsional spring constant of k_ϕ = 50 μN or higher, the remaining population is maintained above 70 cells/10^2 μm^2.

It can be seen in Figure 5.6b, compared to Figure 5.5b, that the rotational force has significantly reduced the presence of differentiated daughters in the basal layer, directly opposing our proposed mechanism for why the stem cell loss occurs. It is also important to note that the mode of the histogram remains around z = 0.7, we have only removed the second peak at z = 0. Consequently, the addition of the rotational force has enabled better maintenance of the basal layer over the time periods of interest, even at very small division spring lengths where the division model is most representative of cell division and the model without the rotational force fails.

The cell deaths and cell velocities for the results using this rotational force are also compared to the system with stem cells restrained in the basal layer in Figure 5.7a and Figure 5.7b. As would be expected, given that the system maintains a consistent stem cell population, the velocities and cell deaths remain close to those of an equivalent system with restrained stem cells.

By using the rotational force, as opposed to the alternative maintenance strategies of pinning cells or increasing membrane adhesion, we provide a system which is able to maintain a higher stem cell population in the basal layer whilst still allowing motility of proliferative cells within the layer. While other methods approach

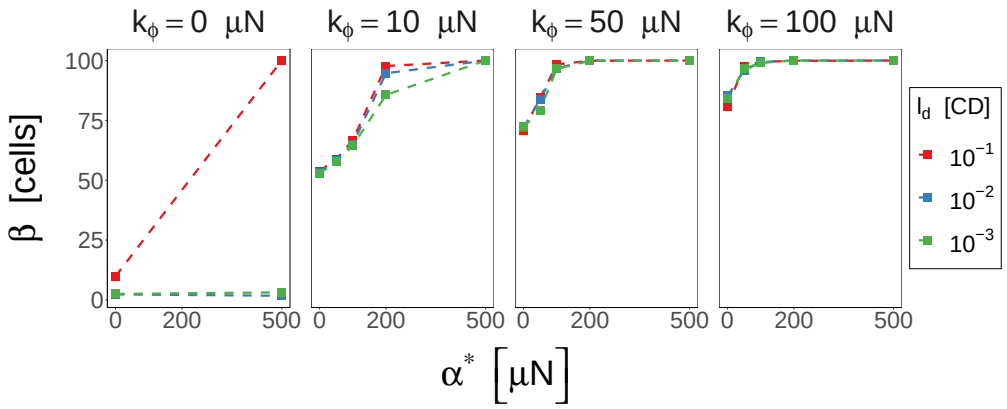

(a) Results with different strengths of rotational force

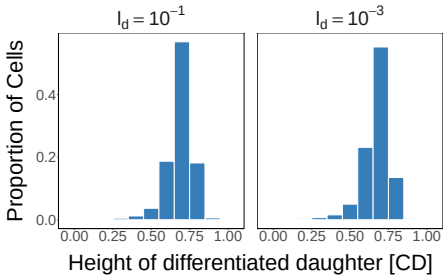

(b) Daughter height

Figure 5.6: (a) The results for the rotational force during the mitotic phase of the cell cycle model. Also shown are the results for the base model at two adhesion levels (left, $k_\phi = 0$). Adhesion levels shown with the rotational force are $\alpha^* = 0$, 50, 100, 200, and 500 μm. (b) The height of the differentiated cell's centre at the end of the M phase of division for the largest and smallest division spring lengths. The rotational spring constant used for these plots was the smallest tested, $k_\phi = 10$ $[\mu N]$, and the membrane adhesion was the same as the base model, $\alpha^* = 500$ $[\mu N]$. The unit of height is cell diameters (CD).

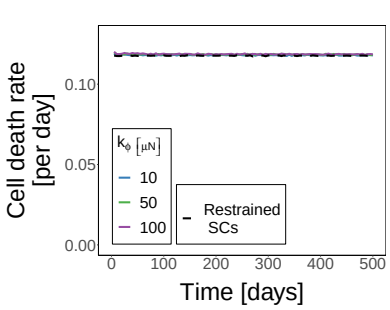

(a) Deaths

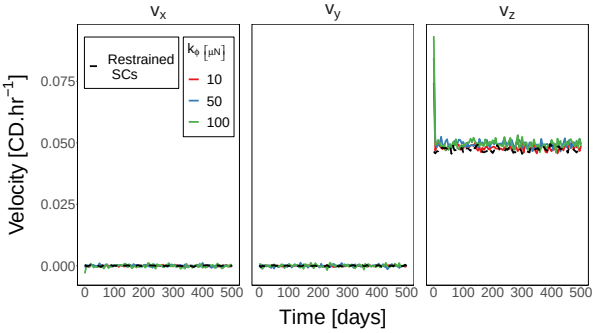

(b) Velocity

Figure 5.7: The new system dynamics with the rotational force included: (a) the cell death rate, as a proportion of the total cell count, and (b) velocities for the different rotational forces. Adhesion to the membrane is $\alpha^* = 500\ \mu N$ and starting spring length at division is $l_d = 10^{-3}$ CD. The dashed black line shows the comparative results for a simulation with vertically restrained stem cells (SC). The unit of velocity is cell diameters (CD) per hour.

the problem by focussing on keeping stem cells in the basal layer, we approach the problem by minimising the number of differentiated cells that enter the basal layer. This novel mechanism is a robust system for simulations on the time scale of months to years using the force magnitudes trialled for this chapter and used previously in the literature.

5.4 Conclusion

We have shown that multicellular models of epithelial tissues require the inclusion of an additional mechanism to maintain a high density of proliferative cells in the basal layer. Using the base model, based on previous models in the literature (without a rotational force), we are unable to maintain high proliferative cell densities in the basal layer of the IFE without a high level of adhesion to the basal membrane. The steady state stem cell densities are particularly low when the spring length

between the daughter cells at division is very small, which is the more biologically realistic spring length. A decrease in the stem cell population significantly affects the dynamics and morphology of the tissue. Particularly, in the case of the IFE, it decreases vertical cell velocities and cell death rates.

We showed that applying a rotational force to the differentiated daughter cell during the M phase increases the homeostatic steady state stem cell density in the basal layer for any given spring length. The rotational force concept is based on the observed regulation of division direction, by the mitotic spindle, during the M phase of the cell cycle. Although it is not known exactly what the density of proliferative cells is in human epidermis, the inclusion of this force has enabled us to produce any stem cell counts wanted. It also allows movement of the proliferative cells in the basal layer where other strategies limit proliferative cell movement. Consequently we have increased the robustness of multicellular IFE models for future research. Our model will produce more reliable results when used to research different aspects of the IFE, as it eliminates the artefacts which occur due to decreased basal populations and atypical cell velocities. Such increased reliability could also be expected if this methodology was implemented in other epithelial tissue where regulation of the mitotic spindle is expected to occur.

Given the simplifications required to implement the division model, these results provide insufficient evidence to assert that the rotational force is biologically significant, however they do suggest a potential role for the division regulation which could be explored further either *in vivo* or *in silico*. Though we only consider perpendicular orientation with asymmetric division in this chapter, the same concept applies for symmetric division parallel to the membrane. As detailed in Section 5.1 there are several opposing theories about the division direction in the basal layer, and this could be investigated using the model. Some open questions remain around incorporating both perpendicular and parallel division directions, the relative performance of the rotational force in parameter spaces outside of the sample space

explored, as well as the effect of misalignment of the spindle on tissue morphology.

6 | Balancing proliferation and desquamation to maintain tissue thickness

The previous results chapter looked at the input of cells to the system, in this chapter we now look at the way cells are removed from the system, via desquamation. We investigate the use of a mechanical model for cell desquamation to maintain tissue thickness. The desquamation model is based on the degradation of cell-cell adhesion towards the top of the epidermis. Once the adhesion is sufficiently degraded, environmental forces remove cells from the tissue. Simulations are used to provide a relationship between tissue thickness, cell proliferation, and the rate of degradation of the adhesion. This model can then be used to investigate the response of the tissue to modifications to the proliferation and desquamation processes. We investigate three different behaviours here: how the system responds when desquamation is stopped and restarted; the effect of multiple proliferative populations; and the effect of stochasticity in the adhesion degradation.

6.1 Introduction

The epidermis helps protect our bodies from external hazards. One contributor to this defence system is the constant turnover of cells, which fully renews the tissue approximately every 4 weeks [21] and is thought to assist in flushing out any toxins which may have entered the system. The flip side of this constant turnover is a requirement for the system to balance the cell input and output in order to maintain an approximately constant tissue thickness. The thickness of the epidermis varies between both body location and individuals, ranging between 50 and 100 μm [31, 78], as was seen in Figure 2.3. Abnormal epidermal thickness, due to either excessive cell loss or accumulation, is associated with conditions such as inflammation or allergies [22].

Cell input in the inter-follicular epidermis (IFE) is due to cell proliferation, which we explored in Chapter 5. Cell output occurs through desquamation of cells from the top of the tissue, as explained in Section 2.4. It is possible to hypothesise mechanisms by which the balance between these processes is maintained. Below, we propose four possible hypotheses, and possible computational models that could be used to model each hypothesis. In order to compare these different hypotheses, we consider how they would respond to a perturbation in the system. Specifically, we consider how the model would respond in the computational equivalent of an experiment by Goldschmidt and Kligman [37] described in Section 2.7 which we will call the *cup experiment*. This experiment is used as the test because it is a rare experiment in which the desquamation process was studied *in vivo* in human epidermis.

In the experiments, Goldschmidt and Kligman [37] protected participants skin from external forces (using a cup) for a period of time and then studied. The results showed that skin cells accumulated on top of the skin (the skin became thicker) during the protected period, but then these cells were easily scraped off upon removal

of the cup. This provides a useful example of the ability of the system to accumulate cells and then recover, with which we can compare the four hypotheses.

The four hypotheses for tissue balance are:

1. Long range signalling, either top down or bottom up, between proliferating and dying cells, such that cell division and cell loss are exactly matched. In this hypothesis, as cells died they would send a signal down to initiate the proliferation. Or, alternately, a cell division would cause a death signal to be sent upwards. Computationally, the equivalent model would be a one-in, one-out policy, where a division caused a death, or a death caused a division. We have not seen any experimental literature that supports this hypothesis. This system would only be able to reproduce the cup experiment if there was an additional process for the cell removal, separate to the cell death. Without this additional process, the enforced equality between cell production and loss means the system will never accumulate cells on top of the tissue.
2. A tightly regulated proliferative cycle time combined with age based cell death programmed into the cells at birth. This hypothesis assumes all information is innately known by the cell. Computationally, this would be implemented by assigning the age at which the cell dies when it is created. Again, we have found no experimental literature to support this hypothesis. In terms of computational results, we would not expect this to vary much from the long range signalling hypothesis (1). It is potentially more restrictive than the the first hypothesis as it also requires precise regulation of the cell cycle times, which has not been seen *in vivo* or *in vitro* [23, 74, 105]. Similarly to the first hypothesis, an additional mechanism, separate to cell death, for cell removal would be required to reproduce the cup experiment.
3. A spatial chemical gradient at the top and bottom of the tissue regulating proliferation and desquamation. Computationally, this would be implemented as either a static gradient, or a gradient coupled to some other process, that

regulated desquamation. The existence of chemical gradients in the epidermis has been seen experimentally. For example, calcium is thought to be involved in the differentiation process [20], however the only gradient we are aware of specifically linked to desquamation is pH, which we will discuss below in Hypothesis (4). A spatial chemical gradient could only reproduce the accumulation of cells in the cup experiment if there was some type of feedback mechanism which caused the gradient to extend when the skin was covered by the cup.

4. A mechanical mechanism in which the adhesion between cells degrades over time and cells are removed due to external forces. Computationally, this mechanism would change the adhesive function for the cell, such that it degraded over time, until the application of the external forces caused it to detach from the tissue. There is much supporting evidence for this mechanical mechanism. It is known that the adhesive molecules between the cells degrade in the stratum corneum, due to different enzyme activities [53, 54, 75]. It is also thought that this degradation is regulated by the pH gradient [22, 88]. This model is able to reproduce the cup experiments, as the removal of the force would mean no cells were separated from the tissue, and would instead build up. During this accumulation period the adhesion would also still have sufficiently degraded such that when the cup was removed and the forces re-applied it would be expected that the tissue would regain its steady state.

For our model we use the adhesion degradation based desquamation method (Hypothesis (4)). Similar desquamation models have been implemented previously by Li et al. [72], Schaller and Meyer-Hermann [108], and Sütterlin et al. [118]. The Schaller and Meyer-Hermann [108] and Sütterlin et al. [118] models degraded the adhesion between cells according to the cell age and time since differentiation respectively, however cells were removed using an adhesion threshold, making removal

rates similar to methodologies based on cell removal at a specified age. Li et al. [72] added an upward force to the Schaller and Meyer-Hermann [108] model to pull cells from the tissue in order to separate and remove them, which is similar to our approach described below. However, the use of a significantly larger magnitude for the upward force than the cell-cell adhesion force, and differences in the definition of which cells are detached, would result in significantly different cell dynamics and looser tissue structures than our model.

In this chapter we use a simple adhesion degradation model based on cell age. In the next chapter (Chapter 7) we propose a more complex, subcellular model for the adhesion degradation based on enzymatic activities. The adhesion degradation desquamation model replaces the sloughing boundary condition described in Section 4.1.2. In this chapter we show that the simple (age based) model is able to maintain a steady state tissue thickness. We then investigate the relationship between proliferation rate, adhesion degradation, and resulting tissue thickness. Finally, we consider how our model:

1. recovers from perturbation, replicating the Goldschmidt and Kligman [37] cup (as described above and in further detail in Section 2.7),
2. varies if two proliferative populations are present in the basal layer, and
3. responds to increasing levels of stochasticity in the degradation of the adhesion.

6.2 Methods

Our model builds on the model first described in Chapter 4 and then extended in Chapter 5. We make two changes to the model in this chapter: a new method for modelling desquamation, and a simple model for the degradation of cell-cell adhesion. Additionally, the cell cycle time in the base parameter set, which we

explore in detail in these results, has been reduced slightly to 12 hours. We use this reduced value as, when combined with the decay rates that were considered, it produces tissue heights close to the 10 CD threshold that was used in Chapter 5, and additionally it gives an easy to work with birth rate per day. Note, the previous value of 15 hours is within the bounds of the parameter sweep performed for this chapter.

Results in this chapter are calculated using 10 realisations for each parameter set. The section below details the implementation of the model additions as well as a description of the *burn-in* period used to ensure the system has reached a steady state. These additions to the model allow us to investigate the relationship between proliferation, degradation of adhesion, and tissue thickness.

6.2.1 A mechanistic model of desquamation

For this investigation, we remove the sloughing based method for desquamation described in Chapter 4 and instead use *force-based cell removal*. In force-based cell removal, a force is applied to the top cells in the tissue, which causes them to begin to separate from the main tissue body. Once a cell, or a set of cells, is completely separated from the main tissue body, it is removed from the simulation. This method can be broken down into three mechanisms: the definition of *top of tissue cells*; the *removal force*; and the definition of *separated cells*. Figure 6.1 gives an example simulation snapshot using this method, with the top of tissue cells shown in green, and the main tissue cells shown in blue. We address each of the three mechanisms individually below, and also show a two dimensional example of the method in Figure 6.2.

Defining the top cells

First, we need to determine which cells are at the top of the tissue. We do this by splitting the horizontal plane into a square grid with grid size Δx. We loop over the

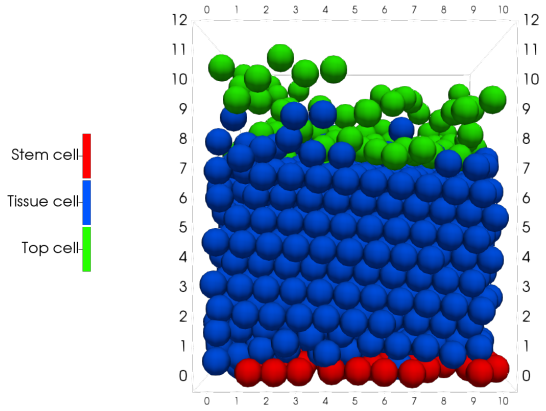

Figure 6.1: Simulation output showing cells in the main tissue, and those labelled top cells.

cell population and determine the highest cell (using the cell centres) in each grid square. This cell is labelled as a top of tissue cell. We refer to these cells as the *top cells* for the remainder of this chapter and thesis.

Intuitively, one would calculate the density of each cell layer to determine an appropriate value of Δx. However, the simulation output does not show cell layers, and therefore it is difficult to determine a cell density. Close to the basal layer, where more layering is present, cell densities are around 1.2 cells/CD^2 (CD: cell diameters). However, after about the fourth layer, the cell arrangement is no longer obviously layered, becoming increasingly random, and cell density starts to decrease. Consequently, for simplicity and symmetry with proliferating cell count we use a grid size of $\Delta x = 1$ CD. This means 100 cells are undergoing desquamation at any point in time, equal to the number of proliferating cells. Changing this grid density does not qualitatively change the results.

Removal force

Once we have identified which cells are the top cells we can then apply the removal force, as shown in Figure 6.2. This vertically upward removal force, $\mathbf{F^D}$ is included as an external force $\mathbf{F}_{\text{ext}}$ in Equation (4.1) in Chapter 4. The removal force is

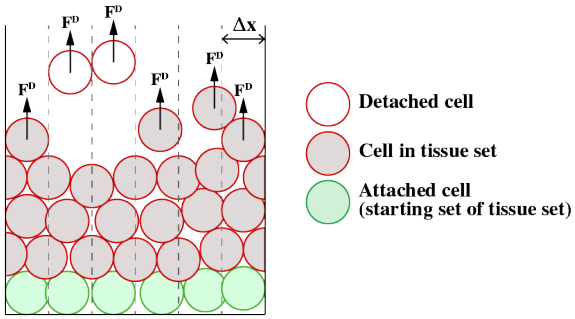

Figure 6.2: The desquamation model. Top cells experience a vertical desquamation force. Once they detach from the tissue they get removed. Detachment is defined by determining the connected tissue set, starting with the set of attached cells.

of set magnitude and is intended to reflect the environmental forces experienced by exposed skin cells. Though we would not expect the forces to be vertical in reality, we neglect the horizontal shear forces for the purposes of our model. What is important is that the bonds between cells are sufficiently broken to allow removal. The reduction in cell-cell adhesion is due to the degradation of the cell-cell bonds, which is known to occur earlier in the vertical direction than the horizontal direction Igawa et al. [49]. Consequently, we believe a vertical force is a good approximation of this process.

Detached cells

Once the force is applied to the top cells, they start to separate from the tissue and so we need to define when cells are no longer connected to the main tissue body. We do this by determining the cell set that constitutes the main tissue body. If we start with a set of cells which we know are in the main body, we can determine which cells are in contact with this set of cells. If we iteratively add the contacting cells to the set, we can repeat this process until no new cells are added to the set. This is then our main tissue body, and any cells not in the set are considered separated,

and consequently removed. We use the set of cells attached to the membrane, as described in Section 4.1.2, as our initial set.

In order for prompt removal of the cells, such that the removal process has minimal effect on the tissue thickness, we use a removal, or desquamation, force of $\mathbf{F_D} = 5\ \mu$N. In the presence of no other forces, a cell experiencing this force would be removed from the tissue in 1.4 hours (12% of the cell cycle). However, as a result of using this increased force for removal, an increased adhesion force is required to counter the effects of this force until the adhesion is sufficiently degraded. For simplicity, we set our adhesion force to twice that of the removal force: $\mathbf{F}^{\mathbf{A}}_{\max} = 10\ \mu$N. We note that this is not the same as setting $\alpha = 10\ \mu$N in the adhesive function (repeated here from Equation (4.5)):

$$\begin{aligned} \mathbf{F}^{\mathbf{A}}_{ij} &= -\alpha\left(\left(s^*_{ij}+c\right)e^{-\gamma\left(s^*_{ij}+c\right)^2} - ce^{-\gamma\left(s^{*2}_{ij}+c^2\right)}\right)\mathbf{n}_{ij}, \\ &\text{where } c = \sqrt{\frac{1}{2\gamma}} \text{ and } s^*_{ij} = \frac{s_{ij}}{r}. \end{aligned} \tag{6.1}$$

The equivalent coefficient value is $\alpha = 374.7\ \mu$N.

Changing this relationship between the expected removal forces and cell-cell adhesion force coefficient would change the point at which the removal occurs during the degradation function, however this would not qualitatively change the results.

6.2.2 Degradation of cell-cell adhesion

The attractive forces between cells represent cellular adhesion, which is provided by corneodesmosomes in the stratum corneum. Corneodesmosomes are desmosomes (see Section 2.3) with additional proteins added during the cell's transition from the granular layer to the corneum. Corneodesmosomes degrade as the cells progress through the stratum corneum [16, 28, 43, 82], resulting in a reduction in cell-cell adhesion. We can represent this as a reduction in the magnitude of our attractive force function (Equation (6.1)). Section 2.3 also details the increasing stiffness gradient in the epidermis, however the effect of this gradient would be the same

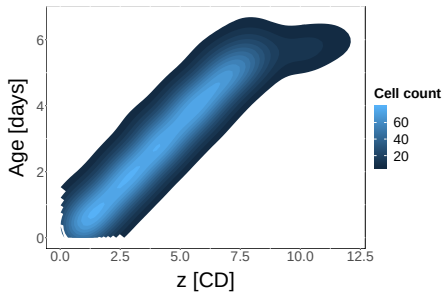

Figure 6.3: A density plot of the ages of the cells varying over the vertical direction of the tissue.

as that of the decreased adhesion in the model, as the desquamation model adds tension and not compression, and hence we do not consider it here.

The degradation of the adhesion begins when the cells enter the corneum. Two biologically reasonable independent variable choices for the degradation function are height of cell or time spent in corneum. Given it would be expected that the degradation would be time dependent, as the process is driven by an enzyme reaction, the simplest way to implement this is as a function of cell age. We also define the point at which the cell enters the corneum using a cell age threshold. This has similar results to defining a cell height for entry to the corneum, as we know that the age is a proxy for cell height—Figure 6.3 shows they they are correlated. This is because the upwards cell movement is due to proliferation, and the proliferating cells are spread approximately uniformly across the basal layer, therefore all cells should move through the tissue at approximately the same rate.

We assume the adhesion proteins degrade exponentially [17], similar to Schaller and Meyer-Hermann [108]. Consequently, the adhesion coefficient, α, between cells follows the function:

$$\alpha = \begin{cases} \alpha_0, & \text{for } a \leq a_d, \\ \alpha_0 \mathrm{e}^{-\lambda(a-a_d)}, & \text{for } a > a_d, \end{cases} \tag{6.2}$$

where a is the age of the cell, α_0 is the normal cell-cell adhesion coefficient, and a_d is the age at which degradation begins. This is shown in Figure 6.4. We set the

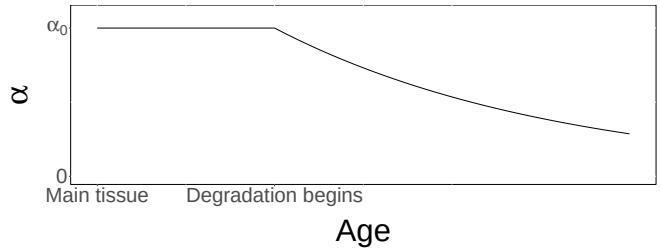

Figure 6.4: The function representing the degradation of adhesion in the upper stratum corneum. Adhesion is constant through the main tissue then degrades after the cell reaches a specified age.

minimum age for degradation, or the expected age at entry to the stratum corneum, to $a_d = 80$ hours. This is equivalent to a cell height, on average, of 4.7 CD for the chosen cell cycle length. Given this degradation occurs on a single cell basis, and the adhesive force is the interaction between the two cells, the actual coefficient used in the force calculation is taken to be the average α of the two cells, as in Schaller and Meyer-Hermann [108].

6.2.3 Burn in period

Similarly to previous chapters, we first simulate a fill period. During this period, cells are sloughed from the tissue and no force is applied. However, given we must define a sloughing thickness during this fill period, the end thickness is not the steady state thickness of the system. Therefore, in order to ensure we are at steady state thickness, we run the system for a *burn-in period* until it has reached a steady state, which is determined visually. We show results for 30 days of simulation, and therefore we set the minimum burn-in time to also be 30 days, giving a total simulated period of at least 60 days. We found, by visual inspection, that this is more than sufficient in all cases for the system to reach a steady state thickness. We only show the results for the final 30 days, and this is the period we use to calculate the steady state.

6.3 Results

In this chapter we investigate the dynamics and stability of a system using degradation of adhesion as a mechanism for cell desquamation at the top of the epidermis. Results are shown for 10 realisations of each parameter set. Thickness plots shown use the mean height of the top cells from the 10 simulations over time, and the steady state thickness is calculated as the mean of this time series. The time series plots for the tissue thickness also show ribbons to indicate the minimum and maximum thickness across the ten simulations. This is also based on the mean height from the set of the top cells.

We begin with a base parameter set with a mean cell cycle length of T_C = 12 hours, and an adhesion decay rate of λ = 0.04 hr^{-1}. For this base simulation we discuss the tissue thickness, density, birth and death rates, adhesion levels, and vertical velocity results. After this we qualitatively, then quantitatively, investigate the effect of changing the cell cycle length and adhesion decay rate parameters. We show the system is able to reproduce the accumulation and removal dynamics expected when replicating the cup experiment of Goldschmidt and Kligman [37]. Finally, we investigate modifications to the properties of the cell cycle model and desquamation model. These modifications are the effects of using two proliferative populations or including stochasticity in the adhesion decay rate.

6.3.1 Degradation of adhesion with force driven desquamation can maintain a steady tissue thickness

Figure 6.5a shows that the system, as described above, is able to maintain a steady state tissue thickness. A video of one simulation can also be found at `https://youtu.be/K4BXPbiYffU`. The results shown are for the base system, with a mean cell cycle time of T_C = 12 hours, and an adhesion decay rate of λ = 0.04 hr^{-1}.

In Figure 6.5a we show both a time series of the minimum and maximum output thickness over the 10 realisations (blue ribbon) and the mean (solid blue line), in addition to the calculated steady state thickness (dashed black line). For this setup, the steady state was calculated to be 9.63 CD. The remainder of this section details the resulting properties and dynamics of the tissue using this desquamation model.

It can be seen in the plot that there is large variation in the thickness over time, as well as spikes in the minimums and maximums. This is mainly due to the method by which the cell removal is modelled. Cells are still considered part of the tissue until they have separated a certain distance from the main tissue, either individually or as a group. Consequently the thickness of the tissue can noticeably increase as groups of these cells are pulled off the tissue. Once these cells have been sufficiently separated, they are then removed from the system, producing a sudden decrease in thickness. Consequently, we would not expect the thickness of the tissue, at high temporal resolutions, to be continuous. Though this happens at a much faster time scale than the output frequency, the time series still reflects this effect.

Figure 6.5b shows the variation in the heights of the top cells in one simulation. This shows the variation in one simulation as cells are pulled upwards and then lost. Though this could potentially have an effect on the determined steady state thickness, it has not been found to be significant. We can see in Figure 6.5c (also clear from the snapshot in Figure 6.1), at the top end of the tissue, close to the steady state thickness, the cells are loosely packed, however are clearly still attached to the main tissue in the snapshot.

In order for this model to maintain a tissue thickness, it must balance cell proliferation and desquamation. This balance can be seen in Figure 6.6. The plot shows the mean rates as solid lines, and the ribbons indicate the range of rates across the simulations. The birth rate (in blue) is maintained at 200 cells.day^{-1} with little variation, which is due to the fact that the cell division time is tightly regulated to be within 10–14 hours. Given 100 cells cycling with T_C = 12 hour cell cycle lengths,

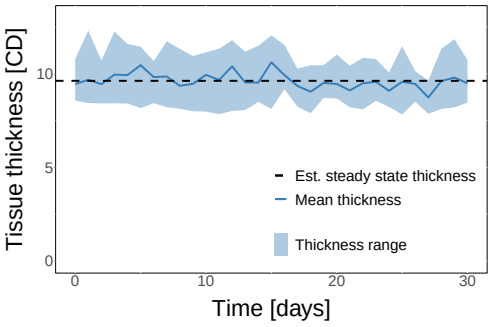

(a) Tissue thickness over time

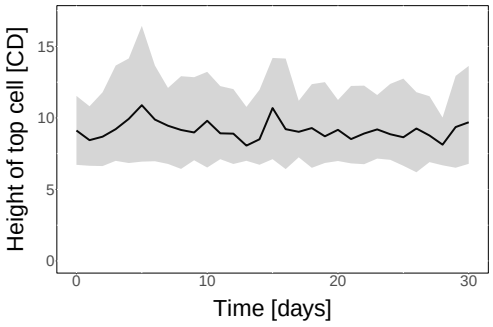

(b) Height of the top cells over time

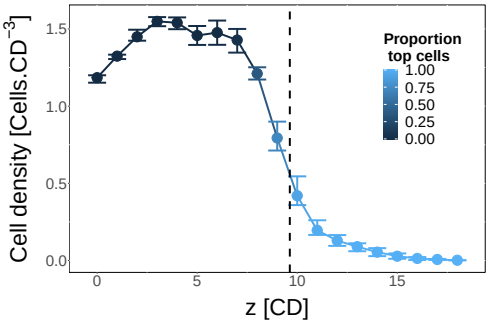

(c) Cell density

Figure 6.5: Tissue thickness and structure data for the base parameter set (T_C = 12 hours and λ = 0.04 hr^{-1}). (a) Time series of tissue thickness. The blue ribbon shows the range of tissue thickness over the 10 realisations, the blue solid line is the mean over time, and the dashed black line is the estimated steady state thickness using the overall mean. (b) The range of the heights of the top of tissue cells for one simulation. The ribbon shows the range of cell heights and the solid line is the mean. The mean is the value used to calculate the thickness in the plot in (a). (c) The change in cell density at different heights in the tissue. Densities are calculated using a moving average ($z \pm 1.5$). The points showing the mean of the simulations and the error bars indicating the range (minimum and maximum) across the 10 realisations. The colour of the points indicates the proportion of the cells at this height that are defined to be top cells. The dashed line shows the calculated steady state thickness.

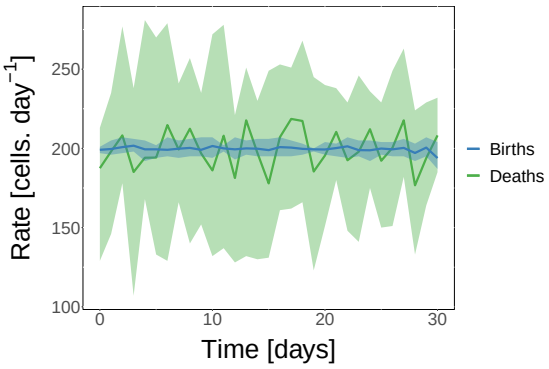

Figure 6.6: Cell birth and death rates for the base parameter set (T_C = 12 hours and λ = 0.04 hr^{-1}). The solid lines indicate the mean over time, while the ribbon shows the minimum and maximum of the daily rates across the 10 simulations.

each cell divides twice a day, resulting in 200 new cells per day. The death rate then balances this (green in Figure 6.6), but has higher variation than the birth rate. This is related to the high variation in thickness seen in Figure 6.5a. As explained above, cells are removed intermittently in clumps, resulting in a relatively high variation in cell deaths.

Figure 6.7a shows the level of adhesion in the cells over the height of tissue for one simulation at the end time step. The median adhesion at the steady state thickness, z=9.6 CD (estimated by $z \in [9.55, 9.65)$), over all simulations is 0.98 μN. We can see the majority of cells follow the same degradation path with cell height, and are therefore maintaining the same velocities upwards through the tissue. However, there are still large variations in the adhesion—at z=9.6 CD the level ranges from 0.1–2.6 μN—from when the cells begin to degrade until desquamation.

The final property of the system we consider is the cell velocity. The average velocity of the cells in the tissue, excluding stem and top cells, is 0.055 CD.hr^{-1}, while the average velocity of the top cells is 0.36 CD.hr^{-1}. The average tissue cell velocity, as expected, is approximately equal to the product of the birth rate of each

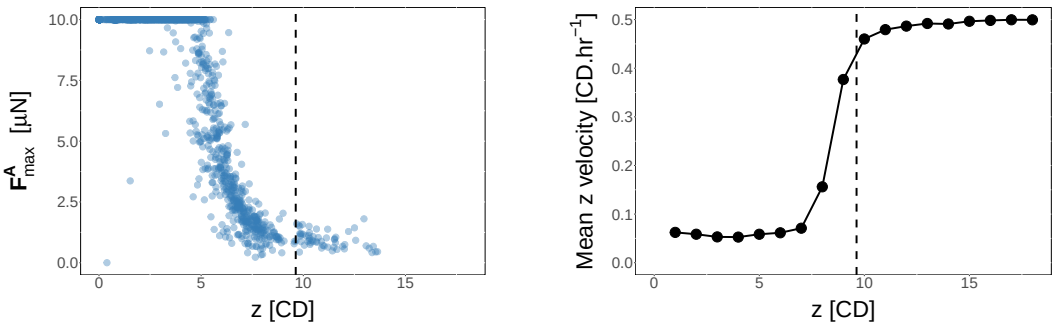

(a) Adhesion of each cell

(b) Change in velocity over height

Figure 6.7: Tissue dynamics for the base parameter set (T_C = 12 hours and λ = 0.04 hr^{-1}). (a) The adhesion of each cell at the final time step in one simulation. (b) Change in cell velocity varying with height, as an average of all 10 simulations. These results do not show the cells attached to the membrane, as these have a negative velocity due to their stronger adhesion to the membrane. The dashed lines on both plots indicate the calculated steady state thickness of the tissue.

stem cell (2 per day) and the inverse of the cell density (approximately 0.7 cells.CD^{-2} in the lower layers, z<8 CD). In Figure 6.7b we can see the change in the velocity over the vertical direction in the tissue. Note, we have not included error bars in this plot, and in the other velocity profiles presented in this chapter, as the range of velocities occurring in the first couple of layers in the CD is significantly higher than the range observed in the profile, and hence the profile is lost. The reason for this high range in these first couple of layers is due to the large (instantaneous) repulsive forces occurring due to proliferation.

Figure 6.7b shows the velocity at the base of the tissue is close to the average tissue velocity. There is a slight increase closer to the basal layer due to the strong upwards force from the basal proliferation. The velocity starts increasing again at around z=5 CD, with much steeper increases seen between z=7 CD and z=9 CD. It is in this region that the cells are beginning to be affected by the removal force.

At first, the forces keeping the cells attached to other cells in the tissue dominate, but this quite quickly switches to be dominated by the removal force, due to the steep drop in adhesion seen at the same heights in Figure 6.7a. When z>9 CD, the velocities are within 10% of the expected velocity for a cell experiencing only the removal force.

So far we have considered the structure and dynamics of a single set of parameters. We have shown that the system is able to maintain a steady state thickness, balancing the proliferation and desquamation processes. Additionally, we have investigated the dynamics of the system and discussed how they are linked to the proliferation rates and desquamation model. In the sections following, we extend these results to consider how changes to parameters and behaviours affect the system.

6.3.2 Determining the relationship between adhesion decay, cell cycle length, and tissue thickness

We can vary the decay rate of the adhesion and the cell cycle length to 'tune' our tissue thickness. If we run a sweep of these parameters we can determine a steady state thickness for each parameter set. These are calculated as described above: by taking the mean of 10 simulations over 30 days, after the simulation has reached a steady state.

Changes in steady state thickness reflect expected behaviours

We first look at the change to a single parameter: the cell cycle length (T_C). The steady state thickness (τ_{ss}) results for different cell cycle lengths are shown as the solid line in Figure 6.8a, for the mean of 10 simulations, with the calculated steady state shown as the dashed line. These results show that τ_{ss} decreases with increasing cell cycle length, $\mathrm{T_C}$. Increasing the cell cycle length decreases the rate of prolif-

eration which causes a decrease in the velocity of the system. This can be seen in Figure 6.8b, mainly at the lower values of z. Decreasing the velocity decreases both the cell height at which the degradation begins and the difference in cell height between the start of degradation and the removal, given the expected time until desquamation is constant if the decay rate remains constant. Though it would be expected that we could directly predict the cell velocity based on the proliferation rate, this does not provide an accurate estimate. Decreasing the cell cycle time, and consequently increasing the frequency of division events, increases the density of the system, as seen in Figure 6.8c, adding a secondary effect on the cell velocities.

In Figure 6.8a, the calculated steady state for each cell cycle time, T_C, is shown by a dashed line. If we then calculate steady state thickness for different adhesion decay rates (λ), we can compare the thickness for different combinations of the two parameters. Figure 6.9 compares the steady state thickness, τ_{ss}, of different decay rates as a function of the inverse of the cell cycle length. We use the inverse of cell cycle length because we expect the thickness to be dependent on the velocity, which depends on the inverse of the cell cycle length, or the rate of cell input. We see that this is not a precise estimate as the plot is not linear. This is in part due to the change in cell density in the tissue at the different proliferation rates, as mentioned above and shown in Figure 6.8c. Additionally, in order for this relationship to be linear, the average age of the top cells need to be constant, which they are not. At short cell cycle lengths, the average age is higher than at long cell cycle lengths. This is also likely explained by the increased cell density of the tissue. Higher cell density has a twofold effect on increased cell age at desquamation. Firstly, it increases the number of cell neighbours, therefore requiring cell adhesion to degrade to lower levels to separate from surrounding cells. Secondly, as the cell moves upwards due to the removal force, the compressed cells underneath also move upwards due to the repulsive forces experienced from the lower layers. If the lower layers of cells move upwards at velocities close the velocity of the top cells, it will take longer for the

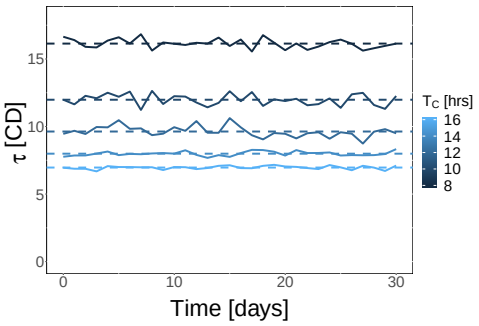

(a) Tissue thickness time series

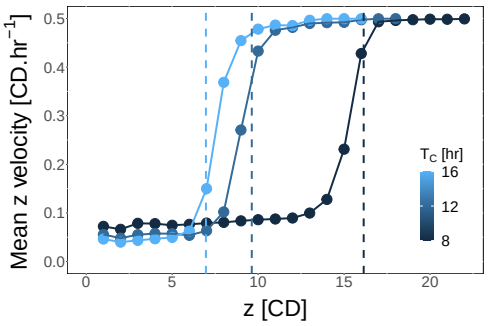

(b) Vertical velocity

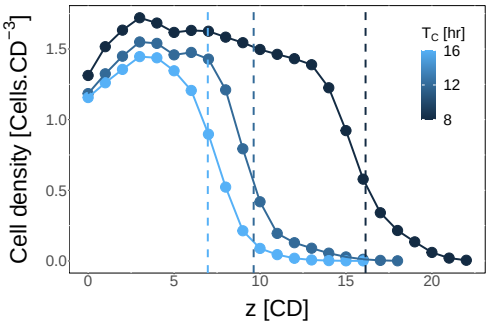

(c) Density

Figure 6.8: Time series results for different values of cell cycle length (T_C). The decay rates for these results is λ = 0.04 hr^{-1}. (a) The tissue thickness, τ. (b) The cell velocity over height for three different cell cycle lengths (minimum, base, and maximum). (c) The cell density over height for three different cell cycle lengths (minimum, base, and maximum). The dashed lines on all plots indicate the calculated steady state. (Error bars were not included for readability).

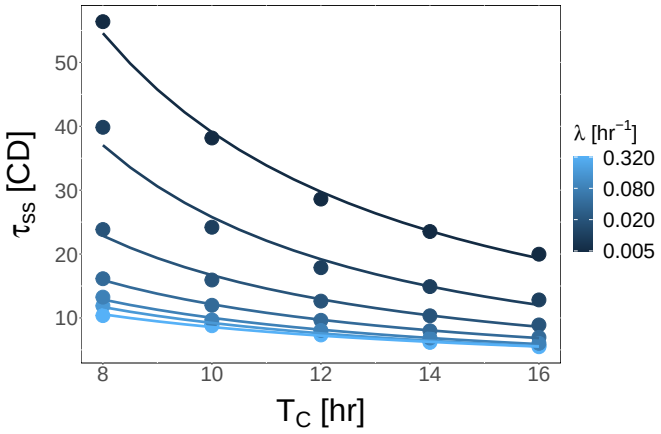

Figure 6.9: The estimated steady state thickness (τ_{ss}) against cell cycle length T_C. The colour shows the value of the adhesion degradation rate, with the colour bar given at a log scale. The lines shown are fits to the data. λ values are: 0.005, 0.01, 0.02, 0.04, 0.08, 0.16, and 0.32 hr^{-1}.

cells to separate.

The second parameter we change in Figure 6.9 is the adhesion decay rate, λ. The results show decreasing λ increases steady state thickness, τ_{ss} (note the colour bar in the plot is on a log scale). This is expected as, decreasing the decay rate increases the time required for the cell to degrade sufficiently for desquamation.

A further behaviour seen in Figure 6.9 is the decreasing sensitivity of τ_{ss} at high values of λ. Given the time until cells are lost is equivalent to the time until sufficient degradation of adhesion for desquamation, we would expect the time until loss to be correlated with the half life of the degradation. Therefore, it could be expected that τ_{ss} would show a similar trend. Note that this is eventually limited by our force parameter choice. When the time until degradation is less than the time taken for a cell to separate from the tissue, the separation time would be the dominant factor.

Here, we have discussed qualitatively how the two different parameters affect the thickness of the tissue—increasing cell cycle length or adhesion decay rate decreases the thickness of the tissue. Each of these results can be explained as a balance of

cell input, controlling cell velocity, and cell output, controlled by adhesion decay rate. Below, we aim to quantify these changes.

Predicting adhesion degradation rate to produce a desired tissue thickness

The lines shown in Figure 6.9 are fits to the point data for steady state thickness (τ_{ss}) as a function of cell cycle length (T_C). We determined a possible fit to the data to be

$$\tau_{ss} = b_2 \, {T_C}^{b_1}. \tag{6.3}$$

This function was chosen as it appeared to provide a close fit to the data (on a log-log plot) with a minimum number of parameters to avoid overfitting the data. Equation (6.3) gives the parameters values for b_1 and b_2 shown as points plotted against the sampled values of λ in Figure 6.10. Performing a second regression on b_1 and b_2 produces a function for the two cell cycle function parameters with respect to the decay rate. Again, we determine the function based on best fit with a minimum of parameters. This gives the following functions, also shown by the lines in Figure 6.10:

$$b_1 = 0.158 \log(\lambda) - 0.759, \tag{6.4}$$

$$\log(b_2) = -0.731 \log(\lambda) + 3.266. \tag{6.5}$$

Rearranging these equations, we can estimate the degradation rate required, given some cell cycle length, to produce a desired steady state tissue thickness:

$$\lambda = \left(0.0382 \, \tau_{ss} \, {T_C}^{0.759}\right)^{\frac{1}{c}}, \tag{6.6}$$

$$\text{where } c = 0.158 \log(T_C) - 0.731 \, . \tag{6.7}$$

This is useful in a modelling context, but can also provide insight into the adhesion degradation rates required for a homeostatic tissue. This could be done by linking this equation to experimental investigations into the parameters of cell cycle time,

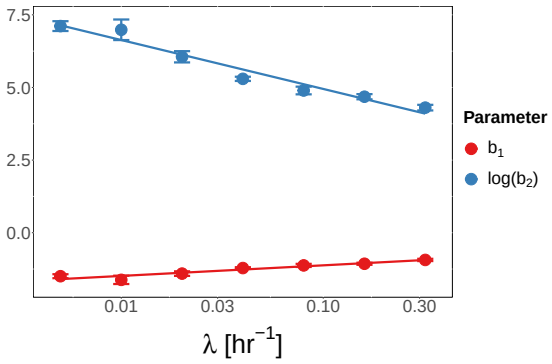

Figure 6.10: Parameter values for the steady state thickness as a function of cell cycle length. The points show the parameter values calculated for each decay rate level. Error bars show the standard error on the fitted parameter (±1 s.e.). The line shows a second fit to these parameter values.

tissue thickness, and degradation of adhesion. However, due to the use of a shortened cell cycle, spherical (rather than flattened) cells, and a decreased number of cell layers for computational efficiency, it would be expected that the adhesion decay rates would be much slower *in vivo*. Consequently, to be experimentally relevant it would be necessary to scale the variables accordingly, once relevant data becomes available. It is also important to note that this relationship has only been calculated for a subset of the potential parameter space of the system, and as such it may not hold outside of the sampled parameter space. Additionally, the results are dependent on the relationship between the maximum adhesion value and the removal force used.

6.3.3 Recovery from perturbation

We can use our model to replicate the cup experiment from Goldschmidt and Kligman [37] described in Sections 2.7 and 6.1. In order to do this we start with 10 realisations of the steady state system, as shown in Section 6.3.1. We then turn off the removal force. During this period cell-cell adhesion is still degrading in the corneum cells but there is no removal of cells from the tissue. This replicates the cup being

applied to the skin in the experiment. After a short amount of time (3 days) we then re-apply the force to the system. This is a much shorter time period than in the experiment (3–6 weeks), however we, firstly, use a much faster proliferation rate than is expected in human epidermis and, secondly, this result can only provide proof that the model is able to qualitatively reproduce the experiment as the original study did not provide data on the increase in thickness. As can be seen in Figure 6.11a, once this removal force is re-applied, the system quickly recovers the steady state.

This is expected, given that most cells at the top of the tissue would have very little cell-cell adhesion, and consequently would be removed by the force with minimal resistance. This provides strong support for this desquamation mechanism, as opposed to the other methods hypothesised in Section 6.1 which would be unable to easily reproduce either the initial increase in thickness, or the subsequent increased rates of desquamation when the cup is removed.

Figure 6.11b shows the birth and death rates for the system. We would expect these to be approximately 200 cells.day^{-1}—the same as the base system—until the desquamation force is turned off (30 days). With no removal force applied to the system, we would expect the birth rate to remain unchanged, as we are not changing proliferation, but the cell loss to drop to zero. When the force is re-applied the death rate should jump higher than the base rate, as the accumulated cells quickly separate from the tissue and are removed, and then settle back to the base rate. This is exactly what is seen in Figure 6.11b.

6.3.4 Two proliferative populations

As discussed in Section 2.2, and shown in Figure 2.6a, experiments have shown evidence of two potential populations of proliferative cells exist in the basal layer with significantly different T_C values. We investigate the effect of two proliferative populations in our model by comparing different combinations of fast and slow

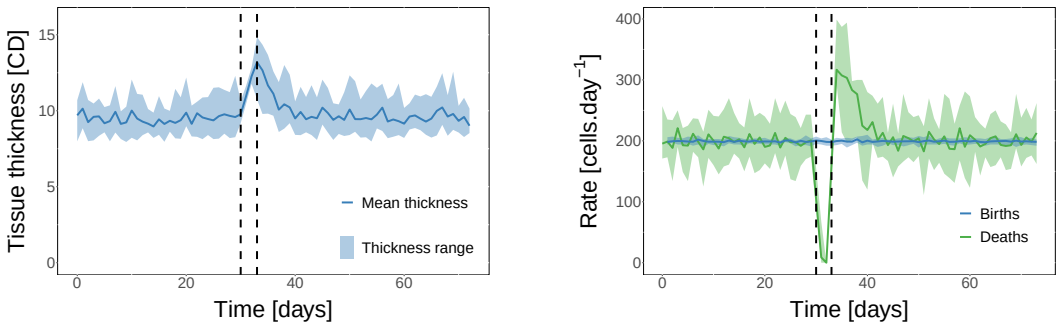

(a) Time series of tissue thickness

(b) Time series of birth and death rates

Figure 6.11: Time series plots showing the system response replicating the cup experiment of Goldschmidt and Kligman [37]. The parameters are the same as the base parameters (T_C = 12 hours and λ = 0.04 hr^{-1}). The ribbons show the maximum and minimum of each simulation. The solid line is the mean. The desquamation force is turned off at day 30, and then re-applied at day 33. (a) The thickness of the tissue. (b) The birth and death rates of the tissue, given 100 stem cells proliferating twice a day.

cycling stem cell populations with either the same expected average cell cycle time, $\mu(T_C)$ = 12 hours, or the same harmonic mean, $H(T_C)$ = 12 hours. The harmonic mean accounts for the fact that the fast cycling cells will undergo more cycles than the slow cycling cells. Due to this behaviour, we would expect an increased number of divisions than would be inferred from the arithmetic mean.

To implement the two populations, we set 50% of the cells to be fast cycling: $T_C = T_1$, and 50% to be slow cycling: $T_C = T_1 + \Delta T_C$. We choose a range of values for ΔT_C and then T_1 is determined based the requirement for the same arithmetic or harmonic mean. For the arithmetic mean, the equation for T_1 is therefore:

$$T_1 = 12 - \frac{1}{2}\Delta T_C\,, \tag{6.8}$$

and for the harmonic mean it is:

$$T_1 = 6 - \frac{\Delta T_C}{2} + \sqrt{\left(\frac{\Delta T_C}{2}\right)^2 + 36}\,. \tag{6.9}$$

The allocation of the fast or slow cycle length to stem cells is random. Due to the cell lineage chosen (Section 4.2.2) and the maintenance of the proliferative population (Chapter 5), all stem cells in the system are immortal. Consequently, the ratio of fast to slow cells in the simulations persist at 50:50.

The corneum thickness for different ΔT values are shown in Figure 6.12a for the arithmetic mean, and Figure 6.12b for the harmonic mean. Using the arithmetic mean, we could expect the fast cycling population to dominate the system, as more proliferation events occur for these cells. Consequently increasing cycle difference, $\Delta \mathrm{T_C}$ is equivalent to increasing the cell input rate, and therefore increases the tissue thickness. This can be seen in Figure 6.12a. Comparatively, as seen in Figure 6.12b, increasing the cycle difference, but maintaining the same harmonic mean, produces the same steady state thickness. This is because the equation to calculate the harmonic mean accounts for the increased count of events occurring for cells with higher rates. Therefore we can approximate the expected steady state thickness of a system with two populations of proliferative cells by a single population system with cycle time equal to the harmonic mean of the two populations.

6.3.5 Stochasticity in the degradation

We would expect that the degradation rate may not be precisely the same across all cells. Consequently, we investigate including stochasticity in the degradation rate, similarly to the way in which we incorporate stochasticity in the proliferation rate. A degradation rate is assigned to each cell at birth, based on a uniform distribution:

$$\lambda_i \sim U(0.04(1-\delta), 0.04(1+\delta)),$$

for some level of variation $\delta \in [0, 0.8]$, giving an expected value of $\mathbb{E}(\lambda) = 0.04$ hr^{-1}. Results for different values of δ are shown in Figure 6.13, and a video of one simulation ($\delta = 0.8$) can be found at `https://youtu.be/17rm61Rhc7s`.

Figure 6.13a shows increasing the stochasticity increases the steady state thick-

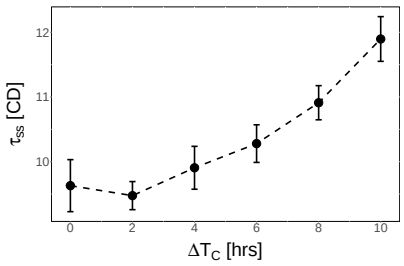

(a) $\mu(\mathrm{T}_1, \mathrm{T}_1 + \Delta\mathrm{T}_\mathrm{C}) = 12$ hrs

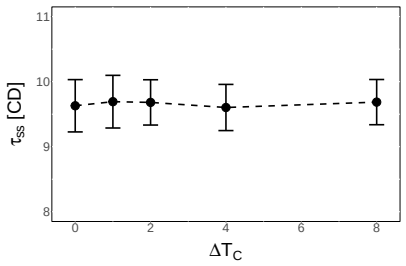

(b) $H(\mathrm{T}_1, \mathrm{T}_1 + \Delta\mathrm{T}_\mathrm{C}) = 12$ hrs

Figure 6.12: Results from simulations with 2 proliferative populations. The dots are the mean thickness (τ_{ss}) of the 10 realisations, and the bars indicate the standard deviation. (a) The corneum height increases with increasing $\Delta\mathrm{T}_\mathrm{C}$ for a two population simulation where the arithmetic mean is kept constant. (b) The corneum height is approximately constant with varying $\Delta\mathrm{T}_\mathrm{C}$ for a two population simulation where the harmonic mean is kept constant.

ness. We can explain this using the level of adhesion at different heights for different levels of stochasticity, shown in Figure 6.13b. As the cells enter the critical region for adhesion decay (around $z = 10$ CD) the variation in the no stochasticity system is small. In the high stochasticity system, it is significantly larger (by a factor of 3.5). Though the majority of the cells are at lower adhesions, the dynamics appears to be dominated by the higher adhesion cells. This is likely to be due the the following inequality:

$$\frac{1}{2}\left(\mathrm{e}^{-\lambda(1-\delta)T} + \mathrm{e}^{-\lambda(1+\delta)T}\right) > \mathrm{e}^{-\lambda T}, \qquad \forall\, T > 0\,. \tag{6.10}$$

The right hand side of this equation is the adhesion between two cells with no stochasticity in the degradation rate ($\delta = 0$) at some time T after the onset of degradation. The left hand side is the adhesion between two cells at either end of the distribution ($\delta > 0$), such that the average degradation rate of the two cells is equal to the base degradation rate λ. The left hand side can be re-arranged to give:

$$\mathrm{e}^{-\lambda T}\cosh\left(\lambda\delta T\right)\,, \tag{6.11}$$

which, given $\cosh(x) > 1\,\forall x \neq 0$, proves the inequality in Equation (6.10). Con-

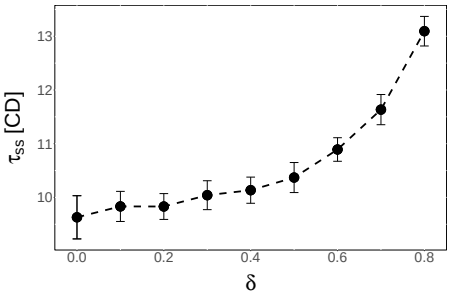

(a) Steady state thickness

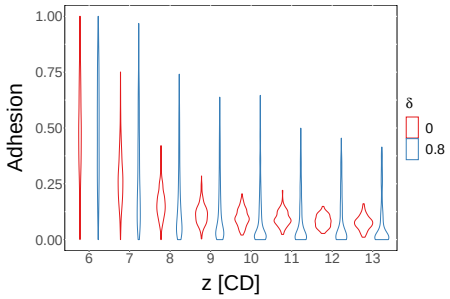

(b) Level of adhesion (z is truncated).

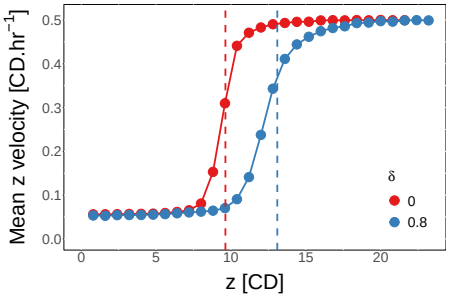

(c) Vertical velocity

Figure 6.13: Results for systems with stochasticity in the decay rate. The decay rates very uniformly between $0.04(1-\delta)$ and $0.04(1+\delta)$. (a) The change in tissue thickness (τ_{ss}) with increasing variation in decay rate. (b) A violin plot showing the level of adhesion in the cells over height (truncated at both ends) for both the no stochasticity and maximum stochasticity results. (c) The vertical velocity over height for the no stochasticity and maximum stochasticity results. The dashed lines indicates the steady state height for each variation level.

sequently, the presence of the higher adhesion cells increases the cell-cell adhesion levels on average.

The final property of the stochastic system we will consider is the cell velocities. Given we are not changing any aspect of proliferation, we expect that the velocity in the main tissue is the same. This can be seen in Figure 6.13c. At the lower heights, the velocity is the same. The results diverge when the removal force becomes the dominant force on cells, which occurs at an increased height for the high variation system due to its increased thickness.

6.4 Summary

Maintaining a homeostatic tissue thickness in a multicellular model requires balancing cells entering the tissue, through proliferation, and cells lost from the tissue, through desquamation. In this chapter, we seek to better understand the mechanics behind this balance. Our results show that it is possible to reproduce a tissue that maintains a steady state thickness by modelling desquamation through a removal force and cell adhesion degradation. In addition, we show that the system is able to recover from a perturbation in a manner that has been observed experimentally. By changing the cell cycle time and degradation rate, we are effectively changing the input and output rates of cells to the tissue, and consequently we can find a relationship between these two parameters and the tissue thickness.

Using this model we are able to investigate the effect of modifications relating to cell input and output behaviours. The first, concerning cell input, is the presence of two populations of proliferative cells in the basal layer. We find that, with respect to steady state heights, two proliferative populations is the equivalent of a single proliferative population with cell cycle length equal to the harmonic mean of the two population cell cycle lengths. The second, relating to the cell output, is stochasticity in the level of adhesion degradation occurring in the cell population. Increasing the

stochasticity in the degradation rate increases the thickness of tissue. This is because the sum of two exponentials with decay rates λ_i and λ_j is always greater than one exponential with a decay rate equal to the mean of λ_i and λ_j.

In this chapter we have been able to reproduce a homeostatic tissue using this mechanics-based approach, however we are also interested in understanding the subcellular mechanics behind this degradation of adhesion. In the following chapter, Chapter 7, we detail how this degradation is thought occur at a molecular model and use this to generate a system of ODEs for the subcellular mechanics. This is then combined with the multicellular model in Chapter 8 to produce a multiscale model. Using this model, we are able to replicate experiments shown in this chapter, and further investigate the dynamics of the tissue.

7 | Subcellular control of adhesion degradation

This chapter describes a model of the subcellular interactions regulating the degradation of cell-cell adhesion molecules. The regulation of this degradation process is necessary to enable the desquamation of cells at the top of the tissue. The subcellular interactions observed are reflective of an enzyme-substrate interaction with a competitive inhibitor. Therefore, we model them using enzyme kinetics to produce a set of ODEs to include for each cell in our multicellular model. The end of this chapter provides an analysis of these ODEs for a single cell. Implementation of the ODEs and results in the multicellular model are provided in the next chapter.

7.1 Degradation of cell-cell adhesion in the stratum corneum by KLK enzymes

The stratum corneum, or corneum, as previously detailed in Section 2.3, is the outermost layer of the epidermis. It is from this layer that cells are lost through the desquamation process. A critical part of the desquamation process is the degradation of cell-cell adhesion.

Throughout the epidermis, the cell-cell adhesion is due to desmosome adhesion molecules, which were described in detail in Chapter 2. The addition of cor-

neodesmosin transforms the desmosomes into corneodesmosomes as the cell transitions from the granular layer to the corneum. These corneodesmosomes are then degraded via an assortment of proteases (enzymes) [54, 75]. An illustration of the reorganisation and degradation of these desmosomes are shown in Figure 7.1.

The degradation of the corneodesmosomes is not uniform around the circumference of the cell. It occurs initially in the vertical direction on the horizontal surfaces of the flattened cells, and then in the planar direction [49]. This is thought to possibly be due to the presence of other adhesion protein complexes called tight junctions, which potentially limit access to the the corneodesmosomes by the proteases [49].

Kallikrein serine proteases (KLKs) degrade the proteins in corneodesmosomes [10, 22, 26, 75]. KLK molecules are released by the cell, via lamellar bodies, at the base of the corneum [54]. Other families of proteases are also known to contribute to degradation, however we only consider KLK proteases as they are thought to be the primary enzyme, and are consequently the most studied [17, 53, 22, 17]. The data available on this process is mostly limited to KLK5 and KLK7 [17, 22]. KLK5 constitutes around 10% of the proteases and KLK7 constitutes 36%. However, KLK5 is a trypsin-like KLK while KLK7 is chymotrypsin-like. The remaining 54% of KLKs are all trypsin-like, and therefore we assume KLK5 has properties more representative of the majority than KLK7. As a result, for simplicity, we limit our analysis to KLK5 and assume the other KLKs all work in a similar fashion.

In addition to KLKs, lamellar bodies also secrete the protein LEKTI [53]. LEKTI interacts with the KLKs to inhibit the cleaving of the cornedesmosomes [32, 53, 66]. This inhibition is regulated by the local pH, which varies vertically through the corneum. The pH gradient changes from neutral in deep corneum to acidic in superficial corneum [88]. At neutral pH there is a high level of interaction between LEKTI and KLK, while low pH increases dissociation of LEKTI and KLK, allowing for higher rates of corneodesmosome degradation [22]. The pH gradient is hypothesised to occur due to other enzymatic activity in the corneum [51]. In this thesis, we

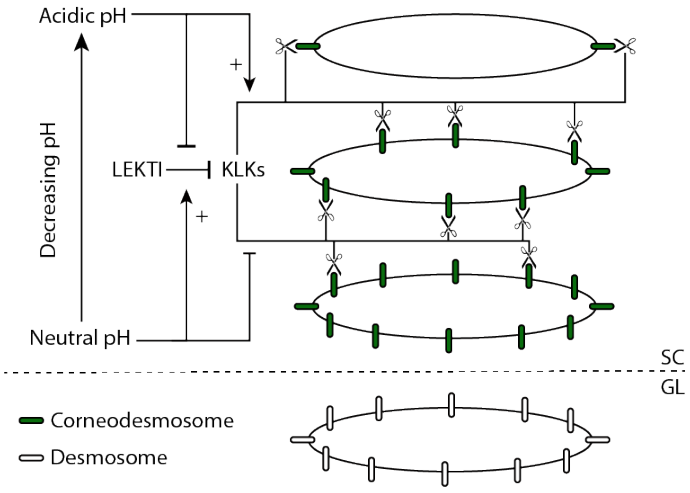

Figure 7.1: A diagram representing the involvement of pH, LEKTI, and KLKs in the desquamation process. Desmosomes (white ellipses) are converted to corneodesmosomes (green ellipses) as they enter the stratum corneum (SC in figure) from the granular layer (GL in figure). These corneodesmosomes are then degraded by KLKs, first on the horizontal surfaces then the vertical (indicated by the scissors). The degradation process is inhibited by LEKTI, which binds with the KLKs and stops the KLKs from binding with the corneodesmosomes. The local pH regulates the inhibition, as well as the corneodesmosome degradation rate by KLKs. Arrows with '+' symbols indicate the pH increases the reaction, while '⊣' indicates an inhibitive reaction or that the pH reduces the rate of a reaction.

assume the pH gradient is fixed for the tissue and do not include any further detail.

In addition to regulating the LEKTI/KLK interaction, the pH also directly contributes to regulation of the degradation process. At neutral pH (deep corneum) the rate of degradation of the corneodesmosomes by the KLK protease is thought to be lower than that at low pH (superficial corneum). These interactions are all summarised in the diagram shown in Figure 7.1.

7.2 Enzyme kinetics

Figure 7.1 illustrates a group of enzymes: KLKs, that break down a substrate: the corneodesmosome, to produce a product: the degraded corneodesmosome. LEKTI inhibits the interaction between the KLKs and the corneodesmosome by binding to the KLKs, and so consequently it is an inhibitor, making the reaction an enzyme reaction with competitive inhibition. Such a reaction can be modelled using mass action kinetics, which describes the rate of interaction for each of the molecules in a chemical reaction. This section will provide background on the mathematical formulation of mass action kinetics models for an enzyme reaction with competitive inhibition, and the use of quasi-steady state approximations. How we apply these models to our system is described in Section 7.3.

The law of mass action states that the rate of a reaction between two chemical species is equal to the product of their concentrations and a rate parameter, k, unique to that interaction and reaction conditions such as temperature. For example, for a simple system in which two reactants, A and B, react to form a product, P, according to the chemical equation:

$$\mathrm{A} + \mathrm{B} \xrightarrow{k} \mathrm{P}, \tag{7.1}$$

the rate of the reaction is given by:

$$\frac{\mathrm{d}[P]}{\mathrm{d}t} = k[A][B], \tag{7.2}$$

where [X] denotes the concentration of chemical species X. This model is probability based—the rate of the reaction is the product of the expected number of collisions (proportional to the concentrations) and the probability that a collision results in a reaction [60, 87].

In simple systems, such as Equation (7.2), it is possible to solve the rate equations analytically for the concentrations of reactants and products over time using conservation laws. However, often the system is more complex and this is not possible.

For example, in the enzyme reaction we base our system on:

$$\mathrm{E} + \mathrm{S} \underset{\mathrm{k}_{-1}}{\overset{\mathrm{k}_{+1}}{\rightleftharpoons}} \mathrm{C} \xrightarrow{k_2} \mathrm{E} + \mathrm{P}, \tag{7.3}$$

an enzyme (E) and a substrate (S) interact to form a complex (C), which then decomposes into the product (P) and releases the enzyme back into the system [60, 80, 87].

For this reaction it is necessary to make some assumptions to simplify the system. The quasi-steady state approximation is one such simplification that is often used in enzyme kinetics [87]. This approximation, proposed by Briggs and Haldane [13], assumes that the concentration of enzyme is much smaller than the concentration of substrate. Consequently, the change in concentration of the complex is negligible and $\mathrm{d}[C]/\mathrm{d}t \approx 0$ [13, 60, 87]. This gives the following solution for the reaction rate V as a function of the concentration of substrate $[S]$:

$$V = -\frac{\mathrm{d}[S]}{\mathrm{d}t} = \frac{k_2[E]_0[S]}{[S] + K_M}, \tag{7.4}$$

$$\text{where } K_M = \frac{k_{-1} + k_2}{k_{+1}}. \tag{7.5}$$

K_M is known as the Michaelis constant [60, 87].

The final element of the system is the inhibitor LEKTI. There are several ways that LEKTI could interact with the enzyme to inhibit the left hand reaction in Equation (7.3). Here we only consider competitive inhibition, where the inhibitor binds to the same site on the enzyme as the substrate, therefore blocking the substrate from binding to this site [60].

The process of competitive inhibition can be represented as an extension of Equation (7.3) with a second equation for the inhibitor (I) reaction:

$$\mathrm{E} + \mathrm{S} \underset{\mathrm{k}_{-1}}{\overset{\mathrm{k}_{+1}}{\rightleftharpoons}} \mathrm{C_S} \xrightarrow{k_2} \mathrm{E} + \mathrm{P}, \tag{7.6}$$

$$\mathrm{E} + \mathrm{I} \underset{\mathrm{k}_{-3}}{\overset{\mathrm{k}_{+3}}{\rightleftharpoons}} \mathrm{C_I}. \tag{7.7}$$

Note, if $[I] = 0$ in this equation, it simplifies to Equation (7.3). This system can be simplified using quasi-steady state assumptions for both $[C_S]$ and $[C_I]$ to produce solutions for the reaction rate V as a function of $[S]$ and $[I]$ [60].

Equations (7.6) and (7.7) is the model we use in this chapter. The following section describes how we use these concepts of enzyme kinetics, quasi-steady state approximations, and competitive inhibition to produce a system of differential equations to represent the adhesion degradation.

7.3 A model of adhesion degradation

We are interested in developing a subcellular model of the adhesion degradation over time that was shown in Figure 6.2. This model takes a spatial pH gradient as an input, and then models the interaction between LEKTI, KLKs, and corneodesmosomes (CNDs) for each cell individually using a set of ODEs. The parameters in this system change as the cell moves up through the tissue and experiences the pH gradient. The output of this model is the proportion of adhesion CND molecules remaining for each cell, which scales the adhesive force of the multicellular model (see Section 4.1.1). We ignore any non-uniformity of adhesion degradation around each cell, as the driving forces we use to mimic the desquamation process all occur in a vertical direction.

This section describes the ODEs and parameters used for the subcellular model, and the process by which these were derived. We normalise the system such that each variable varies from zero to one, exclusive of pH.

7.3.1 A system of differential equations

We convert the system described in Figure 7.1 into the competitive inhibition chemical equations shown in Equations (7.6) and (7.7) where E is the KLK enzymes, S is corneodesmosome adhesion proteins, I is the inhibitor LEKTI, P is the prod-

uct(s) corneodesmosome degradation produces, C_S is the complex formed between the KLKs and the corneodesmosome, and C_I is the complex formed between the KLKs and LEKTI. All rate parameters, k_{+1}, k_{-1}, k_2, k_{+3}, and k_{-3}, are assumed to be functions of local pH.

We take this system of chemical equations and convert it into a set of ODEs using mass action kinetics, as described in Section 7.2. This gives the following system of equations:

$$\frac{\mathrm{d}[E]}{\mathrm{d}t} = -k_{+1}[E][S] + (k_{-1} + k_2)[C_S] - k_{+3}[E][I] + k_{-3}[C_I], \tag{7.8}$$

$$\frac{\mathrm{d}[S]}{\mathrm{d}t} = -k_{+1}[E][S] + k_{-1}[C_S], \tag{7.9}$$

$$\frac{\mathrm{d}[I]}{\mathrm{d}t} = -k_{+3}[E][I] + k_{-3}[C_I], \tag{7.10}$$

$$\frac{\mathrm{d}[C_S]}{\mathrm{d}t} = k_{+1}[E][S] - (k_{-1} + k_2)[C_S], \tag{7.11}$$

$$\frac{\mathrm{d}[C_I]}{\mathrm{d}t} = k_{+3}[E][I] - k_{-3}[C_I], \tag{7.12}$$

$$\frac{\mathrm{d}[P]}{\mathrm{d}t} = k_2[C_S], \tag{7.13}$$

where $[X]$ is the concentration of species X in Equations (7.6) and (7.7).

In order to simplify the computation and analysis we scale all reactant concentrations by the enzyme or substrate concentrations. We define the following dimensionless variables:

$$s = [S]/s_0,\ i = [I]/s_0,\ p = [P]/s_0,\ e = [E]/e_T,\ c_s = [C_S]/e_T, \text{ and } c_i = [C_I]/e_T,$$

where s_0 is the initial concentration of adhesion proteins, and $e_T = [E] + [C_S] + [C_I]$ is the total enzyme present, which is conserved. This gives the following system of

equations:

$$\frac{\mathrm{d}e}{\mathrm{d}t} = -k_{+1}s_0 es + \left(k_{-1} + k_2\right) c_s - k_{+3}s_0 ei + k_{-3}c_i \,, \tag{7.14}$$

$$\frac{\mathrm{d}s}{\mathrm{d}t} = -k_{+1}e_T es + k_{-1}\frac{e_T}{s_0}c_s \,, \tag{7.15}$$

$$\frac{\mathrm{d}i}{\mathrm{d}t} = -k_{+3}e_T ei + k_{-3}\frac{e_T}{s_0}c_i \,, \tag{7.16}$$

$$\frac{\mathrm{d}c_s}{\mathrm{d}t} = k_{+1}s_0 es - \left(k_{-1} + k_2\right) c_s \,, \tag{7.17}$$

$$\frac{\mathrm{d}c_i}{\mathrm{d}t} = k_{+3}s_0 ei - k_{-3}c_i \,, \tag{7.18}$$

$$\frac{\mathrm{d}p}{\mathrm{d}t} = k_2\frac{e_T}{s_0}c_s \,. \tag{7.19}$$

7.3.2 The pH gradient in the corneum

The local pH is the input for the ODE system for the cell, and depends on cell location. The pH gradient over the corneum was obtained from a graph in Ohman and Vahlquist [88] who collected data from human forearm, abdomen, and calf skin using sello-tape and cyanoacrylate resin stripping, shown as the point data in Figure 7.2. We fit a polynomial to the forearm, abdomen, and calf data using the sello-tape stripping data. The function fit for the pH gradient is as follows:

$$\mathrm{pH} = f_{\mathrm{pH}}(\xi) = 6.8482 - 0.3765\,\xi - 5.1663\,\xi^2 + 3.1792\,\xi^3 \,, \tag{7.20}$$

where $\xi \in [0, 1]$ is the height of the cell above the base of the corneum as a proportion of the expected corneum thickness, shown as the solid black line in Figure 7.2. The model was fit using multiple linear regression, with an R-squared value of $R^2 = 0.94$.

7.3.3 Rate parameters

Equations (7.14) to (7.19) require five rate parameters: three for the interaction between the enzyme and the corneodesmosomes; k_{+1}, k_{-1}, and k_2, and two for the interaction between the enzyme and LEKTI inhibitor; k_2 and k_{-3}. It is necessary to

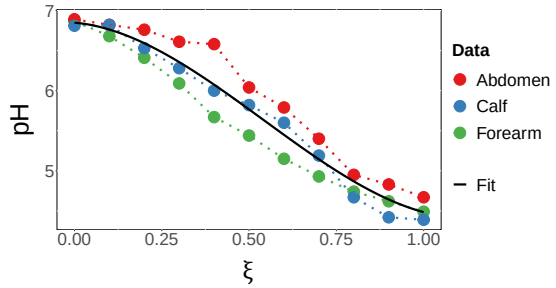

Figure 7.2: The fit for the pH to the data from Ohman and Vahlquist [88].

determine these parameter values from experimental data. Data for these processes is currently limited to *in vitro* experiments. A major assumption of this analysis is that this data is representative of the *in vivo* system. The data we use to estimate these parameters and their dependence on pH is given below.

KLK and corneodesmosome interaction

There are three rate parameters to determine for the KLK and corneodesmosome interaction given in Equation (7.6). The first two, k_{+1} and k_{-1}, are the association and dissociation rates for the formation of the complex, C_I. The last rate parameter, k_2, is the rate at which the corneodesmosome complex is degraded.

The data available in the literature for this reaction is from Caubet et al. [17], who record the degradation of corneodesmosin and desmoglein 1, two proteins in corneodesmosomes, in neutral and acidic pH solution over a two hour period of incubation with KLK5. As this was an *in vitro* experiment, there are several assumptions we make in using the results to parameterise the *in vivo* system. These include the assumption that the limited number of the corneodesmosome proteins that were studied are representative of all proteins in the complex, and extrapolation from a system where the relative concentrations of the proteins and the enzymes are probably not physiologically accurate.

No LEKTI inhibitor was present in the Caubet et al. [17] experiments and each

enzyme was tested separately, therefore our system of differential equations, from Equations (7.14) to (7.19), reduces to:

$$\frac{\mathrm{d}e}{\mathrm{d}t} = -k_{+1}s_0 es + \left(k_{-1} + k_2\right) c_s \,, \tag{7.21}$$

$$\frac{\mathrm{d}s}{\mathrm{d}t} = -k_{+1}e_T es + k_{-1}\frac{e_T}{s_0}c_s \,, \tag{7.22}$$

$$\frac{\mathrm{d}c_s}{\mathrm{d}t} = k_{+1}s_0 es - \left(k_{-1} + k_2\right) c_s \,, \tag{7.23}$$

$$\frac{\mathrm{d}p}{\mathrm{d}t} = k_2\frac{e_T}{s_0}c_s \,. \tag{7.24}$$

As the data has no information about c_s it is not possible to determine all rate parameters for this equation. Consequently, by making some assumptions about this interaction, we can instead determine a relationship between the parameters. In these experiments the KLK mass was 100 ng enzyme compared to 70 μg of the adhesive protein. Given the amount of adhesive protein is two orders of magnitude greater than the enzyme, we can assume that the rate of change in complex is negligible [60]. This is the quasi-steady state assumption from Briggs and Haldane [13]. Therefore we can assume the concentration of KLK5-CND compound is approximately constant, or:

$$\frac{\mathrm{d}c_s}{\mathrm{d}t} = 0, \tag{7.25}$$

and, from Equation (7.23), the amount of KLK and CND in compound is given by:

$$c_s = \frac{s_0}{K_M} es, \tag{7.26}$$

$$\text{where } K_M = \frac{k_{-1} + k_2}{k_{+1}}. \tag{7.27}$$

We know the the total amount of free enzyme and enzyme in complex is conserved, so $e + c_s = 1$ (with no inhibition). Substituting Equation (7.26) into this conservation equation, we get a formula for the amount of free enzyme, which we

can then use to find an equation for c_s in terms of s:

$$e = \frac{1}{1 + \frac{s_0}{K_M} s}, \tag{7.28}$$

$$c_s = \frac{s_0 s}{K_M + s_0 s}. \tag{7.29}$$

Substituting these formulae for c_s and e into Equation (7.22) produces the quasi-steady state equation for the degradation rate of the adhesive protein in terms of s [60, 87]:

$$\frac{\mathrm{d}s}{\mathrm{d}t} = -\frac{k_2 e_T s}{K_M + s_0 s}. \tag{7.30}$$

Solving this equation with initial condition $s(t = 0) = 1$, we get the following relationship between the proportion of remaining protein, s, and t:

$$K_M \log(s) + s_0 (s - 1) = -k_2 e_T t\,. \tag{7.31}$$

This equation can now be fitted to adhesion degradation data to determine K_M and k_2.

As mentioned above, Caubet et al. [17] determined the degradation over time of two adhesive proteins. The experiments were performed for pH values of 5.6 and 7.2, and the data can be seen in Figure 7.3a. Though the plots show a difference at the two pH values, the effect reverses depending on the corneodesmosome protein considered. The authors concluded there was little variation between the two pH results, so, given we do not discriminate between the two proteins in the model, we assume the same. Additionally, this data set is small and consequently it is not reliable for the calculation of fits with high confidence if separated by pH level. Consequently, for this reaction we assume the effect of pH is negligible.

We can use the Caubet et al. [17] data to determine K_M and k_2 using Equation (7.31). However, to maintain unit consistency with the rate parameter k_{+3} (Equation (7.33)), we need to first convert the weight to a Molarity. In order to convert concentrations to a molar quantity, we require the molecular weight of each

Unit	CDSN	DSC1	KLK5
Weight in grams [μg]	70	70	0.1
Molecular weight [kDa]	54	100	34
Weight in moles [pmol]	1,300	700	3
Concentration [μM]	18,600	10,000	41

Table 7.1: Conversion from weights to concentrations for the proteins and enzymes used in the Caubet et al. [17] paper. The experiments were run in volumes of 70 μL (email communication with M. Simon).

Parameter	Value
K_M [M]	4.60×10^{-5}
k_2 [hr^{-1}]	2.29×10^{3}
k_{+1} [$\text{M}^{-1}.\text{hr}^{-1}$]	4.97×10^{7}

Table 7.2: Fitted parameter values for the interaction between enzyme and adhesion protein.

protein and enzyme. Using molecular weights from Caubet et al. [17] we can calculate the molar quantities shown in Table 7.1. Concentrations are then determined by taking the molar weight and dividing by the volume for the experiment to give the values shown in Table 7.1.

The calculated fits are given in Table 7.2 and shown, with the data, in Figure 7.3a. These fits were determined using multiple linear regression (by dividing Equation (7.31) through by k_2), with an R-squared value of R^2 = 0.71. Though this is an acceptable value of R-squared, it is important to note that we found it was possible to get very different fits to produce similar R-squared values, and hence more data is required to have confidence in these parameter values. This is discussed further in Section 7.5.

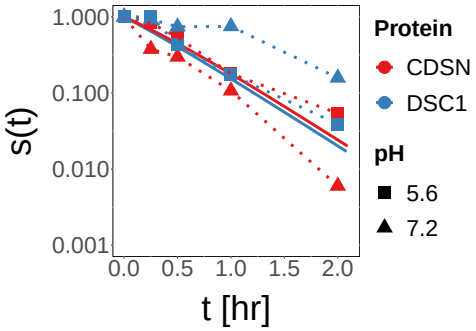

(a) Fit for K_M and k_2.

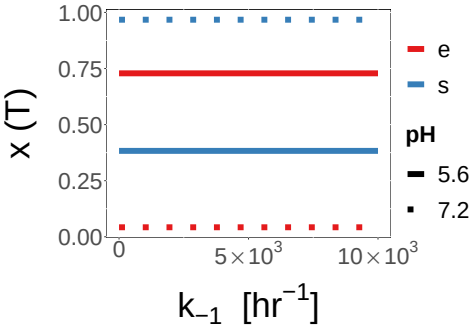

(b) Solution at $T = 50$ hours for varying k_{-1}

Figure 7.3: (a) The fits to the adhesion degradation data. The plot shows the degradation of two proteins at two pH levels. Dashed lines show the path of each experiment, and the solid lines show the fit to the data. Two lines are given as the fit is dependent on the initial protein concentration, which was different for the CDSN and DSC1 experiments. (b) The proportion of s and e, the amount of CND and free KLK5, after $T = 50$ hours for different values of k_{-1} showing that the variation with k_{-1} is negligible.

Two lines can be seen on the plot, one for each adhesion protein (CDSN or DSC1), as each of the adhesion proteins has a different initial concentration (s_0), and consequently, from Equation (7.31), the degradation curve will be different for each protein.

Given these values of K_M and k_2, we now need to determine the values of k_{+1} and k_{-1}. We have the following relationship between k_{+1} and k_{-1}, from Equation (7.27):

$$k_{+1} = \frac{1}{K_M}\left(k_{-1} + k_2\right). \tag{7.32}$$

Given that K_M is on the order of 10^{-5} and k_2 is on the order of 10^3, this makes k_{+1} approximately five to eight orders of magnitude greater than k_{-1}. Consequently, we assume that the value of k_{-1} is negligible and we approximate $k_{-1} = 0$. Solving the full ODE system for different values of k_{-1} at both acidic and neutral pH supports

this assumption. As can be seen in Figure 7.3b, the variation in $s(T)$ is less than 0.01% for either pH. Consequently, we get the the value for k_{+1} shown in Table 7.2.

KLK5 and LEKTI (inhibitor) interaction

Chemical Equation (7.7) has two rate parameters: k_{+3} and k_{-3}, the association and dissociation rates for the binding between KLK5 and the inhibitor LEKTI respectively. A study by Deraison et al. [22] determined association and dissociation constants (k_{+3} and k_{-3}) at different pH from *in vitro* experiments. As with the results above, the use of *in vitro* experimental data may not be an accurate representation of the *in vivo* system. One significant limitation is that results are for only one LEKTI fragment, while multiple are present in the epidermis. LEKTI fragments are small fragments of the LEKTI protein that is synthesised by the cell. It is the fragments that are released into extracellular space and interact with the KLKs [22, 32]. Though Deraison et al. [22] studied the inhibition effectiveness of several fragments, experiments in varying pH levels were only done for one of the fragments.

Fitting models to this data, shown in Figure 7.4, produces the following equations for k_{+3} and k_{-3} as functions of pH:

$$k_{+3} = f_{+3}(\mathrm{pH}) = (5.2\,\mathrm{pH} - 19.5) \times 10^7\ [\mathrm{M}^{-1}.\mathrm{hr}^{-1}], \tag{7.33}$$

$$k_{-3} = f_{-3}(\mathrm{pH}) = 2.3 \times 10^6\,\mathrm{e}^{-3.0\mathrm{pH}}\ [\mathrm{hr}^{-1}]. \tag{7.34}$$

These models were fit using linear regression, with R-squared values of $R^2 = 0.94$ and $R^2 = 0.9998$ for k_{+3} and k_{-3} respectively.

7.3.4 Concentrations of KLK, LEKTI, and CND

There is limited *in vivo* data for the concentrations of KLK, LEKTI, and CND in the corneum. The data and estimates we make for each reactant are detailed below.

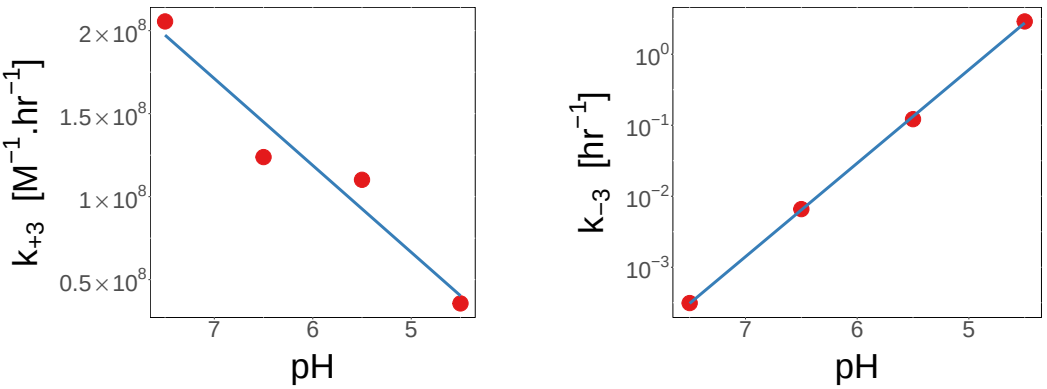

(a) Association rate parameter (k_{+3})

(b) Dissociation rate parameter (k_{-3})

Figure 7.4: Fits to the association and dissociation data for the KLK5-LEKTI interaction (blue line). Data (red dots) is taken from Deraison et al. [22].

KLK enzyme

Several studies have investigated the mass of KLK in epidermal tissue. The data is provided as a mass of free enzyme per mass of dry corneum tissue. Consequently, it does not account for enzyme in complex and provides no spatial component to the concentrations. It is necessary, for the purposes of the model, to convert these amounts to molar concentrations in extracellular space.

Komatsu et al. [66] measured levels of different KLK enzymes for healthy skin and skin with Netherton syndrome (NS). In healthy skin, the study detected a total enzyme amount of 30 ng.mg^{-1} dry weight. Of this, 19.1 ng.mg^{-1} was trypsin-like KLKs, 3.1 ng.mg^{-1} was KLK5. In order to convert this to a molar concentration we need two more pieces of information: the molecular weight of KLK5, and the volume of extracellular water per mg dry weight of stratum corneum tissue. The molecular weight of active KLK5 is 33 kDa [32], making 3.1 ng.mg^{-1} of KLK5 equivalent to 93.9 fmol.mg^{-1}. We can approximate the volume of extracellular water to dry tissue weight using the water content of the tissue and the volume ratio of cell to extracellular space in the corneum.

The water content of the corneum varies between deep and superficial tissue, ranging from 65–70% in the granular layers (and below) to 30–40% at the surface of the corneum [27]. Consequently, we estimate it at 50%, or 0.5 $g.g^{-1}$, making the water weight equal to the dry tissue weight. Given the density of water is 1 $mL.g^{-1}$, the volume of water in millilitres is equal to the weight of dry tissue in grams. However, this water content includes both the intracellular and extracellular water. In order to account for this, we estimate the ratio of intracellular to extracellular water by the volume ratio of the cell to extracellular space. We know the height of a corneocyte is around 300 nm [11], and it has been determined that the extracellular space between the cell sheets in the upper corneum is 44 nm [7]. Consequently, we estimate the volume of extracellular space, and consequently extracellular water, to be approximately 13% of the total volume. Therefore, our conversion from dry tissue weight to water volume in mL is 0.13 times the dry tissue weight in grams, making 93.9 $fmol.mg^{-1}$ KLK5 in dry tissue roughly equivalent to an enzyme concentration of 0.723 μM.

LEKTI inhibitor

LEKTI is synthesised by the cell as a large protein, which is then broken down into smaller fragments before release into the extracellular space [32]. Particular LEKTI fragments are better at inhibiting particular KLK enzymes. Fortugno et al. [32] measured inhibition effectiveness of different LEKTI fragments for different KLK enzymes, as well as their molar quantities in human epidermis. The key result for the purposes of this project was that the LEKTI fragments most effective at inhibiting KLK5 were present in the same molar quantities as KLK5. Consequently, we set $i_T = e_T$ in healthy epidermis.

Corneodesmosomes

The *in vivo* data on corneodesmosomes provides counts of associated proteins across the edges of cells. Igawa et al. [49] counted 16 proteins per μm on the peripherals of cells and 10 proteins per μm in the central regions of cells. In order to convert this into a concentration we need to determine the number of proteins per unit of extracellular volume. We approximate a cell as a rectangle of 30 μm width and 0.3 μm height [11] and use the definition of peripheral and central from Igawa et al. [49] where the peripheral regions extend a quarter of the way into the cell. As above, we know the extracellular space is 0.044 μm [7]. From this, we can estimate the concentration of proteins in the space between two stacked cells to be 1.6×10^5 proteins in 39.6 μm^3. This is equivalent to 4.0×10^{18} proteins.L^{-1}, or 6.6 μM. This value is a very rough estimation, but provides an idea of the order of magnitude of the protein concentration. We note this is only one order of magnitude greater than the enzyme concentration.

Initial conditions

We assume the enzyme and inhibitor start in complex (c_i), limited by whichever of the enzyme or inhibitor has a lower concentration. If there is more enzyme than inhibitor, any remaining enzyme is free (e), and consequently the enzyme-substrate complex (c_s) is always zero initially. Corneodesmosomes are at their maximum concentration initially ($s(t = 0) = 1$).

7.4 Results

In the previous section we have developed a system of ODEs (Equations (7.14) to (7.19)) for the degradation of adhesion proteins in the stratum corneum by enzymes, with an inhibitor, using enzyme kinetics methods. This system has five parameters: two which are related to the enzyme–inhibition reaction (Equations (7.33)

and (7.34)), and three which are related to the degradation of the corneodesmosome by the enzyme (Table 7.2). Each of these parameters change depending on the local pH of the cell, which varies over the corneum (Equation (7.20)).

In this section we analyse the dynamics of the ODE system external to the multicellular model. This allows us to interrogate the system parameters in more detail. We consider the system response at different pH, and to different reactant concentrations assuming a specified upwards velocity of the cell, determined using cell migration times and corneum thickness data.

7.4.1 Decreasing pH increases degradation of adhesion but does not match expected degradation rates

The first result we look at is the degradation of the substrate at varying levels of pH. The solutions over time of Equations (7.14) to (7.19)are shown in Figure 7.5. The first observation is the increased rate of degradation with decreasing pH. This is in support of the hypothesised system, as the high pH represents the activity at deep epidermis while low pH is the equivalent of superficial epidermis. This is not a surprising result, as the rate parameters for the inhibition reaction should free more enzyme from complex at lower pH. In Figure 7.4, at high pH (deep epidermis), the ratio of association to dissociation of inhibitor complex is on the order of magnitude of 10^{11}, while at low pH, this ratio on the order of 10^{7}. Consequently, we expect much more inhibitor complex at high pH, decreasing the amount of enzyme available to interact with the corneodesmosome.

A second observation from Figure 7.5 is the rate of degradation of the corneodesmosomes (s). We know the migration time of a cell through the corneum is around 20 days, and so would expect the degradation to occur at a similar time scale. The results show much faster time scales, closer to a day. We explore this in more detail below, by considering the degradation of a cell migrating through the pH gradient.

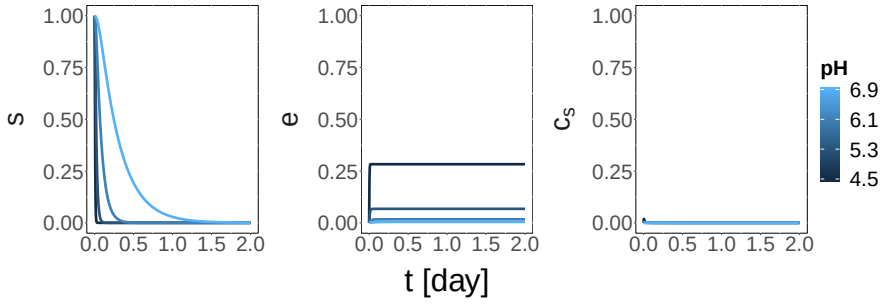

Figure 7.5: Results for the system (Equations (7.14) to (7.19)) at varying pH. Reactant concentrations are $e_T = i_T = 0.723$ μM and $s_0 = 6.6$ μM.

7.4.2 Solutions for a migrating cell highlight the effect of limited diffusion

In order to better understand this system, we can solve it for a cell migrating through the pH gradient. This provides a more realistic representation of the degradation of the adhesion proteins. From Chapter 2 (Section 2.4), we know the migration of the cell takes around 18.5–26.5 days in human epidermis. We assume that the cell velocity is approximately constant through the corneum, and estimate the migration time as 20 days. This gives us an approximate velocity, normalised by corneum thickness, of $v_\xi = 0.05$ day^{-1}.

Figure 7.6 shows the results for a cell migrating through the pH gradient over the expected 20 days migration time. As we saw in Figure 7.5, the substrate degrades too fast to see the effect of the pH gradient.

If we consider the spatial component mentioned earlier—the degradation of corneodesmosomes occurs initially on the horizontal surfaces of the cells—we can determine if the data matches the degradation time of these planar proteins. Igawa et al. [49] found that the proteins on the horizontal surface were essentially degraded at the third layer. If we assume that the corneum depth is 10–20 layers, we would therefore expect these proteins to be degraded around days 3–6. This expected

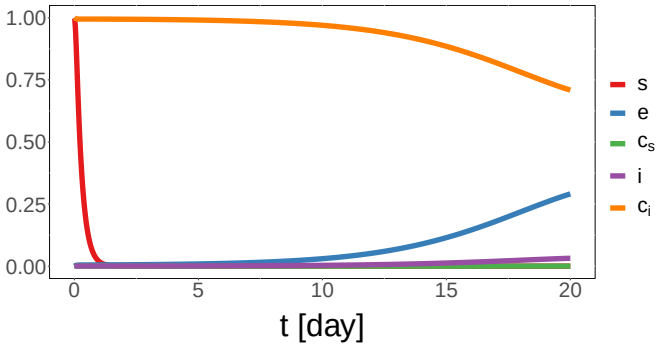

Figure 7.6: The solutions for a cell migrating through the pH gradient.

degradation is still slower than the results seen in the model, which indicates that either the rate parameters are wrong (k_{+1} and k_2), or that the mechanism is wrong.

We know there is a parameter regime in which the system produces the desired results, as can be seen in Figure 7.8. We also know more processes occur in the system than this one interaction, which is highly likely affecting the reaction. Igawa et al. [49] hypothesise that tight junctions at the peripheral of the cells act as a barrier to the enzyme-corneodesmosome interaction at peripheral sites, as shown in Figure 7.7. Our results indicate that, assuming rate parameters are at the right order of magnitude, this could have a significant effect on the degradation rate. Additionally, similar effects may even be occurring at the central regions of the cell, with the diffusion of the enzyme potentially limited by the intact corneodesmosomes themselves or the lipids also residing in the extracellular space. By limiting the diffusion of the enzyme, the system is no longer mixed and consequently the mass action model does not hold. In order to compensate for this limited diffusion effect, without incorporating new processes in the model, we instead propose the use of an *effective concentration of enzyme*. This will be explored in the next section.

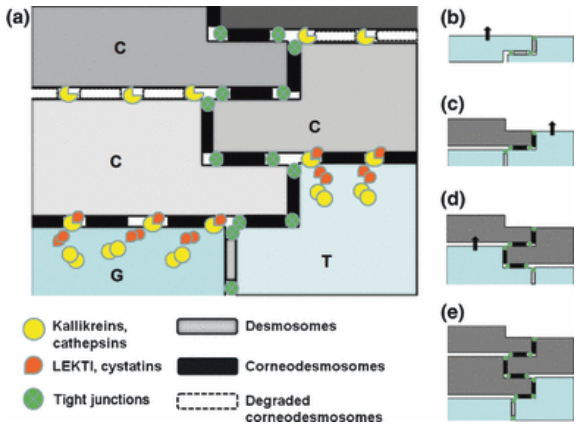

Figure 7.7: Tight junctions restricting the diffusion of enzymes. (Image reproduced with permission from Igawa, S. et al. en. *Experimental Dermatology* 20.1 (2011) [49]).

7.4.3 Incorporating an effective concentration of enzyme reproduces observed desquamation rates

We investigate changing the concentrations of the enzyme, and subsequently the inhibitor, or the substrate. We consider different orders of magnitude of the reactants, rounding our base concentrations: $s_0 = 10$ μM and $e_T = i_T = 1$ μM. The results for varying s_0 and e_T can be seen in Figure 7.8.

The first reactant we vary is the amount of KLK enzyme, or e_T. By decreasing e_T, we are effectively limiting the amount of enzyme available for degradation of corneodesmosomes, and consequently this is a way to simulate limited diffusion. As we vary e_T we also maintain $i_T = e_T$, as we want sufficient LEKTI to bind with the KLK.

From Equation (7.15), we can see that decreasing e_T directly affects the effective rate parameter for the degradation of s, which is given by $k_{+1}e_T$. However, it also will indirectly affect the amount of free enzyme. The equivalent decrease in i_T can significantly decrease the upper bound on i (given by i_T/s_0), and consequently could be expected to indirectly decrease the rate of the formation of inhibitor complex,

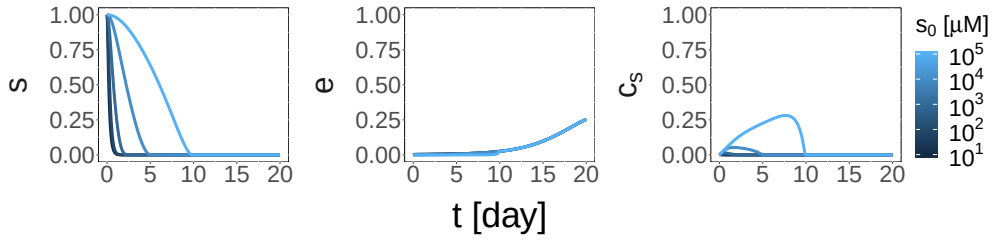

(a) Varying s_0 ($i_T = e_T = 1$ μM).

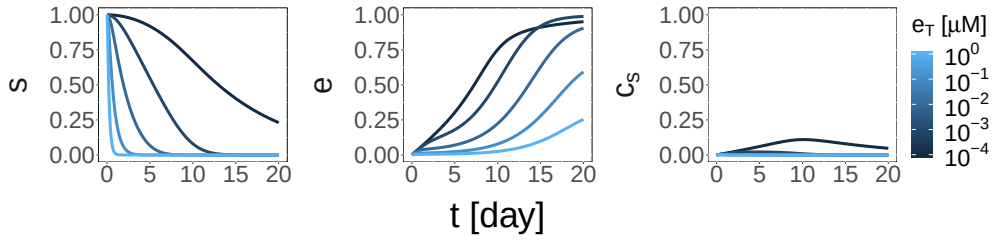

(b) Varying e_T ($i_T = e_T$ and $s_0 = 10$ μM).

Figure 7.8: The effect of varying concentrations on the system dynamics and rate of degradation of adhesion.

and increase e, as given by Equation (7.14).

The results for decreasing e_T can be seen in Figure 7.8b. As would be expected, decreasing the total amount of enzyme in the system increases the rate of degradation of the substrate. Also seen in Figure 7.8b, increasing e_T decreases the value of e. This is due to the indirect effect on e from the increasing upper bound on i, as mentioned above. However, this does not have as large an effect on the degradation of s as the increased effective rate parameter ($k_{+1}e_T$) with increased e_T.

We can better quantify the change in degradation by considering the point at which the substrate drops below 25%, or $s \leq 0.25$. These values are shown in Table 7.3. As can be seen in the table, by scaling the enzyme by a factor of 10^{-4} we can reproduce the expected rate of degradation of adhesion.

Next we consider the effect of increasing the amount of corneodesmosome, or s. This corresponds to varying the amount of adhesion between cells. Unlike decreasing e_T, it does not directly relate to a limited diffusion mechanism, but does affect rate

	Results				
Quantity	$e_T = 1.0$	$e_T = 10^{-1}$	$e_T = 10^{-2}$	$e_T = 10^{-3}$	$e_T = 10^{-4}$
$t(s \leq 0.25)$ [days]	0.4	1.1	3.2	7.8	19.3

Table 7.3: Quantifying the effect of degradation of adhesion with increasing e_T (and i_T). The units of e_T are μM, and $i_T = e_T$. Results are the time taken for the substrate (adhesion complex) to get below 25% of its initial concentration.

parameters.

Increasing s_0 increases the effective rate parameters for formation of the complexes, which are given by $k_{+1}s_0$ and $k_{+3}s_0$ in Equation (7.14). This would appear to decrease the amount of free enzyme available to degrade the complex. However, similarly to the effect of increasing i_T mentioned above, an increase in s_0 can significantly decrease the upper bound on i (given by i_T/s_0) and cause an increase in e, reversing the effect on the change of rate for the formation of inhibitor complex. Physically this makes sense, as changing the initial substrate concentration should not affect the rate of enzyme formation of complex with the inhibitor, just the amount of free enzyme.

The results for increasing s_0 are shown in Figure 7.8a. We see that, while there is substrate remaining and available for complex, essentially all the enzyme is in complex with either the substrate or the inhibitor, as expected. The main conclusion to draw from Figure 7.8a is that we are unable to prolong the degradation of the adhesion to 20 days; even with an increase in s by a factor of 10^4, full degradation occurs in half the time we expect it to.

Figure 7.8 shows a reduced concentration of e_T is able to reproduce the rates expected for the desquamation process. Additionally, the reduction of this parameter is a computationally efficient way to simulate the effect of limited diffusion, which would also reduce the available enzyme to bind to the substrate. In order to produce

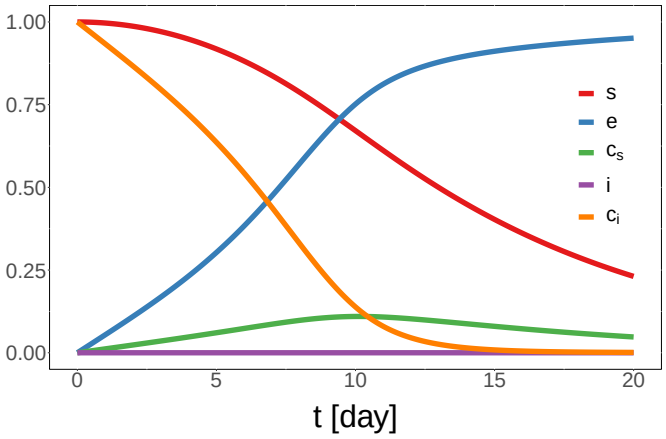

Figure 7.9: Model results incorporating an effective concentration of enzyme (e_T = 0.1 nM).

the expected results, we use an order of magnitude of e_T = 0.1 nM. An example of a full solution of the system with e_T = 0.1 nM, $i_T = e_T$, and s_0 = 10 μM is shown in Figure 7.9.

7.4.4 Modelling disease

We can use this model to investigate *Netherton Syndrome (NS)*, a disorder that mutates the gene for the LEKTI inhibitor. As detailed in Section 2.6.1, symptoms of NS include skin peeling, frequent skin infection, and temperature instability [66]. Presumably as a result of the reduced amount of inhibitor, KLK levels are elevated in NS patients. Komatsu et al. [66] recorded KLK levels in the NS patients between 157% to 486% that of healthy corneum.

We can consider the effect of reduced LEKTI inhibitor on the model by reducing the concentration, i_T. These results can be seen in Figure 7.10. As would be expected, decreasing the amount of inhibitor decreases the amount of enzyme in complex with the inhibitor, and consequently increases the degradation rate of the substrate. We can again quantify these results by comparing the time at which the substrate drops below 25%, and by determining the amount of free enzyme over the

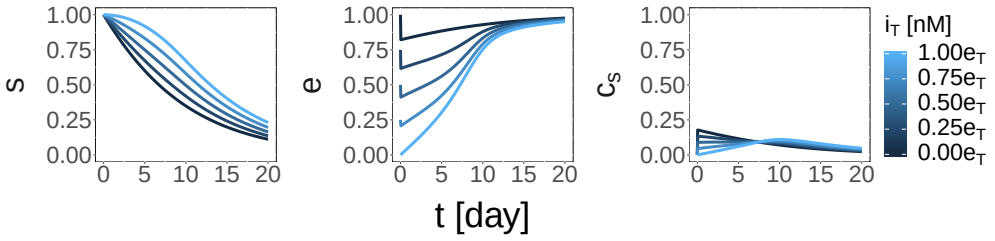

Figure 7.10: Varying i_T (e_T = 0.1 nM, s_0 = 10 μM).

	Results				
Quantity	$i_T = e_T$	$i_T = 0.75e_T$	$i_T = 0.5e_T$	$i_T = 0.25e_T$	$i_T = 0.0e_T$
$t(s \leq 0.25)$ [days]	19.3	17.9	16.3	14.8	13.0
$\int_0^{20} e \, \mathrm{d}t$ [days]	12.3	13.7	15.1	16.7	18.4

Table 7.4: Quantification of the results for diseased versus healthy system. The units of i_T are μN and e_T = 0.1 nM.

whole corneum for comparison to the data from Komatsu et al. [66]. These values are shown in Table 7.4.

As can be seen in Table 7.4, the worst case scenario would produce corneum with a reduced depth of 33% and 50% more free KLK. This is the smallest amount of extra KLK observed in NS patients in the data from Komatsu et al. [66], and therefore is likely underpredicting the effect of the reduced LEKTI. However, if we consider the results in Figure 7.8b, we can see that the proportion of free enzyme at lower total e_T concentrations is much higher than at high e_T concentrations. Consequently, if we were instead to compare the same integral ($\int_0^{20} e \, \mathrm{d}t$) with the original estimate of e_T = 1 μM, we get 1.2 days for $i_T = e_T$ compared to 5.4 days for $i_T = 0.75e_T$, which is an increase of 350% and much closer to the results seen experimentally. However, it is not possible to analyse the reduced depth at these concentrations as the substrate degrades too fast to produce these results.

These results tell us that, using the experimental values of enzyme concentration,

it only requires small reductions in the amount of inhibitor (around 25%) to reproduce the higher weights of enzymes seen in NS corneum experimentally. However, using the effective concentration of enzyme, we reduce the impact of the reduction of inhibitor. This is important when we consider the diseased system results in the multicellular system in Chapter 8.

7.5 Limitations of the model

As with many mathematical models of biological systems, the system is limited by computational feasibility and access to appropriate data. In order to model this system in a computationally efficient way, we have had to make several assumptions and ignore many processes occurring in the system. The most significant is the assumption of a well-mixed homogeneous system, which is an assumption of the mass action model. This, of course, does not reflect the physical system. Though it may be a valid assumption for the reaction between LEKTI and KLK, as we saw in the results the formation of the corneodesmosomes appears to have a significant effect on the degradation rate. A further improvement on this model would be to incorporate this spatial structure of the corneodesmosomes in a more sophisticated way. However, a model of this level would be infeasible to include in a multicellular model.

Another assumption is that the only effect of NS is a reduction in LEKTI available for binding with KLKs. As stated in Section 2.6.1, the disease's effect on subcellular dynamics on the system are likely to be much more complex. In particular, we assume that the pH gradient is not affected by the disease, either directly or indirectly. However, we note that our model assumes the pH affects only the KLK5 and LEKTI interaction and therefore, in the $i_T = 0$ case, the pH gradient would have no effect on the results. In the other cases, for example $i_T = 0.5e_T$, the effect of scaling the pH gradient in the corneum height dimension (equivalent to doubling

the velocity of the cell through the gradient) was found to be $\Delta s = 0.01$ after 20 days (results not shown). In comparison, the difference due to decreasing i_T to $i_T = 0.5e_T$ is $\Delta s = 0.07$.

A further limitation is access to appropriate data. Firstly, there is not sufficient data available to be fully confident in the parameters for the system. If we consider the fit in Figure 7.3a, the R-squared value is $R^2 \approx 0.7$. The R-squared value is defined as the variation in the dependent variable that can be be explained by the rate parameters. However, there are lots of combinations of parameters which result in similar R-squared values, which means the rate parameters are non-identifiable without further experimental data. Small differences in K_M and k_2 can also significantly impact the value of k_{+1}, and consequently the degradation rate of the adhesion proteins.

Secondly, the data for the rate parameters is from *in vitro*, rather than *in vivo*, experiments. Consequently, the values may not be accurate reflections of the *in vivo* parameters.

Thirdly, there is not sufficient data on the concentrations of each of the reactants in the system. The data that is available is limited to dried *ex vivo* tissue, which makes it necessary to make several approximations to convert this into a form useful for the model.

Though it is necessary to make these approximations and simplifications now, we have intended to create a system that can be built upon in the future. Future work will attempt to incorporate more of these complexities in the system, and the parameters are easily modified as more data becomes available.

7.6 Summary

In this chapter we have used enzyme kinetics to model the degradation of adhesion complexes by KLK enzymes in the stratum corneum for the purpose of better un-

derstanding desquamation. An additional molecule in this process is LEKTI, which inhibits the system, making the model one of competitive inhibition. Using data sourced from the literature, we are able to produce estimates for the different rate parameters and their variation with local pH, as well as concentrations of each of the reactants. Results show that the calculated rate parameters and concentrations produce a system that degrades much faster than has been observed in the desquamation process. This is either due to inaccurate rate parameters, or a mechanism that is not included in the model. Such a mechanism could be limited diffusion of the enzyme due to other molecules in intracellular space, particularly tight junctions. In order to account for such a mechanism without increasing the complexity of the model, it is possible to instead use an *effective concentration* of enzyme. We show that by doing this we are able to reproduce a system that reflects the desquamation rates observed in the corneum. However, when we model a diseased system with reduced inhibitor concentration, due to NS, we find that the reduced concentration of enzyme reduces the effect of the mutation on the enzyme concentration results over the corneum. Using the experimental enzyme concentration, the system is more effective at reproducing the elevated free enzyme concentrations recorded in NS patients.

8 A multiscale model of epidermal thickness regulation

In this chapter we incorporate the subcellular model developed in Chapter 7 into the multicellular model, replacing the exponential decay model for adhesion used in Chapter 6. The first section in this chapter describes the updated model. This includes the parameters for the multicellular model, the changes that need to be made to the subcellular system in order to produce an efficient realisation of the multiscale model, as well as the coupling of the two models. The second section contains results generated using the multiscale model. Firstly, we simulate a healthy tissue, the underlying subcellular model results, and the resulting tissue dynamics. We then investigate the effect of reduced inhibitor disorder on the tissue, and possible treatment hypotheses.

8.1 Building the multiscale model

In order to build the multiscale model we implement the DE system described in Chapter 7 into our multicellular model described in Chapter 4 and extended in Chapters 5 and 6. This DE system regulates the degradation of adhesion, replacing the exponential decay model described in Section 6.2.2, for the desquamation process

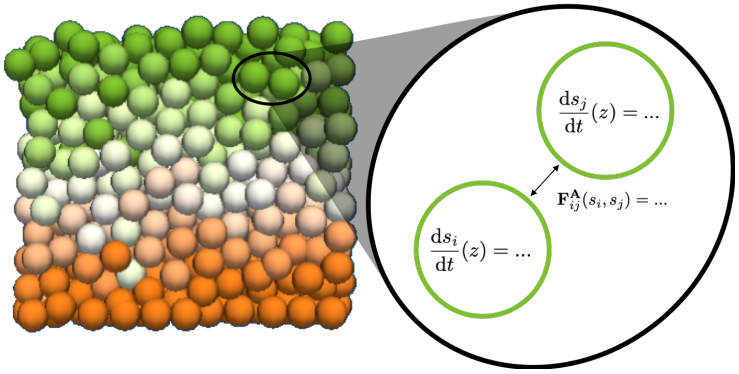

Figure 8.1: Coupling of the multicellular and subcellular models. Cells are coloured by their age.

described in Section 6.2.1. In order to efficiently incorporate the subcellular model described in Chapter 7 we make some changes in order to speed up computation. The first is a change to the parameters, both to account for the proliferation rate used and the smaller layer count modelled. The second is a change to the initial conditions to reduce large initial changes in reactants at lower inhibitor concentrations, and hence potential numerical issues. In this section we note the parameters used in the multicellular model, detail the adjusted rate parameters for the subcellular ODE system, the new initial conditions, and how we couple the subcellular and multicellular models together.

8.1.1 Multicellular model parameters

We begin with the multicellular model used for Chapter 6, with a couple of differences. We use the same cell cycle as in Chapter 5: $T_C \sim U\,(13, 17)$. The force-based desquamation is the same as in Chapter 6, however we replace the exponential function used for the degradation of adhesion with our new subcellular model. The burn-in period (30 days) and base cell-cell adhesion coefficient (10 μN) are the same as in Chapter 6. Ten realisations are run for each simulation.

8.1.2 Subcellular model rate parameter modifications

In order to produce a more computationally efficient system we have, as for previous chapters, decreased the number of cell layers in the tissue and increased the proliferation rate. Therefore the subcellular rate parameters (k_{+1}, k_2, k_{+3}, and k_{-3}) need to be adjusted to account for this. The fit for pH in Equation (7.20) is already normalised to the thickness of the stratum corneum and therefore this does not need to be changed.

In Chapter 7 we estimated the cell migration time as 20 days (480 hours) across the corneum. In multiscale system we use a much smaller migration time. The target corneum thickness is 8 CD (cell diameters) for the healthy system—approximately 10 cell layers in a tetrahedron style of packing. From previous results in Section 5.3.4, we know that the upwards velocity of the cells in the multicellular system is v_z = 0.05 CD.hr^{-1}. This gives a migration time of 160 hours and a velocity normalised by corneum thickness of v_ξ = 0.00625 hr^{-1}. Consequently, to change from a transit time of 20 days to 160 hours, we scale all rate parameters by 3. This gives the rate parameters for the enzyme-substrate reaction shown in Table 8.1, and the following equations for the enzyme-inhibitor reaction:

$$k_{+3} = g_{+3}(\text{pH}) = (15.6\text{pH} - 58.5) \times 10^7 \ [\text{M}^{-1}.\text{hr}^{-1}], \tag{8.1}$$

$$k_{-3} = g_{-3}(\text{pH}) = 6.9 \times 10^6 \, \text{e}^{-3.0\text{pH}} \ [\text{hr}^{-1}]. \tag{8.2}$$

Additionally, for a corneum thickness of 8 CD, the normalised corneum thickness parameter ξ is defined as:

$$\xi = g_\xi(z) = \frac{1}{8}(z - 4), \tag{8.3}$$

where z = 4 CD is the cell height we define to be the start of the corneum. In Chapter 6 we defined the start of the corneum using the cell age (as the degradation was also parameterised by cell age). Here, as the degradation depends on the pH, which depends on the cell height, it is sensible to instead define the start of the corneum using a minimum height.

Parameter	Value
Expected v_ξ [hr^{-1}]	6.25×10^{-3}
k_{+1} [$\text{M}^{-1}.\text{hr}^{-1}$]	1.49×10^{8}
k_2 [hr^{-1}]	6.87×10^{3}

Table 8.1: New rate parameters for the multicellular model.

Figure 8.2a shows the behaviour of the subcellular system for the adjusted system assuming an upwards cell velocity of $v_\xi = 0.0065$ hr^{-1}. Figure 8.2b shows that the solution as a function of the dimensionless ξ (normalised corneum thickness) parameter is the same for the new system as the original parameters from Chapter 7.

In Figure 8.2a, we can see $s(\xi = 1) = 0.23$. This is not necessarily the concentration of s at which desquamation will occur. In Chapter 7, concentrations were considered purely in terms of orders of magnitude, and the system was not controlled for the level of adhesion expected at the point of removal. Though we expect this is slightly higher than desquamation adhesion, given the results seen in Chapter 6 (Figure 6.7a), this difference is not significant, and should cause only small quantitative changes to results.

8.1.3 Initial conditions

In Chapter 7 we assumed all enzyme was initially in complex with the inhibitor. If there was less inhibitor than enzyme, we assumed the remaining enzyme was free enzyme (not in complex with the substrate). As can be seen in Figures 7.10 and 8.2c, when there is less enzyme than inhibitor, particular when $i_T = 0$, there is a steep drop initially in the free enzyme. This is a stiff system and the solution therefore requires very small time steps to solve and has the potential to cause numerical issues. Consequently, we instead assume that any enzyme that is not complex with the inhibitor is in an instantaneous quasi-equilibrium with the substrate-enzyme

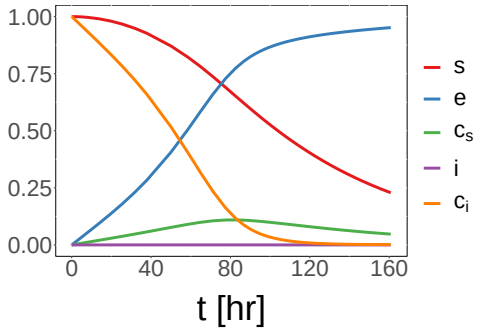

(a) Adjusted system solved for a moving cell with velocity $v = 0.01$ hr^{-1}.

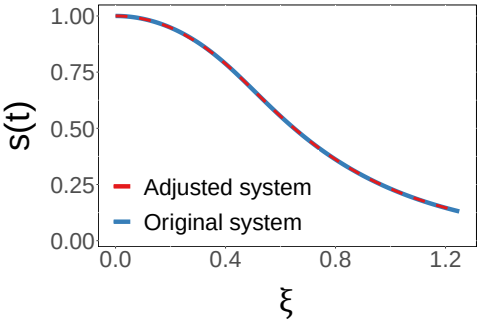

(b) Comparison of the Chapter 7 and new parameter systems normalised for the expected corneum thickness for each system.

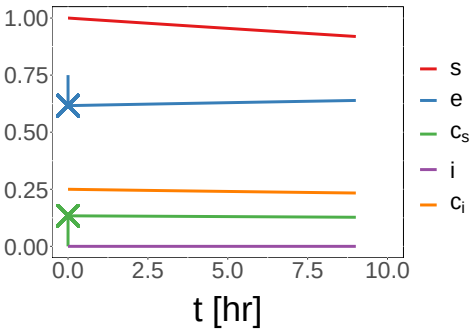

(c) System solution with new initial conditions indicated by '×'s.

Figure 8.2: The new parameter system results. (a) Subcellular system solution for a moving cell with the new parameters and a cell velocity of $v = 0.0065$ hr^{-1}. (b) A comparison of the new parameters system with the original system from Chapter 7, shown over the normalised corneum thickness, showing that the new system is just a scaled version of the old system. Bottom: subcellular system solution for a moving cell with $i_t = 0.25e_t$ as in Section 7.4.4. The solutions use the initial conditions described in Chapter 7, and the '×' indicate the new initial conditions for e and c_s. All other initial conditions remain the same.

complex.

In order to calculate what the equilibrium state would be we first assume all inhibitor is in complex with the enzyme. For the remaining enzyme, we take the differential equation for the enzyme in the enzyme-substrate reaction, Equation (7.21), and assume it is approximately equal to zero. Given we are estimating the dynamics instantaneously upon the release of these reactants, we set $s = 1$. This gives the following relationship between e and c_s:

$$-k_{+1}s_0e + (k_{-1} + k_2)c_s = 0\,. \tag{8.4}$$

We have $k_{-1} = 0$ and, additionally, $e + c_s + c_i = 1$. Therefore the initial conditions become:

$$e(t = 0) = e^* = \frac{k_2}{k_{+1}s_0 + k_2}\left(1 - \frac{i_T}{e_T}\right), \tag{8.5}$$

$$c_s(t = 0) = 1 - e^* - \frac{i_t}{e_t}\,, \tag{8.6}$$

$$c_i(t = 0) = \frac{i_T}{e_T}\,, \tag{8.7}$$

with $s(t = 0) = 1$ and $i(t = 0) = 0$. Parameters i_T and e_T are the concentration of inhibitor and enzyme respectively, with $i_T \leq e_T$. The results using the previous initial condition, along with crosses ('×'s) indicating the new initial condition, are shown in Figure 8.2c.

8.1.4 Linking the ODE system to the multicellular model

The subcellular degradation model is solved for each cell in the system for each time step. The only exclusion is the first few layers, where $z < h$ for some specified h (here $h = 4$), of cells, which are assumed to be in the lower layers of the epidermis, where we set $\mathrm{d}e/\mathrm{d}t = 0$ and hence $e = 0$. The cell location is taken from the multicellular model to determine pH, and consequently the rate parameters. The output from the cell into the multicellular system is the current proportion of s, or adhesion proteins, remaining.

The multicellular model then needs to relate the proportion of adhesion proteins to the cell-cell adhesion function. The proportional loss of the proteins is assumed to be directly proportional to the loss of adhesion, as these proteins are the cause of the cell-cell adhesion. In order to determine the adhesion between two cells we use the mean of the two protein concentrations. The use of the mean is an approximation of the fact that the reaction is occurring between the cells in extracellular space. It would be expected, therefore, that the adhesion between the two cells would be related to the length of time the enzymes from both of the cells have been in the extracellular space and interacting with the adhesion proteins between the two cells.

The coupling and solution of the ODE model follows Algorithm 1.

8.2 Results

Using the multiscale model described above, we can determine the steady state thickness, and the levels of each reactant, for healthy and diseased skin. Additionally, we consider a situation in which we can treat only a proportion of the stem cells. The results for each of these systems are detailed below.

For each result, as in Chapter 6, we present the mean thickness of the tissue as an average over 10 realisations. This is due to the stochasticity in the cell cycle adding stochasticity to the system. The results plotted for the reactants are taken from the end time point of a single realisation.

8.2.1 Model results for healthy function

The first results we show are for the healthy system, in which there are equal concentrations of enzyme and inhibitor. The levels of adhesion protein, s, are shown in an image of the simulation output in Figure 8.3a, and in a video at `https://youtu.be/VsFxSxSP9n4`. In this figure we see that the adhesion level appears to degrade homogeneously as cells move up through the tissue. Secondly, we

Algorithm 1: Linking subcellular model to cell-cell adhesion in multicellular model

for *each multicellular model time step* **do**
  for *every cell* **do**
    Determine the parameters:
      1. Height in corneum from cell location, $\xi = g_\xi(z)$, from Equation (8.3),
      2. $\text{pH} = f_{\text{pH}}(\xi)$ using Equation (7.20),
      3. $k_{+3} = g_{+3}(\text{pH})$ and $k_{-3} = g_{-3}(\text{pH})$ using Equations (8.1) and (8.2),
      4. k_{+1} and k_2 from Table 8.1.

    Solve Equations (7.14) to (7.19) using CVODE to next time step,
    Store s for the cell.
  end
  for *every cell pair* **do**
    Determine mean s for the two interacting cells,
    Scale the adhesion coefficient in the adhesion function (Equation (4.5)) between the two cells according to:

$$\alpha_{ij} = \frac{1}{2}(s_i + s_j)\alpha_0, \tag{8.8}$$

    where α_{ij} is the adhesion coefficient between cells i and j, and α_0 is the normal cell-cell adhesion coefficient.
  end
end

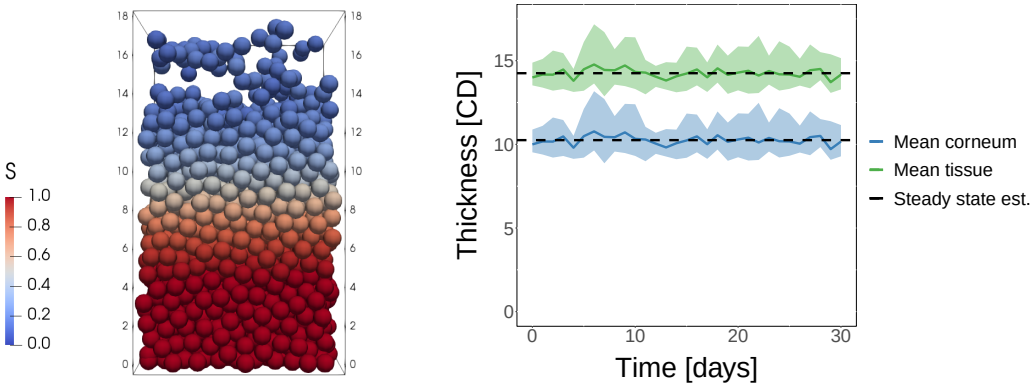

(a) Simulation output

(b) Time series of tissue thickness

Figure 8.3: Tissue structure and thickness for the healthy system (i_T = e_T). (a) Output from one realisation of the system showing the levels of adhesion protein s in each cell. (b) The thickness of tissue and the corneum. The ribbons indicate the variation (minimum and maximum) over the simulations, and the solid lines show the mean. The green line and ribbon are for the total tissue thickness. The blue line and ribbon is the corneum, which is 4 CD less than the tissue thickness. The black dashed lines show the estimated steady state thickness, calculated as the mean over time.

see seven layers of cells before the protein begins to visibly degrade, which is higher than the defined beginning of the corneum, however we know from Figure 8.2a that the initial degradation of s is slower.

At the top of the tissue, cells detach in clumps, when the adhesion protein appears to have dropped to less than s = 0.2. This appears to match the reduced number of corneum layers we used to calculate the reduced velocity and parameters for the system in Section 8.1.2.

Figure 8.3b shows the mean thickness of the system over time and the estimated steady state thickness of the tissue and the corneum. We can see that this new system is able to maintain a steady state thickness, similarly to the system in Chapter 6. The steady state tissue and corneum thickness in Figure 8.3b is 14.3 CD and

10.3 CD respectively—slightly higher than the expected system. In this chapter we are interested in corneum thickness. The target thickness for the corneum was 8 CD—roughly 2 CD below the results we are seeing. This appears to be due to the high variation in height of the cells at the top of the tissue (as discussed in Section 6.3.1) and the requirement of a separation distance of 0.7 CD. This can be seen in Figure 8.3a, where the cells at the top of tissue are seen to be 2–3 CD (note this varies over time) from the layer below, but have still not been removed as there is a line of connection to the tissue. Additionally, as we mentioned above, $s(\xi = 1)$ (which is equivalent to $s(z = 12)$) is slightly higher than we expect is needed for desquamation, as seen in the results from Chapter 6 (Figure 6.7a).

The values of the reactants over tissue thickness for one realisation, at $t = 30$ days are shown in Figure 8.4a. The point data shows the multicellular simulation values, while the lines indicate the expected values as shown in Figure 8.2a. Note i is given as i_T/s_0 and therefore has a maximum value of 10^{-5} when $i_T = e_T = 0.1$ nM. This is shown in the inset in the figure. Cells at the top of the tissue have a median substrate level of $s = 0.18$. If we consider the system as a tetrahedron, this is close to what is expected to be required to break the 3 cell-cell bonds to the lower cell layer for removal. Given that the removal force is half the maximum adhesion force, it would be expected that s would need to drop to $s \approx 0.17$ for desquamation. Note, however, in reality the cell configuration is highly random at the top of the tissue (result not shown) and, additionally, cells can 'drag along' cells below them when they are pulled from the top of the tissue, as seen in Figure 8.3a. Therefore this close match to the expected value should not be considered proof that the simulation matches the idealised system. Figure 8.4a also shows little variation in the reactant concentrations in cells at any particular height—the mean range in s over 0.1 CD intervals in z is 3.3%—as we could see see in Figure 8.3a, and a good match to the expected concentrations.

Given we know the tissue thickness and cell cycle length, we can calculate λ for

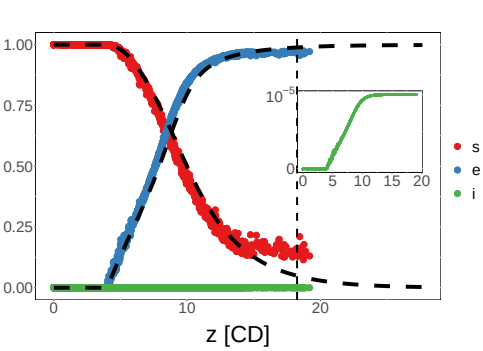

(a) Reactants level

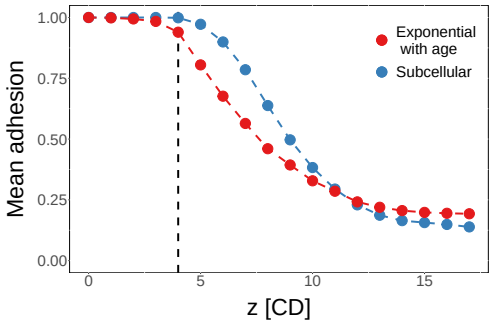

(b) Comparison with equivalent exponential model

Figure 8.4: Healthy tissue subcellular model results. (a) Reactant levels for each cell at one time point in one simulation. The vertical dashed line shows the steady state height, and the other dashed black curves show the expected solution of the subcellular model given the expected vertical velocity. (b) A comparison of the s level with the adhesion level using the equivalent exponential model calculated from the cell age data. The dashed line indicates the height at which the gradient begins solving in the subcellular model.

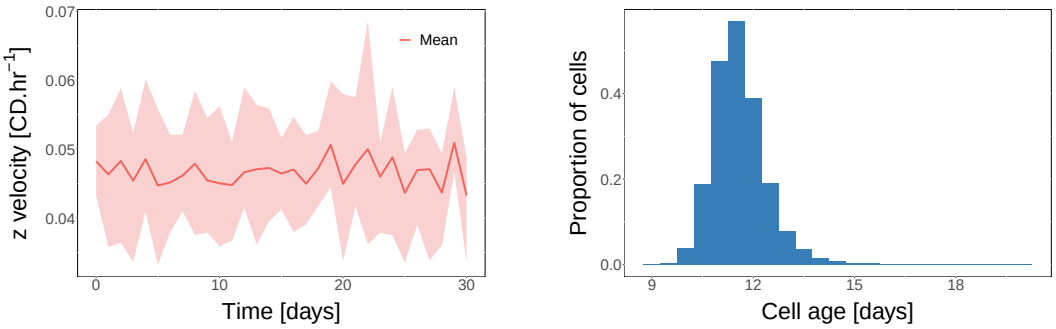

(a) Vertical velocity

(b) Turnover time

Figure 8.5: Healthy tissue dynamics. (a) The average vertical velocity over time. The ribbon indicates the range seen across all simulations, and the line is the mean of the simulations. The velocity is calculated based on cells in the main tissue and does not include stem cells or cells that are experience the desquamation force. (b) The age at which cells are removed, also known as the turnover time.

the equivalent exponential degradation model in Chapter 6 using Equation (6.6). The equivalent rate parameter is $\lambda = 8.4 \times 10^{-3}$ hr^{-1}. Figure 8.4b shows the adhesion levels of the cells using the equivalent exponential system, based on the cell age data from the multiscale model. The dashed line indicates the onset of the corneum in the multiscale model. As the exponential model is based on age, some cells in this model begin to degrade before this point, seen as the drop in adhesion at $z = 4$ CD in the figure. However the median age at $z = 4$ (defined as $z \in [3.5, 4.5)$) is 81.4 hours and therefore the starting point of the corneum is both models is approximately the same. We can see that the exponential model does provide a reasonable substitute for the full model, as the critical region of the model is when $\xi < 0.25$, and the exponential model and subcellular model are very close in this region.

The final aspect of the healthy system we will discuss are the dynamics. Specifically, the cell turnover time, and the velocity. These are shown in Figure 8.5.

The mean cell velocity, calculated from the time series data shown in Figure 8.5a,

is v_z = 0.047 CD.hr^{-1}. These results exclude stem cells and cells at the top of the tissue, as these values are much higher than in the main tissue, and therefore the mean is not representative of the main bulk of the tissue. This is close to the expected velocity (v_z = 0.05) based on the results in Section 5.3.4 and also based on the cell cycle time and expected layer thickness in the tissue (0.8 CD).

Figure 8.5a also shows a high amount of noise between the simulations. The reason for this noise is twofold. Firstly, there is noise is due to proliferation events, which cause increased velocities in local cells, as discussed in Section 5.3.1. Secondly, there is noise due to the use of the removal force. Though we have excluded the data from cells at the top of the tissue in the Figure, other cells will be affected by these forces. In some cases cells remain attached to the top cells and are consequently pulled upwards at high velocities (due to the force) before detaching from the tissue and being removed.

The cell turnover times are shown in Figure 8.5b. As can be seen in the plot, the median cell age at death is 11.5 days, or 276 hours. Given we know the median age of cells at entry to the corneum is 81 hours, turnover time in the corneum is 196 hours. It could be expected that the corneum turnover time should be close to 219 hours, given a thickness of 10.3 CD and a velocity of v_z = 0.047 CD.hr^{-1}. However, as noted above, this velocity does not include cells experiencing the removal force. The average velocity of cells experiencing the removal force is 0.31 CD.hr^{-1}, which accounts for the lower turnover time.

We have shown that the multiscale model is able to reproduce a system that maintains a steady state thickness. This system can be approximated by the exponential degradation model used in Chapter 6, however the inclusion of the subcellular system provides a higher level of understanding of how the tissue is maintaining its thickness. We have also seen that the use of the removal force, though necessary for the implementation of the model, does have a small impact on the results seen here.

8.2.2 Tissue thickness and inhibitor concentration have a linear relationship in diseased tissue

Similar to Chapter 6, we now consider the response of the system to reduced inhibitor. Such a reduction in LEKTI is a characteristic of Netherton Syndrome (NS), as described in Section 2.6.1. In Section 7.4.4 we considered the effect of the disorder on the reactants. In this chapter, we will consider how it affects the corneum thickness and tissue dynamics.

Figure 8.6a shows the simulation output for the system with no inhibitor present. Comparing this to Figure 8.3a, there does not seem to be any obvious difference in the structure of the systems except for the difference in thickness. Figures 8.6b and 8.6c show the mean thickness over time for different levels of inhibitor and the calculated steady states respectively. As would be expected, reducing the inhibitor decreases corneum thickness. This is because a reduced level of inhibitor increases the amount of enzyme available to degrade the adhesion proteins, resulting in earlier desquamation. We can see this in Figure 8.7, where decreasing concentrations of inhibitor increases the amount of free enzyme e, and this increases the degradation rate of the adhesion protein s.

Figure 8.6c also shows that corneum thickness is linearly dependent on the concentration of inhibitor present in the system. When there is no inhibitor present the corneum thickness decreases by 24% (to 7.8 CD). However, it is important to note, in Section 7.4.4 we determined that the use of an effective enzyme concentration decreased the effect of the decrease in inhibitor. Therefore, these results are considered to be a lower bound for the effect of the decreased level inhibitor on tissue thickness.

We can also look at the change in the vertical velocity and turnover time. Changes to the inhibitor concentration should have no effect on the proliferation, and so we would not expect the velocity of the cells to change. Figure 8.8a shows

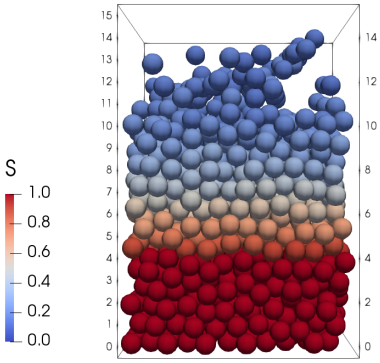

(a) Simulation output ($i_T = 0$)

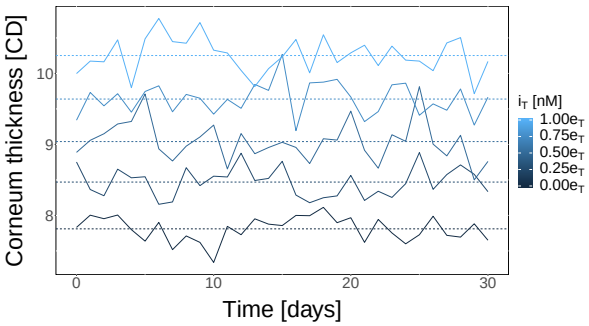

(b) Corneum thickness

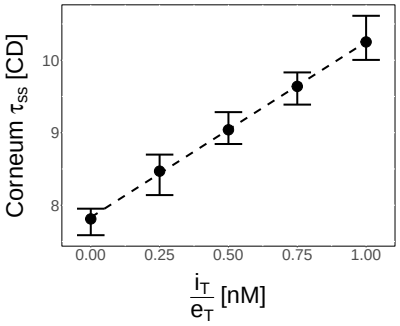

(c) Steady state estimate with fit

Figure 8.6: Tissue structure and thickness results for different amounts of inhibitor. (a) Simulation output from one simulation at one time point, showing the level of adhesion protein s in each cell. (b) The mean tissue thickness for different amounts of inhibitor, as a fraction of the enzyme concentration. Solid lines show the variation in the mean over time, and the dotted line shows the mean over all time steps. (c) The steady state thickness values, as shown by the dotted line in (b). The dashed line is a linear fit to the points and the error bars show the range over the 10 realisations.

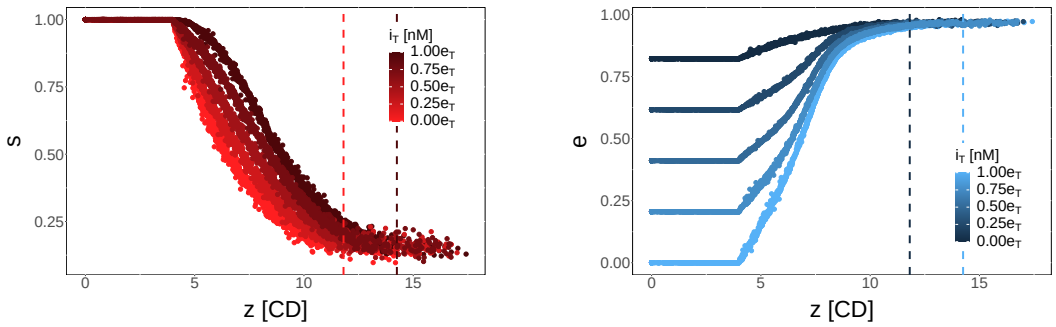

Figure 8.7: Diseased tissue s and e levels with different levels of inhibitor. The dashed vertical lines indicate the steady state height for the $i_T = 0$ and $i_T = e_T$ cases. The data is taken from the final time point of one simulation for each inhibitor concentration.

there is no evidence to reject the hypothesis that the velocity stays constant—the difference in mean velocity between the systems is 2.1%. The Figure also shows high variation in the velocity. As in Section 5.3.1, velocities are calculated from the instantaneous forces experienced by each cell. Additionally, this data includes every (except stem or top) cell in every simulation across all output times.

We expect turnover time to increase with increasing corneum thickness, and hence increasing inhibitor concentration. Figure 8.8b shows, similarly to corneum thickness, the turnover time is proportional to the concentration of the inhibitor. Note, the plot shows the median, range, and quartiles, rather than the mean and range, to show that the majority of cell turnover times are within a smaller band than the range would imply.

Given there is negligible difference in velocity, we could expect the relationship between turnover time and tissue thickness to be $\tau_{\text{ss}} = \bar{v}_z T_T - 4$, where $\bar{v}_z = 1.13$ CD.day^{-1} is the mean z velocity, T_T is the turnover time, and $z = 4$ CD is the start of the corneum. Figure 8.8c shows that the turnover time and tissue thickness are linearly dependent. However, the relationship is found to be:

$$\tau_{\text{ss}} = 1.04 T_T - 1.68. \tag{8.9}$$

There are three factors that are likely to contribute to this discrepency. Firstly, the calculated turnover time is not identical to the average age at the determined tissue height. This is because tissue height is determined by the mean height of the top layer of cells, which differs slightly from the mean height at which cells are lost (after they have sufficiently detached from the tissue). Secondly, the velocity is calculated using only 'normal cells'—that is cells which are not stem or top of tissue cells. This is because the forces on the top cells (and the stem cells), are much stronger and therefore including these cells is not a good representation of the bulk tissue velocity. Consequently, the period of time in which cells are a top cell, and consequently moving at higher velocities than the average, slightly affects this result. Thirdly, there are only 10 data points (simulations) for each steady state height calculated and so stochasticity in the system will have an effect.

These results showed the expected qualitative effect of decreasing the inhibitor. We saw that there was a linear relationship between inhibitor concentration and tissue thickness. With the lowest inhibitor concentration, the corneum thickness decreased by 20%, from 10.3 CD to 7.8 CD. Though this value is significant, due to the results found in Section 7.4.4, we expect this to be a lower bound for the thickness reduction in diseased tissue.

8.2.3 Potential treatment efficacy

A multiscale multicellular model is well suited for investigating heterogeneous systems. If we consider the system above for diseased tissue, we could hypothesise that a treatment to restore the healthy system would be to increase the level of inhibitor in the cells. The efficacy of this treatment can be seen above in Figure 8.6c where results show a linear relationship between the inhibitor concentration in the cells and the tissue thickness. However, one could also envisage a scenario in which such a treatment did not have 100% cell uptake, instead treating only a proportion of stem cells and leaving the remainder diseased. This is the scenario we investigate

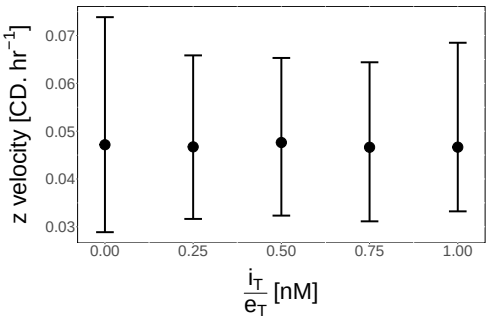

(a) Vertical velocity

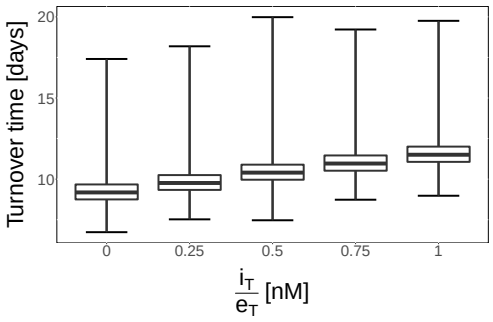

(b) Turnover time

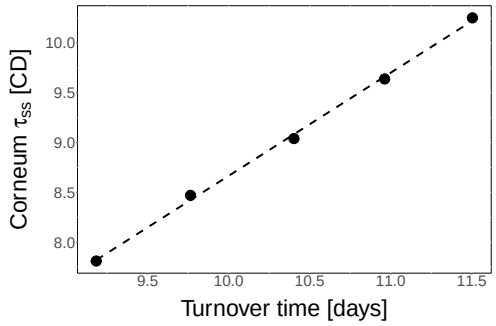

(c) Height as a function of turnover time

Figure 8.8: Diseased tissue results. (a) The mean vertical cell velocity for different levels of inhibitor, errors bars shown the minimum and maximum. (b) The cell turnover time. The box shows the median and 1st and 3rd quartiles, and the error bars show the minimum and maximum values. (c) The steady state corneum thickness plotted against cell turnover time, with the dashed line showing a linear fit to the points.

here.

We assume that the level of inhibitor in any cell is inherited from its parent stem cell and assign a level of inhibitor to each stem cell. The allocation of the diseased and healthy cells in random, so there is no spatial dependency. We set $i_T = 0$ for the diseased cells and $i_T = e_T$ for the healthy cells. Note there are 100 stem cells in the system, so the percentage of cells shown in plots is equivalent to the cell count.

Figure 8.9a shows the reactant levels of all the cells for one time point in a simulation with half the stem cells diseased and the other half treated. As would be expected, half the cells (points) follow the diseased path and the other half the healthy path. Figures 8.9b and 8.9c are a simulation snapshot with cells coloured by the s and e levels. Videos of one simulation showing s and e can also be found at `https://youtu.be/j25vwgZsJ18` and `https://youtu.be/ge0RxeBARQQ`. The diseased cells can be identified as the terracotta (red-brown) cells when $z < 4$ CD in Figure 8.9c, and the healthy cells are blue. This shows their initial conditions which are assigned at birth.

The plots and simulation snapshots in Section 8.2.3 show that the diseased cells are not lost before the healthy ones, as might be expected given their increased adhesion degradation rate. As cells tend to be removed in clumps the diseased cells are held longer than expected in the tissue, or in the clumps, by the healthy cells.

Figure 8.10a shows the thickness of the tissue with different counts of diseased cells. As can be seen in the figure, increasing the number of healthy stem cells has a non-linear effect on the corneum thickness. Here, we have fitted a quadratic curve to the thickness. Consequently, in comparison to the results in Figure 8.6c, we can see that better outcomes are seen if only a proportion of cells are treated to recover full inhibitor concentration, compared to small increases to the concentration of inhibitor in all the cells.

Lastly, we consider the system dynamics: cell velocity and turnover times. These are shown in Figures 8.10b and 8.10c respectively. As expected, these results are

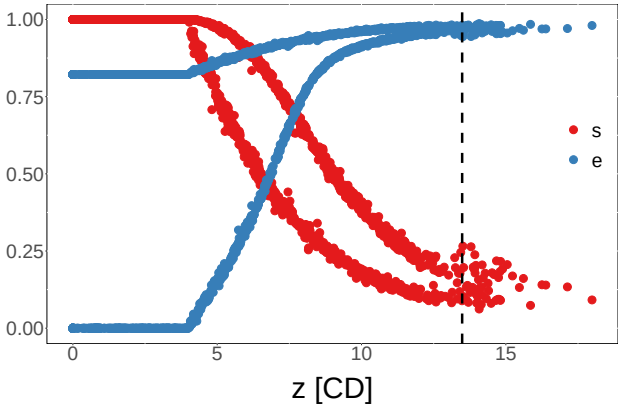

(a) Reactant levels

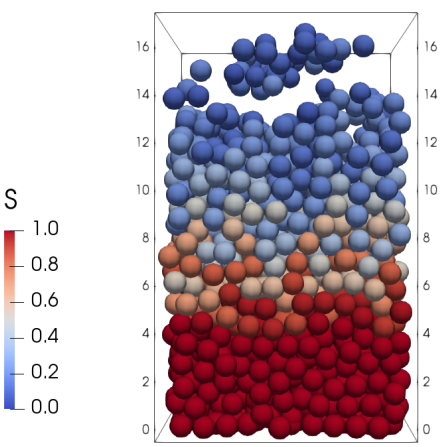

(b) Adhesive protein levels

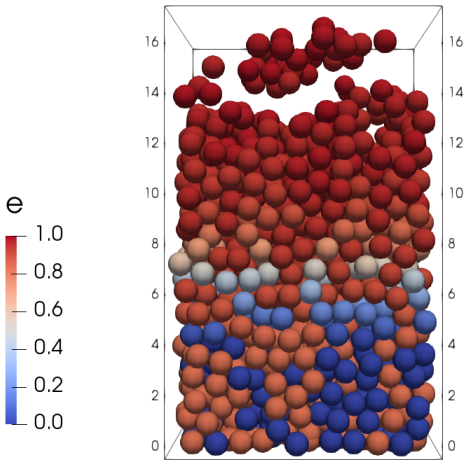

(c) Enzyme levels

Figure 8.9: The s and e levels for a system with 50% diseased and 50% healthy stem cells. (a) Reactant levels of each cell at the final time point for one simulation. The vertical dashed line shows the steady state height of the tissue. (b) Simulation snapshot showing the level of s (left) and e (right) for each cell.

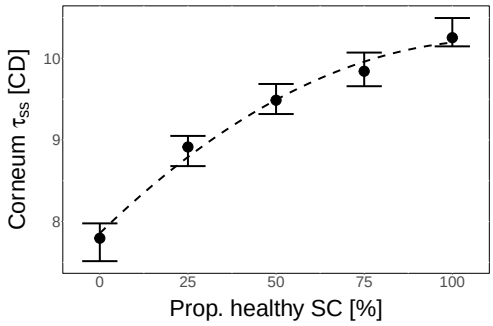

(a) Steady state thickness

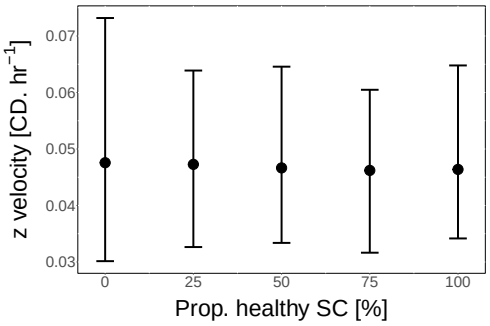

(b) Velocity

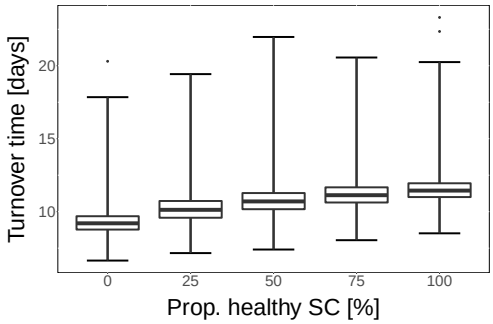

(c) Turnover time

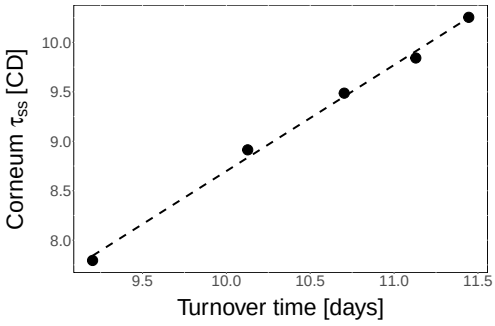

(d) Height as a function of turnover time

Figure 8.10: Tissue thickness and dynamics for varying proportions of healthy to diseased cells. (a) The steady state tissue thickness varies over the proportion of healthy cells. The dotted line shows a quadratic fit to the data and the error bars show the range over the 10 realisations. (b) The vertical velocity of cells in the tissue, excluding stem and cells experiencing the removal force. The point is the mean, and the error bars show minimum and maximum over all simulations and time points. (c) The cell turnover times. The box shows the median and 1st and 3rd quartiles, and the error bars show the minimum and maximum values. (d) The steady state corneum thickness plotted against cell turnover time, with the dashed line showing a linear fit to the points.

similar to the diseased system results discussed above. The mean cell velocity is approximately the same (maximum difference is 2.9%), regardless of the proportion of healthy/diseased cells. The turnover times follow the expected increase in time given the increase in tissue thickness and average cell velocity.

Figure 8.10d, similarly to Figure 8.8c, shows there is a linear relationship between corneum height and turnover time. Here the relationship is determined to be:

$$\tau_{\text{ss}} = 1.04T_T - 1.68, \tag{8.10}$$

which is the same as the relationship in Equation (8.9) determined for the diseased system.

If we consider the possible hypotheses for treating a condition such as NS, you would expect the treatment to involve increasing the inhibitor in some or all cells. Here we have determined that, given a choice between a large increase in inhibitor levels in a proportion of cells, or a small inhibitor concentration increase in all cells, the former has a better effect on the system.

8.3 Summary

In this chapter we have presented a multiscale model which couples the multicellular model developed in Chapters 4 to 6 and the subcellular model developed in Chapter 7. Using this model, we are able to simulate an epidermal tissue that self-regulates its thickness.

We used the model to investigate the effect of reducing the inhibitor in the cells, similar to what is seen in patients with NS. The reduction of the inhibitor frees up more enzyme to degrade the adhesion proteins, increasing the rate of degradation of the adhesion and consequently reducing the tissue thickness. We find that there is a linear relationship between the corneum thickness and the concentration of inhibitor.

Increasing the inhibitor concentration in all cells is one possible treatment for a condition such as NS, however it is possible that such a treatment would not be

effective in treating all cells. This latter scenario is ideal for testing in a multicellular model. The results using this scenario show that treating just 25% of the cells has a significant beneficial effect on the tissue thickness, recovering 44% of the lost corneum thickness in the model. Such a treatment is more effective than a small increase in inhibitor for all cells, where a 25% recovery of the inhibitor in all cells ($i_T = 0.25e_T$) recovers 27% of the lost corneum thickness. These proportions are, however, highly dependent on the parameters values used.

There are several limitations to the desquamation model. Many assumptions have been made in order to build a full multiscale model of desquamation. These include the limitations of the subcellular model discussed in Section 7.5. Additionally, adhesion degradation is assumed to be uniform around the circumference of the cell but *in vivo*, as described in Section 7.1, degradation occurs in the vertical direction first. We assume this is not important as our desquamation force is vertical, but it could have an effect.

The use of spherical cell shapes also has an effect on these results. For example, it would affect the number of cells that experience the removal force, as the flatter cells would cover more of the surface area, and it would affect the number of cell neighbours the cell is attached to. Finally, the point in the adhesion curve at which cells are lost is dependent on the magnitudes chosen for the maximum adhesion between cells and the removal force magnitude.

Our multiscale model of the epidermis has the potential to be used to implement different treatment strategies for a variety of conditions. We have also developed the model such that the implementation of further subcellular systems to drive other processes in the epidermis is straightforward. Through such systems we can gain a better understanding of how the subcellular kinetics impact the tissue structure and dynamics.

9 | Conclusion

In this study, we have developed a three dimensional multiscale model of the interfollicular epidermis to better understand how the tissue maintains its thickness. We couple a multicellular model of the tissue (with a robust model of cell proliferation) and a subcellular model for the desquamation process. By balancing these two processes, we are able to generate a tissue that maintains a steady state thickness. These results demonstrate that proliferation and degradation of cell-cell adhesion to enable desquamation are the two key processes for maintaining the thickness of the epidermis, and therefore the barrier function of the tissue. Furthermore, we show that an understanding of the process of degradation of adhesion proteins by enzymes is critical to understanding abnormalities in desquamation.

In this chapter we will discuss how the study has advanced the research into computational models of epidermal tissue, both in terms of the modelling and biological implications. We will also discuss the limitations of the research, and potential future work.

9.1 Advances made in this study

In this section, we discuss how this study has advanced the field of computational modelling of epidermal tissue. Advances have been made both in terms of the modelling techniques used, and the biological implications of the results. We discuss each of these below.

9.1.1 Modelling advances

The use of multicellular models of biological tissues has been an area of interest for several decades. With respect to the epidermis, the first two dimensional, discrete, multicellular model was published in 1995 by Stekel, Rashbass, and Williams [113], followed by Sun et al. [115] over a decade later. These models are usually based on overlapping spheres techniques.

Multicellular modelling

We use similar techniques for our multicellular model to previous models in the literature. A key difference in our model is the inclusion of a rotational division force, described in Chapter 5. With this new force, the model is more robust in maintenance of the basal layer of proliferative cells, removing the erroneous proliferative cell loss that can occur in other models. We also show that using a desquamation method based on the degradation of cell-cell adhesion with a removal force, rather than using a height or age threshold, is able to reproduce experimental observations where protecting the skin results in the accumulation of cells. When the protection is removed the cells are easily removed.

Multiscale modelling

The use of three dimensional multiscale models is fairly recent, particularly of the inter-follicular epidermis. Similarly to the models of Sun et al. [115] and Sütterlin et al. [117], we have integrated a subcellular DE model into an overlapping spheres model. Our model, however, varies in the implementation and the subcellular reactions considered. Firstly, we develop and implement a novel subcellular DE model for the degradation of the adhesion. This model is based on the competitive inhibition process hypothesised to occur in the corneum order to enable desquamation. Secondly, rather than coupling two previously developed modelling frameworks, the

subcellular and multicellular models are solved within the same code framework, similar to Van Leeuwen et al. [120] in colonic crypt models. Consequently, the coupling between the two models is very efficient. This allows us to run simulations with cell counts at magnitudes of 10^3 cells for time periods on the scale of months, or 10^5 iterations. This is significantly longer time periods, and faster computation, than the simulations run in Adra et al. [2] (on the scale of 10^2 iterations), however a direct speed comparison is difficult due to differences in compute power.

9.1.2 Biological implications

The main aim of this thesis was to understand how the epidermis regulated its homeostatic thickness. We found that the maintenance of a proliferative population, in combination with the degradation of cell-cell adhesion, was sufficient for the system to self-regulate its thickness: the system produces a loss rate equal, on average, to the birth rate. The value of this thickness was then a function of the proliferation rate, as this determines the upwards cell velocity, and the rate of desquamation, determined by the rate at which the adhesion degrades.

Cell proliferation and tissue thickness

We focus first on the cell proliferation. Cell proliferation is a major determinant of cell velocity, as the creation of new cells is the driver of the upwards movement of the cells. Our model determined that the regulation of the division direction may play a critical role in maintaining the proliferative population in the basal layer. The size of this proliferative population determines the overall rate of proliferation in the tissue, and consequently helps determine tissue thickness. Therefore the maintenance of this size is critical to maintaining the thickness of the tissue.

There are still many questions relating to cell division, particularly cell lineage, in the epidermis. The exact configuration of the proliferative population—whether it is one or two proliferative cell types—appears not to be important for the tissue

thickness. Results show the thickness is determined by the harmonic mean of the cell cycle lengths of the whole population.

The results only consider proliferative cells which undergo asymmetric division to produce one differentiated cell. Extending this concept to include a symmetric division lineage hypothesis, the rate value of importance for the tissue thickness is expected to be the rate at which differentiated cells are produced by the proliferative population.

Desquamation rates

Our new subcellular model for desquamation supports the hypothesis of desquamation driven by KLK enzymes. In this hypothesis KLK enzymes degrade the corneodesmosomes (adhesion proteins) between the cells, a process which is inhibited by LEKTI and regulated by local pH. Though the results show that enzyme dynamics follow the expected function over pH, they also show that there is a missing component to the model as the degradation occurs at too high a rate to match observed desquamation times *in vivo*. This missing component is likely to be the presence of the corneodesmosomes and other extracellular complexes limiting the diffusion of the enzymes, and therefore reducing the rate of degradation of the corneodesmosomes.

An additional factor in desquamation is stochasticity. It would be expected that not all cells would degrade at exactly the same rate, due to stochasticity in either the enzyme concentrations, the structure of the corneodesmosomes, or both. Results using the multicellular model showed that the more stochasticity there is in the system, modelled as stochasticity in the rate of cell-cell adhesion degradation, the thicker the tissue.

Modelling the genetic disease Netherton Syndrome

The genetic disease Netherton Syndrome is known to reduce production of the LEKTI inhibitor for the desquamation process. Our subcellular model results show that such a reduction in inhibitor is sufficient to explain the increased concentration of free enzyme observed in patient skin samples. Additionally, the multiscale model shows a decrease in the inhibitor has a noticeable effect on tissue thickness, even though model approximations cause the system to underestimate the effect of the reduced inhibitor. The relationship between the inhibitor concentration and tissue thickness is also shown to be linear. If we consider a hypothetical treatment for the diseased cells, that only cures a proportion of them, tissue thickness increases approximately quadratically with the number of cells treated.

9.2 Limitations of the model

The epidermis is a complex tissue, combining processes occurring at subcellular to tissue scales. As with any model, it was necessary to make many simplifications and assumptions in developing our model. Though we aimed to incorporate the key processes related to tissue thickness, the model only incorporates a minimal number of the multitude of processes occurring in the tissue. Many other processes, occurring concurrently to those modelled, could interact with, or in some way affect, the processes that have been included. Of those processes that are included in our model, simplifications were made with regards to tissue structure, for computational reasons, and assumptions and approximations were required when appropriate data was not available.

Examples of model simplifications to the tissue structure, relevant to the results of this study, are:

- spherical cells (rather than ellipsoidal at the base and disc-shaped at the top),
- a flat membrane (rather than undulating), and

- ignoring the structure of extracellular space in the subcellular model.

The first two examples would affect how cells move through the tissue, and therefore quantitatively affect the results of the model. The third simplification was discussed in detail in Chapter 7. To account for ignoring the extracellular structure it was necessary to modify the parameters of the subcellular model, resulting in a reduction in the impact of the disease on the system.

In order to accurately parameterise a model, it is necessary to have appropriate experimental data. Such data is often not available, or inaccessible to current experimental methods. Some key areas which would be assisted with more or better data are:

- the concentration and further rate parameters for the subcellular model,
- example environmental forces the epidermis might experience,
- proliferative cell density in the basal layer, and
- cell-cell and cell-membrane adhesion strength.

Similarly to the simplifications made above, this missing data would be expected to quantitatively change the model results, however would not be expected to cause significant qualitative differences.

9.3 Future work

Moving forward, the work of thesis could be extended by refinement of the model, and use of the model to understand further biological phenomena. Refinements to the model could remove many of the limitations discussed above. These could include:

1. incorporating extracellular structure into the enzyme kinetics model,
2. cell morphology change as cells migrate through the tissue, or

3. collaboration with experimental biologists to provide more appropriate data for parameterising and validating the model.

There are still many open research questions relating to the epidermis that could be investigated using a multiscale model. If we limit this to further studies on epidermal thickness, there are many environmental factors which can affect the thickness of the skin, such as ultraviolet rays. Incorporating models for these factors could shed more light on the regulatory mechanisms. Additionally, we know cell proliferation rate is critical to this process. The addition of subcellular control of proliferation—either in relation to the regulation of the division direction, the cell cycle, or the cell lineage—would provide a further level of understanding of the system.

More generally, the model has been developed within Chaste to allow for easy implementation of new mechanisms, the modification of current mechanisms, and the addition of further subcellular models. By using such an approach, it is possible to extend this model to investigate any component of the epidermis that affects or regulates tissue scale behaviours. Ideally, the multiscale model would one day be used to replace experimental studies, such as in predicting response to treatments. In comparison to experimental studies a computational model is cheaper, provides a more comprehensive understanding of response of the system, and can lessen the ethical difficulties associated with animal studies.

Bibliography

[1] Adams, J. C. and Watt, F. M. "Expression of Beta 1, Beta 3, Beta 4, and Beta 5 Integrins by Human Epidermal Keratinocytes and Non-Differentiating Keratinocytes." *The Journal of Cell Biology* 115.3 (Nov. 1991), pp. 829–841. DOI: 10.1083/jcb.115.3.829.

[2] Adra, S., Sun, T., MacNeil, S., et al. "Development of a Three Dimensional Multiscale Computational Model of the Human Epidermis". *PLoS ONE* 5.1 (Jan. 2010), e8511. DOI: 10.1371/journal.pone.0008511.

[3] Alarcon, T., Byrne, H. M., and Maini, P. K. "A Multiple Scale Model for Tumor Growth". *Multiscale Modeling & Simulation* 3.2 (2005), p. 36. DOI: 10.1137/040603760.

[4] Alberts, B., Johnson, A., Lewis, J., et al. *Molecular Biology of the Cell*. Sixth edition. New York, NY: Garland Science, Taylor and Francis Group, 2015. ISBN: 978-0-8153-4432-2.

[5] Alcolea, M. P. and Jones, P. H. "Lineage Analysis of Epidermal Stem Cells". *Cold Spring Harbor Perspectives in Medicine* 4.1 (Jan. 2014). DOI: 10.1101/cshperspect.a015206.

[6] Alcolea, M. P. and Jones, P. H. "Tracking Cells in Their Native Habitat: Lineage Tracing in Epithelial Neoplasia". *Nature Reviews Cancer* 13.3 (Mar. 2013), pp. 161–171. DOI: 10.1038/nrc3460.

[7] Al-Amoudi, A., Dubochet, J., and Norlén, L. "Nanostructure of the Epidermal Extracellular Space as Observed by Cryo-Electron Microscopy of Vitreous Sections of Human Skin". *Journal of Investigative Dermatology* 124.4 (Apr. 2005), pp. 764–777. DOI: 10.1111/j.0022-202X.2005.23630.x.

[8] Asare, A., Levorse, J., and Fuchs, E. "Coupling Organelle Inheritance with Mitosis to Balance Growth and Differentiation". *Science* 355.6324 (Feb. 2017). DOI: 10.1126/science.aah4701.

[9] Atwell, K., Qin, Z., Gavaghan, D., et al. "Mechano-Logical Model of C. Elegans Germ Line Suggests Feedback on the Cell Cycle". *Development* 142.22 (Nov. 2015), pp. 3902–3911. DOI: 10.1242/dev.126359.

[10] Borgoño, C. A., Michael, I. P., Komatsu, N., et al. "A Potential Role for Multiple Tissue Kallikrein Serine Proteases in Epidermal Desquamation". *Journal of Biological Chemistry* 282.6 (Sept. 2007), pp. 3640–3652. DOI: 10.1074/jbc.M607567200.

[11] Bouwstra, J. A., de Graaff, A., Gooris, G. S., et al. "Water Distribution and Related Morphology in Human Stratum Corneum at Different Hydration Levels". *Journal of Investigative Dermatology* 120.5 (May 2003), pp. 750–758. DOI: 10.1046/j.1523-1747.2003.12128.x.

[12] Brandner, J. M. "Tight Junctions and Tight Junction Proteins in Mammalian Epidermis". *European Journal of Pharmaceutics and Biopharmaceutics* 72.2 (Jan. 2009), pp. 289–294. DOI: 10.1016/j.ejpb.2008.08.007.

[13] Briggs, G. E. and Haldane, J. B. S. "A Note on the Kinetics of Enzyme Action". *Biochemical Journal* 19.2 (1925), pp. 338–339. DOI: 10.1042/bj0190338.

[14] Buske, P., Galle, J., Barker, N., et al. "A Comprehensive Model of the Spatio-Temporal Stem Cell and Tissue Organisation in the Intestinal Crypt". *PLoS*

Computational Biology 7.1 (Jan. 2011), e1001045. DOI: 10.1371/journal.pcbi.1001045.

[15] Campbell, N. A., ed. *Biology*. 8th ed. (Australian version). Sydney: Pearson Education, Inc., 2009. ISBN: 978-1-4425-0221-5.

[16] Candi, E., Schmidt, R., and Melino, G. "The Cornified Envelope: A Model of Cell Death in the Skin". *Nature Reviews Molecular Cell Biology* 6.4 (Apr. 2005), pp. 328–340.

[17] Caubet, C., Jonca, N., Brattsand, M., et al. "Degradation of Corneodesmosome Proteins by Two Serine Proteases of the Kallikrein Family, SCTE/KLK5/hK5 and SCCE/KLK7/hK7". *Journal of Investigative Dermatology* 122.5 (May 2004), pp. 1235–1244. DOI: 10.1111/j.0022-202X.2004.22512.x.

[18] Chao, C. Y., Zheng, Y.-P., and Cheing, G. L. "Epidermal Thickness and Biomechanical Properties of Plantar Tissues in Diabetic Foot". *Ultrasound in Medicine & Biology* 37.7 (Jan. 2011), pp. 1029–1038. DOI: 10.1016/j.ultrasmedbio.2011.04.004.

[19] Clayton, E., Doupé, D. P., Klein, A. M., et al. "A Single Type of Progenitor Cell Maintains Normal Epidermis". *Nature* 446.7132 (Mar. 2007), pp. 185–189. DOI: 10.1038/nature05574.

[20] Cursons, J., Angel, C. E., Hurley, D. G., et al. "Spatially Transformed Fluorescence Image Data for ERK-MAPK and Selected Proteins within Human Epidermis". *GigaScience* 4 (2015), p. 63. DOI: 10.1186/s13742-015-0102-5.

[21] Cursons, J., Gao, J., Hurley, D. G., et al. "Regulation of ERK-MAPK Signaling in Human Epidermis". *BMC Systems Biology* 9 (2015), p. 41. DOI: 10.1186/s12918-015-0187-6.

[22] Deraison, C., Bonnart, C., Lopez, F., et al. "LEKTI Fragments Specifically Inhibit KLK5, KLK7, and KLK14 and Control Desquamation through a pH-Dependent Interaction". *Molecular Biology of the Cell* 18.9 (June 2007), pp. 3607–3619. DOI: 10.1091/mbc.e07-02-0124.

[23] Dover, R. and Potten, C. S. "Heterogeneity and Cell Cycle Analyses from Time-Lapse Studies of Human Keratinocytes in Vitro". *Journal of Cell Science* 89.3 (Mar. 1988), pp. 359–364.

[24] Drasdo, D. and Höhme, S. "Individual-Based Approaches to Birth and Death in Avascular Tumors". *Mathematical and Computer Modelling* 37.11 (June 2003), pp. 1163–1175. DOI: 10.1016/S0895-7177(03)00128-6.

[25] Du, H., Wang, Y., Haensel, D., et al. "Multiscale Modeling of Layer Formation in Epidermis". *PLoS Computational Biology* 14.2 (Feb. 2018), e1006006. DOI: 10.1371/journal.pcbi.1006006.

[26] Egawa, G. and Kabashima, K. "Barrier Dysfunction in the Skin Allergy". *Allergology International* 67.1 (Jan. 2018), pp. 3–11. DOI: 10.1016/j.alit.2017.10.002.

[27] Egawa, M., Hirao, T., and Takahashi, M. "In Vivo Estimation of Stratum Corneum Thickness from Water Concentration Profiles Obtained with Raman Spectroscopy". *Acta Dermato-Venereologica* 87.1 (2007), pp. 4–8. DOI: 10.2340/00015555-0183.

[28] Elias, P. M. "The Epidermal Permeability Barrier: From the Early Days at Harvard to Emerging Concepts". *Journal of Investigative Dermatology* 122.2 (Feb. 2004), pp. xxxvi–xxxix. DOI: 10.1046/j.0022-202X.2004.22233.x.

[29] Elias, P. M., Brown, B. E., Crumrine, D., et al. "Origin of the Epidermal Calcium Gradient: Regulation by Barrier Status and Role of Active vs Passive Mechanisms". *Journal of Investigative Dermatology* 119.6 (Dec. 2002), pp. 1269–1274. DOI: 10.1046/j.1523-1747.2002.19622.x.

[30] Encyclopaedia Britannica, I., ed. *The New Encyclopaedia Britannica*. 15th ed. Chicago: Encyclopaedia Britannica, 1994. ISBN: 978-0-85229-591-5.

[31] Evans, N. D., Oreffo, R. O. C., Healy, E., et al. "Epithelial Mechanobiology, Skin Wound Healing, and the Stem Cell Niche". *Journal of the Mechanical Behavior of Biomedical Materials* 28 (Dec. 2013), pp. 397–409. DOI: 10.1016/j.jmbbm.2013.04.023.

[32] Fortugno, P., Bresciani, A., Paolini, C., et al. "Proteolytic Activation Cascade of the Netherton Syndrome–Defective Protein, LEKTI, in the Epidermis: Implications for Skin Homeostasis". *Journal of Investigative Dermatology* 131.11 (Nov. 2011), pp. 2223–2232. DOI: 10.1038/jid.2011.174.

[33] Fuchs, E. "Genetic Disorders of Keratins and Their Associated Proteins". *Journal of Dermatological Science* 13.3 (Dec. 1996), pp. 181–192. DOI: 10.1016/S0923-1811(96)00568-3.

[34] Galle, J., Loeffler, M., and Drasdo, D. "Modeling the Effect of Deregulated Proliferation and Apoptosis on the Growth Dynamics of Epithelial Cell Populations In Vitro". *Biophysical Journal* 88.1 (Jan. 2005), pp. 62–75. DOI: 10.1529/biophysj.104.041459.

[35] Gatenby, R. A. and Gawlinski, E. T. "A Reaction-Diffusion Model of Cancer Invasion". *Cancer Research* 56.24 (Dec. 1996), pp. 5745–5753.

[36] Gladkova, N. D., Petrova, G. A., Nikulin, N. K., et al. "In Vivo Optical Coherence Tomography Imaging of Human Skin: Norm and Pathology". *Skin Research and Technology* 6.1 (Feb. 2000), pp. 6–16. DOI: 10.1034/j.1600-0846.2000.006001006.x.

[37] Goldschmidt, H. and Kligman, A. M. "Desquamation of the Human Horny Layer". *Archives of Dermatology* 95.6 (June 1967), pp. 583–586. DOI: 10.1001/archderm.1967.01600360029004.

[38] Gord, A., Holmes, W. R., Dai, X., et al. "Computational Modelling of Epidermal Stratification Highlights the Importance of Asymmetric Cell Division for Predictable and Robust Layer Formation". *Journal of The Royal Society Interface* 11.99 (Oct. 2014), p. 20140631. DOI: 10.1098/rsif.2014.0631.

[39] Grabe, N. and Neuber, K. "A Multicellular Systems Biology Model Predicts Epidermal Morphology, Kinetics and Ca2+ Flow". *Bioinformatics* 21.17 (Jan. 2005), pp. 3541–3547. DOI: 10.1093/bioinformatics/bti585.

[40] Grabe, N. and Neuber, K. "Simulating Psoriasis by Altering Transit Amplifying Cells". *Bioinformatics* 23.11 (Jan. 2007), pp. 1309–1312. DOI: 10.1093/bioinformatics/btm042.

[41] Green, K. J. and Simpson, C. L. "Desmosomes: New Perspectives on a Classic". *Journal of Investigative Dermatology* 127.11 (Nov. 2007), pp. 2499–2515. DOI: 10.1038/sj.jid.5701015.

[42] Haridas, P., McGovern, J. A., McElwain, S. D. L., et al. "Quantitative Comparison of the Spreading and Invasion of Radial Growth Phase and Metastatic Melanoma Cells in a Three-Dimensional Human Skin Equivalent Model". *PeerJ* (Sept. 2017), e3754. DOI: 10.7717/peerj.3754.

[43] Has, C. "Peeling Skin Disorders: A Paradigm for Skin Desquamation". *Journal of Investigative Dermatology* 138.8 (Aug. 2018), pp. 1689–1691. DOI: 10.1016/j.jid.2018.05.020.

[44] Hashmi, S. and Marinkovich, M. P. "Molecular Organization of the Basement Membrane Zone". *Clinics in Dermatology*. Bullous Skin Diseases: Part I 29.4 (July 2011), pp. 398–411. DOI: 10.1016/j.clindermatol.2011.01.009.

[45] Hirsch, T., Rothoeft, T., Teig, N., et al. "Regeneration of the Entire Human Epidermis Using Transgenic Stem Cells". *Nature* 551.7680 (Nov. 2017), pp. 327–332. DOI: 10.1038/nature24487.

[46] Hoops, S., Sahle, S., Gauges, R., et al. "COPASI—a COmplex PAthway SImulator". *Bioinformatics* 22.24 (Dec. 2006), pp. 3067–3074. DOI: 10.1093/bioinformatics/btl485.

[47] Hsu, Y.-C., Li, L., and Fuchs, E. "Emerging Interactions between Skin Stem Cells and Their Niches". *Nature Medicine* 20.8 (Aug. 2014), pp. 847–856. DOI: 10.1038/nm.3643.

[48] Hu, S. and Cucinotta, F. A. "Epidermal Homeostasis and Radiation Responses in a Multiscale Tissue Modeling Framework". *Integrative Biology* 6.1 (Jan. 2014), pp. 76–89. DOI: 10.1039/c3ib40141c.

[49] Igawa, S., Kishibe, M., Murakami, M., et al. "Tight Junctions in the Stratum Corneum Explain Spatial Differences in Corneodesmosome Degradation". *Experimental Dermatology* 20.1 (Jan. 2011), pp. 53–57. DOI: 10.1111/j.1600-0625.2010.01170.x.

[51] Ilic, D., Bollinger, J. M., Gelb, M., et al. "sPLA2 and the Epidermal Barrier". *Biochimica et Biophysica Acta (BBA) - Molecular and Cell Biology of Lipids* 1841.3 (Mar. 2014), pp. 416–421. DOI: 10.1016/j.bbalip.2013.11.002.

[52] Ipponjima, S., Hibi, T., and Nemoto, T. "Three-Dimensional Analysis of Cell Division Orientation in Epidermal Basal Layer Using Intravital Two-Photon Microscopy". *PLoS ONE* 11.9 (Sept. 2016), e0163199. DOI: 10.1371/journal.pone.0163199.

[53] Ishida-Yamamoto, A., Deraison, C., Bonnart, C., et al. "LEKTI Is Localized in Lamellar Granules, Separated from KLK5 and KLK7, and Is Secreted in the Extracellular Spaces of the Superficial Stratum Granulosum". *Journal of Investigative Dermatology* 124.2 (Feb. 2005), pp. 360–366. DOI: 10.1111/j.0022-202X.2004.23583.x.

[54] Ishida-Yamamoto, A. and Igawa, S. "The Biology and Regulation of Corneodesmosomes". *Cell and Tissue Research* 360.3 (June 2015), pp. 477–482. DOI: 10.1007/s00441-014-2037-z.

[55] Johnson, J. L., Najor, N. A., and Green, K. J. "Desmosomes: Regulators of Cellular Signaling and Adhesion in Epidermal Health and Disease". *Cold Spring Harbor Perspectives in Medicine* 4.11 (Nov. 2014). DOI: 10.1101/cshperspect.a015297.

[56] Johnston, S. T., Shah, E. T., Chopin, L. K., et al. "Estimating Cell Diffusivity and Cell Proliferation Rate by Interpreting IncuCyte ZOOM™ Assay Data Using the Fisher-Kolmogorov Model". *BMC Systems Biology* 9 (July 2015). DOI: 10.1186/s12918-015-0182-y.

[57] Kashibuchi, N., Hirai, Y., O'Goshi, K., et al. "Three-Dimensional Analyses of Individual Corneocytes with Atomic Force Microscope: Morphological Changes Related to Age, Location and to the Pathologic Skin Conditions". *Skin Research and Technology* 8.4 (2002), pp. 203–211. DOI: 10.1034/j.1600-0846.2002.00348.x.

[58] Kaur, P. and Li, A. "Adhesive Properties of Human Basal Epidermal Cells: An Analysis of Keratinocyte Stem Cells, Transit Amplifying Cells, and Postmitotic Differentiating Cells". *Journal of Investigative Dermatology* 114.3 (Mar. 2000), pp. 413–420. DOI: 10.1046/j.1523-1747.2000.00884.x.

[59] Kaur, P. and Potten, C. S. "The Interfollicular Epidermal Stem Cell Saga: Sensationalism versus Reality Check". *Experimental Dermatology* 20.9 (Sept. 2011), pp. 697–702. DOI: 10.1111/j.1600-0625.2011.01338.x.

[60] Keener, J. and Sneyd, J. *Mathematical Physiology. I: Cellular Physiology.* 2nd ed. Vol. 8/1. Interdisciplinary Applied Mathematics. New York, NY: Springer-Verlag New York, 2009. ISBN: 978-0-387-75846-6. DOI: 10.1007/978-0-387-75847-3.

[61] Kelly-Mancuso, G., Kopelan, B., Azizkhan, R. G., et al. "Junctional Epidermolysis Bullosa Incidence and Survival: 5-Year Experience of the Dystrophic Epidermolysis Bullosa Research Association of America (DebRA) Nurse Educator, 2007 to 2011". *Pediatric Dermatology* 31.2 (2014), pp. 159–162. DOI: 10.1111/pde.12157.

[62] Kirschner, N. and Brandner, J. M. "Barriers and More: Functions of Tight Junction Proteins in the Skin". *Annals of the New York Academy of Sciences* 1257.1 (June 2012), pp. 158–166. DOI: 10.1111/j.1749-6632.2012.06554.x.

[63] Kobayashi, Y., Kitahata, H., and Nagayama, M. "Model for Calcium-Mediated Reduction of Structural Fluctuations in Epidermis". *Physical Review E* 92.2 (Aug. 2015), p. 022709. DOI: 10.1103/PhysRevE.92.022709.

[64] Kobayashi, Y., Sanno, Y., Sakai, A., et al. "Mathematical Modeling of Calcium Waves Induced by Mechanical Stimulation in Keratinocytes". *PLOS ONE* 9.3 (Mar. 2014), e92650. DOI: 10.1371/journal.pone.0092650.

[65] Kobayashi, Y., Sawabu, Y., Kitahata, H., et al. "Mathematical Model for Calcium-Assisted Epidermal Homeostasis". *Journal of Theoretical Biology* 397 (May 2016), pp. 52–60. DOI: 10.1016/j.jtbi.2016.02.032.

[66] Komatsu, N., Saijoh, K., Jayakumar, A., et al. "Correlation between SPINK5 Gene Mutations and Clinical Manifestations in Netherton Syndrome Patients". *Journal of Investigative Dermatology* 128.5 (May 2008), pp. 1148–1159. DOI: 10.1038/sj.jid.5701153.

[67] Krstić, R. V. *Ultrastructure of the mammalian cell: an atlas*. Berlin; New York: Springer-Verlag, 1979. ISBN: 978-0-387-09583-7.

[69] Kulukian, A. and Fuchs, E. "Spindle Orientation and Epidermal Morphogenesis". *Philosophical Transactions of the Royal Society B* 368.1629 (Nov. 2013), p. 20130016. DOI: 10.1098/rstb.2013.0016.

[70] Lechler, T. and Fuchs, E. "Asymmetric Cell Divisions Promote Stratification and Differentiation of Mammalian Skin". *Nature* 437.7056 (Sept. 2005), pp. 275–280.

[71] Lewis, J. E., Wahl, J. K., Sass, K. M., et al. "Cross-Talk between Adherens Junctions and Desmosomes Depends on Plakoglobin". *The Journal of Cell Biology* 136.4 (Feb. 1997), pp. 919–934. DOI: 10.1083/jcb.136.4.919.

[72] Li, X., Upadhyay, A. K., Bullock, A. J., et al. "Skin Stem Cell Hypotheses and Long Term Clone Survival – Explored Using Agent-Based Modelling". *Scientific Reports* 3 (May 2013), p. 1904. DOI: 10.1038/srep01904.

[73] Lulevich, V., Yang, H.-y., Rivkah Isseroff, R., et al. "Single Cell Mechanics of Keratinocyte Cells". *Ultramicroscopy* 110.12 (Nov. 2010), pp. 1435–1442. DOI: 10.1016/j.ultramic.2010.07.009.

[74] Mascré, G., Dekoninck, S., Drogat, B., et al. "Distinct Contribution of Stem and Progenitor Cells to Epidermal Maintenance". *Nature* 489.7415 (Sept. 2012), pp. 257–262. DOI: 10.1038/nature11393.

[75] Matsui, T. and Amagai, M. "Dissecting the Formation, Structure and Barrier Function of the Stratum Corneum". *International Immunology* 27.6 (June 2015), pp. 269–280. DOI: 10.1093/intimm/dxv013.

[76] Meineke, F. A., Potten, C. S., and Loeffler, M. "Cell Migration and Organization in the Intestinal Crypt Using a Lattice-Free Model". *Cell Proliferation* 34.4 (Aug. 2001), pp. 253–266.

[77] Menon, G. K. "New Insights into Skin Structure: Scratching the Surface". *Advanced Drug Delivery Reviews* 54, Supplement (Nov. 2002), S3–S17. DOI: 10.1016/S0169-409X(02)00121-7.

[78] Menon, G. K., Cleary, G. W., and Lane, M. E. "The Structure and Function of the Stratum Corneum". *International Journal of Pharmaceutics* 435.1 (Oct. 2012), pp. 3–9. DOI: 10.1016/j.ijpharm.2012.06.005.

[79] Meşe, G., Richard, G., and White, T. W. "Gap Junctions: Basic Structure and Function". *Journal of Investigative Dermatology* 127.11 (Nov. 2007), pp. 2516–2524. DOI: 10.1038/sj.jid.5700770.

[80] Michaelis, L. and Menten, M. L. "Die Kinetik Der Invertinwirkung". *Biochemische Zeitschrift* 49 (1913), pp. 333–369.

[81] Miller, C., Crampin, E., and Osborne, J. *Maintaining the stem cell niche in multicellular models of epithelia*. 2020. arXiv: 1811.10781 [q-bio.TO].

[82] Milstone, L. M. "Epidermal Desquamation". *Journal of Dermatological Science* 36.3 (Dec. 2004), pp. 131–140. DOI: 10.1016/j.jdermsci.2004.05.004.

[83] Mirams, G. "Subcellular Phenomena in Colorectal Cancer". PhD. University of Nottingham, 2008.

[84] Mirams, G. R., Arthurs, C. J., Bernabeu, M. O., et al. "Chaste: An Open Source C++ Library for Computational Physiology and Biology". *PLoS Computational Biology* 9.3 (Mar. 2013), e1002970. DOI: 10.1371/journal.pcbi.1002970.

[85] Mirams, G. R., Fletcher, A. G., Maini, P. K., et al. "A Theoretical Investigation of the Effect of Proliferation and Adhesion on Monoclonal Conversion in the Colonic Crypt". *Journal of Theoretical Biology* 312 (Nov. 2012), pp. 143–156. DOI: 10.1016/j.jtbi.2012.08.002.

[86] Morrison, S. J. and Kimble, J. "Asymmetric and Symmetric Stem-Cell Divisions in Development and Cancer". *Nature* 441.7097 (June 2006), pp. 1068–1074.

[87] Murray, J. D. *Mathematical Biology. I. An Introduction*. 3rd ed. Vol. 17. Interdisciplinary Applied Mathematics. Springer-Verlag New York, 2002. ISBN: 978-0-387-22437-4. DOI: 10.1007/b98868.

[88] Ohman, H. and Vahlquist, A. "In Vivo Studies Concerning a pH Gradient in Human Stratum Corneum and Upper Epidermis". *Acta Dermato-Venereologica* 74 (1994), pp. 375–379. DOI: 10.2340/0001555574375379.

[89] Osborne, J. M. "Multiscale Model of Colorectal Cancer Using the Cellular Potts Framework". *Cancer Informatics* 14.Suppl 4 (Oct. 2015), pp. 83–93. DOI: 10.4137/CIN.S19332.

[90] Osborne, J. M., Fletcher, A. G., Pitt-Francis, J. M., et al. "Comparing Individual-Based Approaches to Modelling the Self-Organization of Multicellular Tissues". *PLoS Computational Biology* 13.2 (2017), e1005387. DOI: 10.1371/journal.pcbi.1005387.

[92] Pasparakis, M., Haase, I., and Nestle, F. O. "Mechanisms Regulating Skin Immunity and Inflammation". *Nature Reviews Immunology* 14.5 (May 2014), pp. 289–301. DOI: 10.1038/nri3646.

[94] Pathmanathan, P., Cooper, J., Fletcher, A., et al. "A Computational Study of Discrete Mechanical Tissue Models". *Physical Biology* 6.3 (2009), p. 036001. DOI: 10.1088/1478-3975/6/3/036001.

[95] Pease, J. C. and Tirnauer, J. S. "Mitotic Spindle Misorientation in Cancer – out of Alignment and into the Fire". *Journal of Cell Science* 124.7 (Apr. 2011), pp. 1007–1016. DOI: 10.1242/jcs.081406.

[96] Pitt-Francis, J., Pathmanathan, P., Bernabeu, M. O., et al. "Chaste: A Test-Driven Approach to Software Development for Biological Modelling". *Computer Physics Communications* 180.12 (Dec. 2009), pp. 2452–2471. DOI: 10.1016/j.cpc.2009.07.019.

[97] Potten, C. S., Saffhill, R., and Maibach, H. I. "Measurement of the Transit Time for Cells through the Epidermis and Stratum Corneum of the Mouse and Guinea-Pig". *Cell Proliferation* 20.5 (Sept. 1987), pp. 461–472. DOI: 10.1111/j.1365-2184.1987.tb01355.x.

[98] Potten, C. S. “Epidermal Transit Times”. *British Journal of Dermatology* 93.6 (1975), pp. 649–658. DOI: 10.1111/j.1365-2133.1975.tb05115.x.

[99] Potten, C. S. and Major, D. “Repeated Injection (Continuous Labelling) Experiments in Mouse Epidermis”. *Journal of Theoretical Biology* 82.3 (Feb. 1980), pp. 465–472. DOI: 10.1016/0022-5193(80)90249-0.

[100] Poulson, N. D. and Lechler, T. “Robust Control of Mitotic Spindle Orientation in the Developing Epidermis”. *The Journal of Cell Biology* 191.5 (Nov. 2010), pp. 915–922. DOI: 10.1083/jcb.201008001.

[101] Rashbass, J., Stekel, D., and Williams, E. D. “The Use of a Computer Model to Simulate Epithelial Pathologies”. *The Journal of Pathology* 179.3 (1996), pp. 333–339. DOI: 10.1002/(SICI)1096-9896(199607)179:3<333::AID-PATH584>3.0.CO;2-3.

[102] Rawlings, A., Sabin, R., Harding, C., et al. “The Effect of Glycerol and Humidity on Desmosome Degradation in Stratum Corneum”. *Archives of Dermatological Research* 287.5 (1995), pp. 457–464. DOI: 10.1007/BF00373429.

[103] Rippa, A., Vorotelyak, E., Vasiliev, A., et al. “The Role of Integrins in the Development and Homeostasis of the Epidermis and Skin Appendages”. *Acta Naturae* 5.4 (2013), pp. 22–33.

[104] Roberts, D. and Marks, R. “The Determination of Regional and Age Variations in the Rate of Desquamation: A Comparison of Four Techniques”. *Journal of Investigative Dermatology* 74.1 (Jan. 1980), pp. 13–16. DOI: 10.1111/1523-1747.ep12514568.

[105] Sada, A., Jacob, F., Leung, E., et al. “Defining the Cellular Lineage Hierarchy in the Interfollicular Epidermis of Adult Skin”. *Nature Cell Biology* 18.6 (June 2016), pp. 619–631. DOI: 10.1038/ncb3359.

[106] Sakamoto, K., Lochhead, R. Y., Maibach, H. I., et al., eds. *Cosmetic Science and Technology: Theoretical Principles and Applications*. 1st ed. Amsterdam Oxford Cambridge: Elsevier, 2017. ISBN: 978-0-12-802054-8.

[107] Sandby-Møller, J., Poulsen, T., and Wulf, H. C. "Epidermal Thickness at Different Body Sites: Relationship to Age, Gender, Pigmentation, Blood Content, Skin Type and Smoking Habits". *Acta Dermato-Venereologica* 83.6 (Nov. 2003), pp. 410–413. DOI: 10.1080/00015550310015419.

[108] Schaller, G. and Meyer-Hermann, M. "A Modelling Approach towards Epidermal Homoeostasis Control". *Journal of Theoretical Biology* 247.3 (Aug. 2007), pp. 554–573. DOI: 10.1016/j.jtbi.2007.03.023.

[109] Seltmann, K., Fritsch, A. W., Käs, J. A., et al. "Keratins Significantly Contribute to Cell Stiffness and Impact Invasive Behavior". *Proceedings of the National Academy of Sciences of the United States of America* 110.46 (Nov. 2013), pp. 18507–18512. DOI: 10.1073/pnas.1310493110.

[110] Sick, S., Reinker, S., Timmer, J., et al. "WNT and DKK Determine Hair Follicle Spacing through a Reaction-Diffusion Mechanism". *Science* 314.5804 (2006), pp. 1447–1450.

[111] Simpson, M. J., Landman, K. A., and Bhaganagarapu, K. "Coalescence of Interacting Cell Populations". *Journal of Theoretical Biology* 247.3 (Aug. 2007), pp. 525–543. DOI: 10.1016/j.jtbi.2007.02.020.

[112] Solanas, G. and Benitah, S. A. "Regenerating the Skin: A Task for the Heterogeneous Stem Cell Pool and Surrounding Niche". *Nature Reviews Molecular Cell Biology* 14.11 (Nov. 2013), pp. 737–748. DOI: 10.1038/nrm3675.

[113] Stekel, D., Rashbass, J., and Williams, E. D. "A Computer Graphic Simulation of Squamous Epithelium". *Journal of Theoretical Biology* 175.3 (Aug. 1995), pp. 283–293. DOI: 10.1016/S0022-5193(95)80011-5.

[114] Sun, J. D. and Linden, K. G. "Netherton Syndrome: A Case Report and Review of the Literature". *International Journal of Dermatology* 45.6 (June 2006), pp. 693–697. DOI: 10.1111/j.1365-4632.2005.02637.x.

[115] Sun, T., Adra, S., Smallwood, R., et al. "Exploring Hypotheses of the Actions of TGF-$B1$ in Epidermal Wound Healing Using a 3D Computational Multiscale Model of the Human Epidermis". *PLOS ONE* 4.12 (Dec. 2009), e8515. DOI: 10.1371/journal.pone.0008515.

[116] Sun, T., McMinn, P., Coakley, S., et al. "An Integrated Systems Biology Approach to Understanding the Rules of Keratinocyte Colony Formation". *Journal of The Royal Society Interface* 4.17 (Dec. 2007), pp. 1077–1092. DOI: 10.1098/rsif.2007.0227.

[117] Sütterlin, T., Kolb, C., Dickhaus, H., et al. "Bridging the Scales: Semantic Integration of Quantitative SBML in Graphical Multi-Cellular Models and Simulations with EPISIM and COPASI". *Bioinformatics* 29.2 (Jan. 2013), pp. 223–229. DOI: 10.1093/bioinformatics/bts659.

[118] Sütterlin, T., Tsingos, E., Bensaci, J., et al. "A 3D Self-Organizing Multicellular Epidermis Model of Barrier Formation and Hydration with Realistic Cell Morphology Based on EPISIM". *Scientific Reports* 7 (Mar. 2017), p. 43472. DOI: 10.1038/srep43472.

[119] Tariq, H., Bella, J., Jowitt, T. A., et al. "Cadherin Flexibility Provides a Key Difference between Desmosomes and Adherens Junctions". *Proceedings of the National Academy of Sciences of the United States of America* 112.17 (Apr. 2015), pp. 5395–5400. DOI: 10.1073/pnas.1420508112.

[120] Van Leeuwen, I. M. M., Mirams, G. R., Walter, A., et al. "An Integrative Computational Model for Intestinal Tissue Renewal". *Cell Proliferation* 42.5 (Oct. 2009), pp. 617–636. DOI: 10.1111/j.1365-2184.2009.00627.x.

[121] Vilar, J. M. G., Jansen, R., and Sander, C. "Signal Processing in the TGF-β Superfamily Ligand-Receptor Network". *PLOS Computational Biology* 2.1 (Jan. 2006), e3. DOI: 10.1371/journal.pcbi.0020003.

[122] Voronoi, G. "Nouvelles Applications Des Paramètres Continus à La Théorie Des Formes Quadratiques. Premier Mémoire. Sur Quelques Propriétés Des Formes Quadratiques Positives Parfaites". *Journal für die reine und angewandte Mathematik* 133 (Jan. 1908), p. 97.

[123] Weinstein, G. D., McCullough, J. L., and Ross, P. "Cell Proliferation in Normal Epidermis". *Journal of Investigative Dermatology* 82.6 (June 1984), pp. 623–628. DOI: 10.1111/1523-1747.ep12261462.

[124] Whitton, J. T. and Everall, J. "The Thickness of the Epidermis". *British Journal of Dermatology* 89.5 (Nov. 1973), p. 467.

[125] Xie, W. and Zhou, J. "Regulation of Mitotic Spindle Orientation during Epidermal Stratification". *Journal of Cellular Physiology* 232.7 (July 2017), pp. 1634–1639. DOI: 10.1002/jcp.25750.

[126] Yingzi Li, Hammad Naveed, Sema Kachalo, et al. "Mechanisms of Regulating Cell Topology in Proliferating Epithelia: Impact of Division Plane, Mechanical Forces, and Cell Memory". *PLoS ONE* 7.8 (Aug. 2012), pp. 1–10. DOI: 10.1371/journal.pone.0043108.

[127] Zhang, H., Hou, W., Henrot, L., et al. "Modelling Epidermis Homoeostasis and Psoriasis Pathogenesis". *Journal of The Royal Society Interface* 12.103 (Feb. 2015), p. 20141071. DOI: 10.1098/rsif.2014.1071.